Chapter 7
Combustion Characteristic Analysis

Abbreviations and Symbols

ATDC	After top dead center
BMF	Burned mass fraction
BTDC	Before top dead center
CAD	Crank angle degree
CARS	Coherent anti-Stokes Raman scattering
CD	Combustion duration
CI	Compression ignition
CR	Compression ratio
DP	Difference pressure
ECU	Electronic control unit
EGR	Exhaust gas recirculation
EOC	End of combustion
EOI	End of injection
EVC	Exhaust valve closing
EVO	Exhaust valve opening
HCCI	Homogeneous charge compression ignition
HR	Heat release
HRR	Heat release rate
HT	Heat transfer
ID	Ignition delay
IGN	Ignition timing
IHR	Initial heat release
IHRR	Initial heat release rate
IMEP	Indicated mean effective pressure
IP	Intake pressure
IT	Ignition timings
IVC	Inlet valve closing

R. K. Maurya, *Reciprocating Engine Combustion Diagnostics*, Mechanical Engineering Series, https://doi.org/10.1007/978-3-030-11954-6_7

LIF	Laser-induced fluorescence
LSR	Laser Rayleigh scattering
LTR	Low-temperature reaction
MP	Mixing period
NDP	Normalized difference pressure
°CA	Crank angle degree
PDF	Probability distribution function
PDR	Pressure departure ratio
PMEP	Pumping mean effective pressure
PMR	Pressure ratio management
PPC	Partially premixed combustion
PSD	Power spectral density
ROHR	Rate of heat release
RW	Rassweiler and Withrow
SI	Spark ignition
SOC	Start of combustion
SOV	Start of vaporization
SRS	Spontaneous Raman scattering
TDC	Top dead center
TP	Throttle position
TSA	Thermal stratification analysis
A	Area of the reaction front
B	Bore
D	Cylinder diameter
L	Characteristic length
P	Pressure
T	Temperature
u	Internal energy
V	Volume of cylinder
W	Work on the piston
Q_{ht}	Heat transfer
CA_{DD}	Detection delay crank angle
c_p	Specific heat capacity at constant pressure
c_v	Specific heat capacity at constant volume
$c_{v,b}$	Specific heat capacity of burn charge at constant volume
$c_{v,u}$	Specific heat capacity of unburnt charge at constant volume
HRR_{max}	Maximum heat release rate
L_c	Instantaneous combustion chamber height
n_a	Moles of air
n_c, n_e	Compression and expansion polytropic exponents
n_f	Moles of fuel
n_R	Moles of residual gases
Nu	Nusselt number
P_{atm}	Atmospheric pressure

P_{cyl}	Measured cylinder pressure
P_{diff}	Pressure difference
p_{EOC}	Pressure at end of combustion
P_{mot}	Motored cylinder pressure
Pr	Prandtl number
p_{SOC}	Pressure at start of combustion
r_c	Compression ratio
Re	Reynolds number
S_p	Mean piston speed
T_{atm}	Atmospheric temperature
T_b	Burned temperature
T_{EVC}	Temperature at EVC
T_{IVC}	Temperature at IVC
T_U	Burned zone temperature
T_w	Wall temperature
U_s	Sensible energy of the charge
V_{ch}	Characteristic velocity
V_{EOC}	Volume at end of combustion
V_{SOC}	Volume at start of combustion
V_{TDC}	Volume at TDC
x_b	Mass burn fraction
δQ_{hrr}	Elemental combustion heat released
$\Delta\theta_b$	Combustion duration
γ	Specific heat
θ	Crank angle position
λ	Excess air ratio (relative air-fuel ratio)

7.1 Introduction

In-cylinder pressure measurement and analysis is an essential tool for automotive engine research and diagnosis due to its direct relationship with the combustion process. The pressure developed in the combustion chamber at any crank angle position is the net result of the interplay of many overlapping phenomena such as combustion, change in volume, wall heat transfer, blowby, etc. The more that is known about the combustion process in the engine cylinder, the easier is to control it [1]. One approach for investigating the combustion process in an internal combustion engine is the heat release analysis. The heat release analysis provides valuable information on combustion behavior which is an important factor in fuel economy, engine performance, and emissions of harmful pollutants. Heat release analysis is a backward calculation process which requires pressure as input and analyzes the whole system within the framework consisting mainly of conservation equations for mass and energy and the equation of state. An insight into the engine combustion

process, i.e., whether the burning rate is fast or slow, complete or incomplete, advanced or retard, and so on, can be obtained through the heat release analysis. Therefore, heat release analysis can be considered as a combustion diagnostic tool to gain an understanding about an existing engine which otherwise would be very difficult and would require highly advanced instrumentations and techniques, which may not even be possible to apply on production engines.

More stringent demands on emissions (by legislation) and efficiency (fuel economy) introduce new challenges for the design and control of modern automotive engines. Additionally, the complexity of the control system is increasing because of the added number of degrees of freedom available for engine control. This makes the task of calibrating a traditional open-loop engine control system more difficult and time-consuming. Thus, the interest in closed-loop engine control is growing as a solution to these problems. Combustion phasing (i.e., combustion event timing with respect to the position of the piston) is a central measure to control in an internal combustion engine as it affects both engine emissions and fuel conversion efficiency. The most common approach of measuring the combustion phasing is by means of heat release analysis [2]. Thus, online estimation of combustion phasing (or heat release) is required for condition monitoring and combustion management of reciprocating engines. Additionally, engine hardware development and control parameters tuning are usually supported by processing in-cylinder pressure data (heat release analysis) which allow examining a number of different solutions so that the combined effects of such solutions can be quickly tested experimentally.

Thermodynamic analysis of measured cylinder pressure data is a very powerful tool used for quantifying combustion parameters. There are two main approaches that are often referred to as “burn rate analysis” and “heat release analysis” [3]. Burn rate analysis is mainly used for determining burn crank angle positions (typically in gasoline engines), and it is used to obtain the mass fraction burned, which is a normalized quantity with a scale of zero to one. Heat release analysis is most commonly used for diesel engine combustion studies and produces absolute energy with units of Joules or Joules/degree. Different methods for the burn rate and heat release rate analysis (single/multi-zone model, Rassweiler and Withrow model, etc.) for offline and real-time estimation are discussed in this chapter (Sects. 7.2 and 7.5). Gas temperature and wall heat transfer (Sects. 7.3 and 7.4) are also required for performing accurate heat release analysis. Based on the calculation of heat release, different combustion parameters such as the start of combustion (SOC), end of combustion (EOC), combustion duration, etc. can be estimated. Typically, mass fraction burned is used for estimation of combustion phasing. Different methods that can be used for determination of mass fraction burned from measured cylinder pressure data are discussed in the next section.

7.2 Burned Mass Fraction Estimation and Analysis

Burned mass fraction (BMF) is a measure of the fraction of energy released from combustion of fuel to the total energy released at the end of the combustion process. Burned gas mass fraction is typically determined from the analysis of measured cylinder pressure [4]. The combustion rate is a very important parameter affecting fuel conversion efficiency, maximum temperature and pressure in a cycle, and exhaust emissions. The combustion rate is frequently quantified in gasoline engines by the estimation of burn angles which are the crank angles at which the BMF reaches a specified value. Conventional cylinder pressure-based techniques are able to predict the BMF as a function of crank angle position more accurately in SI engines than in diesel engines [5]. To calculate the burned mass fraction, cylinder pressure analysis can be performed using either relatively simple equations capable of real-time processing or by using more complicated post-processing thermodynamic heat release models. Several techniques have been proposed in the published literature for determination of burned mass fraction using measured cylinder pressure data.

7.2.1 Marvin's Graphical Method

Marvin proposed one of the first applications of experimental cylinder pressure data for direct diagnosis of engine combustion process [6]. Figure 7.1 illustrates the graphical method for calculation of burned mass fraction using measured cylinder pressure. In this method, the compression and expansion processes are considered as polytropic evolution (PV^n = constant) during closed valve conditions except for the period of combustion. The slopes of straight lines on the log P − log V curves

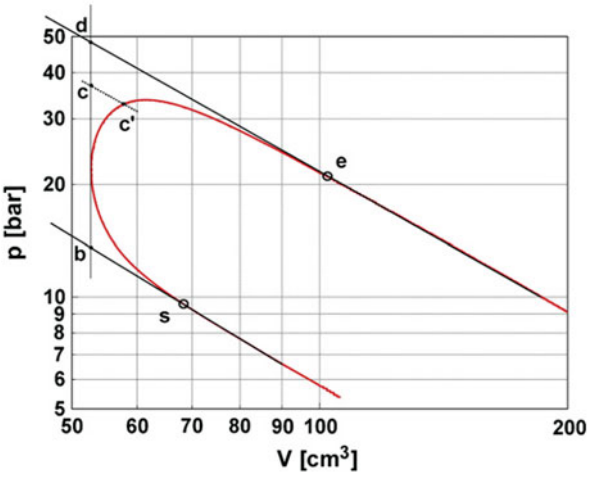

Fig. 7.1 Illustration of the graphical method of burned mass fraction calculation [7]

provide the compression and expansion polytropic index values. The positions of deviation of actual pressure from straight lines during compression and expansion phase are defined as the start of combustion (SOC) and end of combustion (EOC), respectively (Fig. 7.1), which are denoted by points "s" and "e," respectively. The points "b" and "d" on the curve are obtained by extrapolating the straight ideal compression and expansion lines.

The SOC and EOC points (s and e in Fig. 7.1) can be determined by considering the inflection points in the diagrams, which can be calculated using Eq. (7.1) [5, 7].

$$\frac{d^2(\log P)}{d(\log V)^2} = 0 \tag{7.1}$$

For a constant volume heat addition between points "b" and "d" (Fig. 7.1), ideally the chemical energy released during the combustion process generates a directly proportional pressure rise in the cylinder. Thus, burned mass fraction (x_b) at a particular point "c" is calculated by the ratio of the length *b-c* to length *b-d*, which is represented by Eq. (7.2).

$$x_b = \frac{P_c - P_b}{P_b - P_d} \tag{7.2}$$

For computation of burned mass fraction with experimental pressure data, a point corresponding to constant volume point (c) on the measured pressure data (point c′) needs to be estimated. The point c′ is determined as the intersection between constant volume combustion line and segment c′-c, which represents an equivalent and appropriate polytropic compression from point (c′) to (c) [7]. It can be noticed that this method of burned mass fraction estimation is more valid for the engines which have a close to a constant volume heat release during combustion. Since conventional SI engine is close to Otto cycle (constant volume heat addition), thus, this method is more valid for SI engines. The BMF evaluated using Marvin's method is compared with theoretical two-zone model, and it is found that it has a difference of 2.5% between two curves and 1.5°CA difference in crank angle position corresponding to 50% BMF in both methods [5].

7.2.2 Rassweiler and Withrow Method

Rassweiler and Withrow [8] model is normally used for simple mass fraction burned calculations in spark ignition engines. The Rassweiler and Withrow (RW) method is a sort of analytical version of Marvin's graphical method of burned mass fraction evaluation. This method is established on the assumption that the variations in the cylinder pressure (due to piston movement and the gas-to-wall heat transfer) can be expressed by polytropic processes (PV^n = constant). The polytropic indices are

based on calculated values obtained from the measured cylinder pressure data before and after combustion, the compression index (or exponent) being used up to TDC, and the expansion value thereafter [4]. The change in cylinder pressure consists of two components: (1) pressure rise due to combustion ($\Delta P_{\text{comb,RW}}$) and (2) pressure rise due to piston movement (volume change) and wall heat transfer. Pressure rise due to combustion is used for calculation of burned mass fraction, and it is calculated by Eq. (7.3).

$$\begin{cases} \Delta P_{\text{comb,RW}} = P(\theta_i) - P(\theta_{i-1})[V_{i-1}/V_i]^{n_c} & \text{if } \theta_i \le \theta_{\text{TDC}} \\ \Delta P_{\text{comb,RW}} = P(\theta_i) - P(\theta_{i-1})[V_{i-1}/V_i]^{n_e} & \text{if } \theta_i > \theta_{\text{TDC}} \end{cases} \tag{7.3}$$

where n_c and n_e are polytropic exponents during compression and expansion process.

The burned mass fraction (x_b) can be calculated using Eq. (7.4) in this method.

$$x_b = \frac{m_{b(i)}}{m_{b(\text{total})}} = \frac{\sum_{j=0}^{i} \Delta P_{\text{comb,RW}}(\theta_j)}{\sum_{j=0}^{N} \Delta P_{\text{comb,RW}}(\theta_j)} \tag{7.4}$$

Here it is expected that the first point (sample 0) is between inlet valve closing (IVC) and the SOC and that last point (sample N) is after combustion has completed. The SOC and the EOC can be defined as the maximum (before TDC) and the minimum (after TDC) crank angle positions, respectively, where $\Delta P_{\text{comb,RW}}$ becomes virtually zero [5]. Figure 7.2 shows the variation of $\Delta P_{\text{comb,RW}}$ and

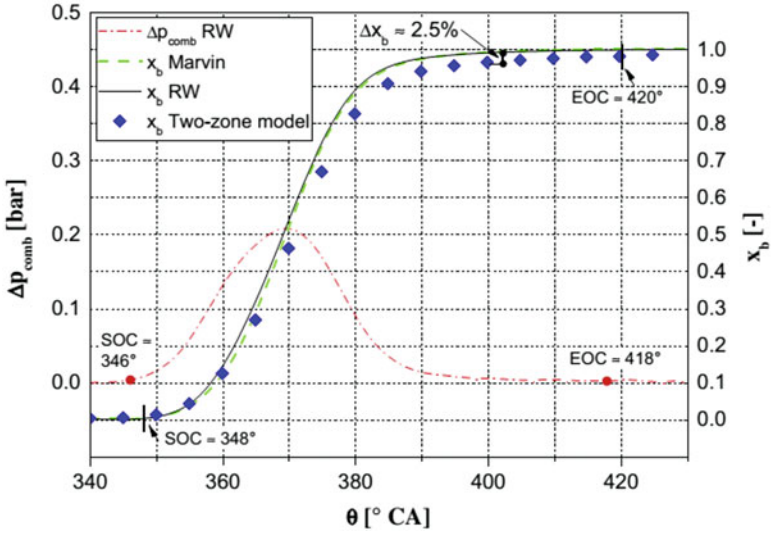

Fig. 7.2 Comparison of burned mass fraction calculated using the Marvin and RW methods in gasoline engine operating at 7.9 bar BMEP and 3300 rpm [5]

compares the burned mass fraction (BMF) calculation using Marvin's and RW methods in a gasoline SI engine. The figure shows that both methods have similar BMF using experimental data and a slight deviation from computed BMF using two-zone model.

The elemental combustion heat released (δQ_{hrr}) during the $\Delta\theta$ CA in SI engine can roughly be expressed as a heat released as constant volume process, as represented in Eq. (7.5).

$$\delta Q_{\text{hrr}} = M c_{\text{v}} \Delta T_{\text{comb,RW}} \tag{7.5}$$

where M is the mass of the charge during combustion. The temperature increase ΔT_{comb} can be estimated as Eq. (7.6).

$$\Delta T_{\text{comb,RW}} = \frac{\Delta p_{\text{comb,RW}} V_{\text{TDC}}}{MR} \tag{7.6}$$

where R is universal gas constant.

The elemental heat release can be expressed in terms of pressure rise due to combustion using Eqs. (7.5) and (7.6). The Eq. (7.7) shows that the heat release is proportional to the pressure rise due to combustion.

$$\delta Q_{\text{hrr}} = \frac{C_{\text{v}}}{R} V_{\text{TDC}} \Delta p_{\text{comb,RW}} \approx \frac{V_{\text{TDC}}}{\gamma - 1} \{p(\theta_i) - p_{i-1}[V_{i-1}/V(\theta_i)]^m\} \tag{7.7}$$

where V_{TDC} is the volume of the cylinder at TDC, m is the polytropic exponent, and γ is the ratio of specific heat of the charge. Since the combustion process does not occur at constant volume, the pressure rise due to combustion is not directly proportional to the mass of fuel burned. The pressure rise due to combustion has to be referenced to a datum volume (V_{TDC}).

McCuiston, Lavoie, and Kauffmann (MLK) suggested a similar relation for calculation of approximate burned mass fraction with the condition that the volume of the burning charge does not significantly changes during the combustion process [9]. The BMF equation proposed is shown by Eq. (7.8).

$$x_{\text{b,MLK}} = \frac{pV^m - p_{\text{soc}} V_{\text{soc}}^m}{p_{\text{EOC}} V_{\text{EOC}}^m - p_{\text{soc}} V_{\text{SOC}}^m} \tag{7.8}$$

where p and V are the pressure and volume at a particular crank angle degree (CAD) and p_{SOC}, p_{EOC}, V_{SOC}, and V_{EOC} are the pressure values and volumes at SOC and EOC positions.

Figure 7.3 illustrates the BMF calculation using the MLK method in gasoline SI engine. The figure shows that calculated BMF using MLK method is virtually coincident with the BMF predicted using two-zone model and the difference between the MFB50 positions of the two methods is less than 0.2°CA [5].

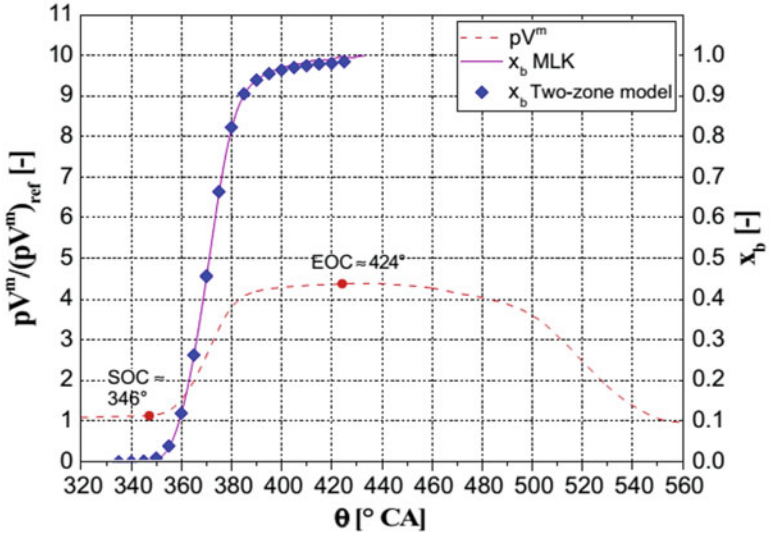

Fig. 7.3 Illustration of burned mass fraction calculation using the MLK method [5]

Development of combustion is often analyzed using BMF by estimating the flame development angle ($\Delta\theta_d$) and the rapid burning angle ($\Delta\theta_b$), which are defined as the crank angle from the spark timing position to 10% of BMF and from 10% to 90% of BMF, respectively. Figure 7.4 illustrates BMF as a function of crank angle in an SI engine operated at different fuels and ignition timings (IT). The BMF is calculated using Rassweiler and Withrow method using Eq. (7.4). Figure 7.4a shows that synthetic gases air-fuel mixture is burned faster than biogas, even though the ignition is more retarded [10]. The ignition timing of different fuel is selected corresponding to maximum thermal efficiency for a particular fuel. The evolution of the BMF at different ignition timing for syngas is presented in Fig. 7.4b. The figure depicts that the combustion tends to occur early as the spark timing is advanced.

7.2.3 Pressure Ratio and Pressure Departure Ratio Method

The pressure ratio management (PRM) is proposed by Matekunas [11] and is defined as the ratio of the cylinder pressure from a firing cycle $P(\theta)$ and the corresponding motored cylinder pressure $P_{mot}(\theta)$ at each crank angle position in the cycle. The motoring pressure can be obtained experimentally by measuring the pressure in the absence of combustion in the cylinder (running the engine by electrical means or combustion in other cylinder in case of multicylinder engine), or it can be obtained numerically by approximating the compression as a polytropic evolution. The pressure ratio can be represented by Eq. (7.9).

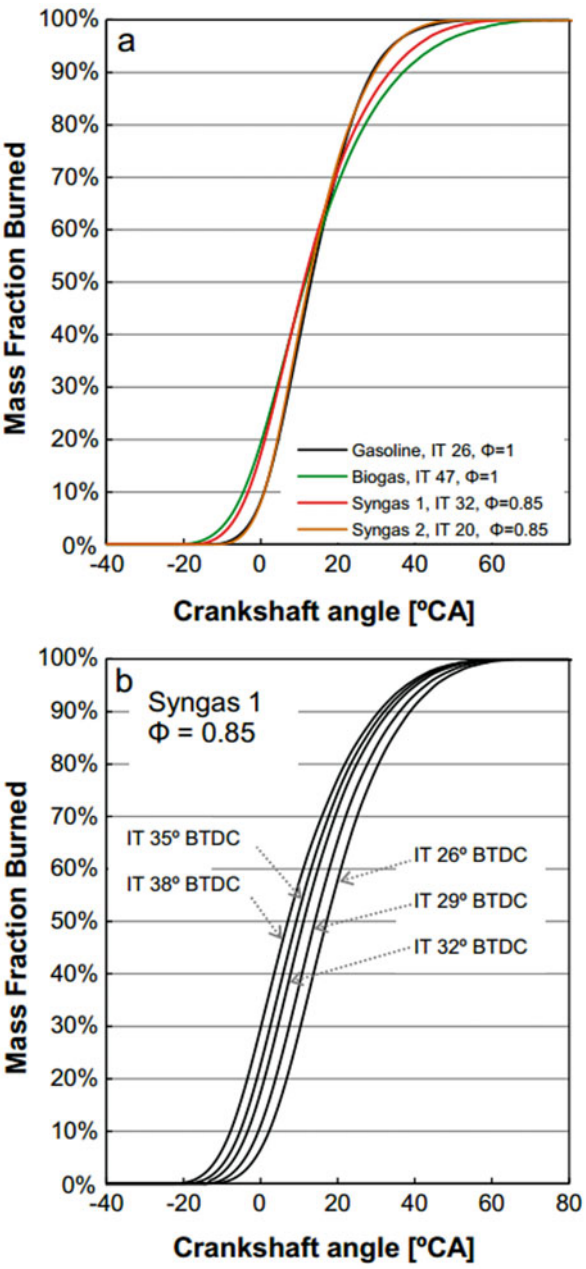

Fig. 7.4 Variations of BMF burned with CA position for (**a**) different fuels at ignition timing corresponding to the maximum thermal efficiency and (**b**) different ignition timing (IT) at syngas operation in an SI engine [10]

$$\mathrm{PR}(\theta) = \frac{P(\theta)}{P_{\mathrm{mot}}(\theta)} - 1 \tag{7.9}$$

The pressure ratio (Eq. 7.9) is normalized by its maximum value, which produces traces that are similar to the burned mass fraction profiles. The BMF can be calculated by Eq. (7.10) using a pressure ratio management method.

$$x_{\mathrm{b,PRM}} = \frac{\mathrm{PR}(\theta)}{\mathrm{PR}(\theta)_{\max}} \tag{7.10}$$

A similar approach for calculation of burned mass fraction in a diesel engine is also proposed [12]. The diesel pressure departure ratio (PDR) algorithm is proposed for fast and reliable determination of the mass fraction burnt. This algorithm is also based on the principle of the RW model which suggests that the fractional pressure rise due to combustion can be used for estimation of BMF. The PDR algorithm utilizes the fired and the motoring pressure signals for cyclic estimation of the CA50, and the mass fraction burned closely matches the normalized cumulative heat release curve [12] (Fig. 7.5). The pressure departure ratio is defined by Eq. (7.11).

$$\mathrm{PDR}(\theta) = \frac{P(\theta) + C_1}{P_{\mathrm{mot}}(\theta) + C_2} - 1 \tag{7.11}$$

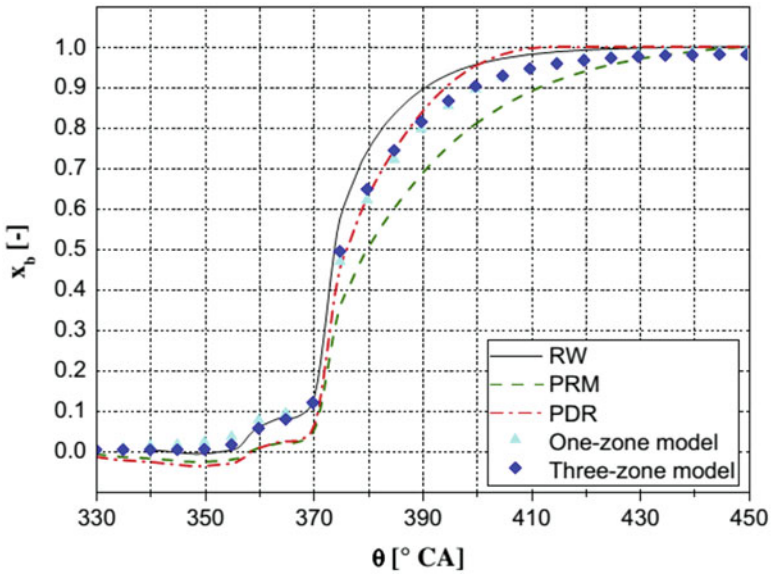

Fig. 7.5 Comparison of the mass fraction burnt calculation methods in a diesel engine using triple injection in the cycle [5]

where C_1 is the fired pressure characterization coefficient and C_2 is the motored pressure characterization coefficient. Constant C_2 is a correction for the polytropic relationship between the volume and the motoring pressure, while the C_1 is a correction for the difference between the pressure change due to the volume of the fired and the motored cycle. The coefficients C_1 and C_2 are constants for a particular engine configuration and are largely not affected by the boost pressure, EGR, etc. [12]. The PDR value is close to zero before SOC and reaches a peak value at the EOC.

The mass fraction burnt can be calculated by normalizing the PDR with its maximum value $\mathrm{PDR}_{\max}$ as represented in Eq. (7.12).

$$x_{\mathrm{b,PDR}} = \frac{\mathrm{PDR}(\theta)}{\mathrm{PDR}_{\max}} \tag{7.12}$$

Figure 7.6 shows the comparison of the burned mass fraction in a diesel engine with multiple fuel injection in a cycle. The PDR method is found to be the best approximation of the mass burned fraction obtained by using single-zone and three-zone models for diesel engine [5]. Figure 7.6 illustrates that the RW method provides better performance than the PRM method. However, both RW and PRM methods seem inadequate for BMF estimation in diesel engines, and PDR is a relatively better method of BMF determination.

7.2.4 Vibe's Function-Based Method

The Vibe function [13] is often used as a parameterization of the burned mass fraction (x_{b}), and it is represented by Eq. (7.13).

$$x_{\mathrm{b}} = 1 - \exp\left\{-a\left(\frac{\theta - \theta_0}{\Delta\theta_{\mathrm{b}}}\right)^{m+1}\right\} \tag{7.13}$$

where θ is the crank angle, θ_0 is the crank angle at the start of combustion, $\Delta\theta_{\mathrm{b}}$ is the combustion duration, a is duration parameter, and m is the shape factor. The shape parameter (m) governs the pressure rise rate and the location of the point of inflection of the BMF curve.

For a particular engine, the parameters "m" and "a" are estimated by trial and error [14]. The parameters are adjusted until the pressure-time curve produced by cycle simulation matches the experimental pressure-time signal. Typical values of the parameters "m" and "a" are 2 and 5, respectively.

7.2.5 Apparent Heat Release-Based Method

The burned mass fraction can also be estimated by computing heat release from measured cylinder pressure data using first law of thermodynamics with single-zone assumption. The detailed algorithm for calculation of heat release from experimental cylinder pressure data is presented in Sect. 7.5. The apparent heat release can be calculated using Eq. (7.14), and wall heat transfer as well as blowby losses are neglected in this equation.

$$\frac{\partial Q}{\partial \theta} = \frac{\gamma}{\gamma - 1} p \frac{dV}{d\theta} + \frac{1}{\gamma - 1} V \frac{\partial p}{\partial \theta} \tag{7.14}$$

The cumulative heat release curve can be determined by integrating the heat release rate obtained using Eq. (7.14), starting from θ_{ivc} (crank angle of intake valve closing) to the current angle [15]. Starting point of integration can be any point between intake valve closing and start of combustion.

$$Q(\theta) = \int_{\theta_{ivc}}^{\theta} \frac{dQ(\alpha)}{d\alpha} d\alpha \tag{7.15}$$

The mass fraction burned can be obtained by normalizing the heat release calculated using Eq. (7.15). The cumulative heat release profile is usually identified as a function of crank angle with the help of a normalized curve which starts with zero at SOC and ends with a value of one at EOC. Assuming that the BMF is directly proportional to the heat release, the burned mass fraction is calculated by Eq. (7.16).

$$x_{b,HR} = \frac{Q(\theta)}{Q(\theta)_{max}} \tag{7.16}$$

The mass fraction burnt (MFB) calculated using this method is dependent on the values of the ratio of specific heat (γ) used in Eq. (7.14). The γ values are typically dependent on the gas temperature. Depending on the complexity, constant γ value as well as function of temperature can be used for calculation of BMF [4].

The sensitivity of MFB calculations to common sources of error in the measured pressure data shows that MFB errors produced as a result of pressure data errors should be relatively small for well-designed algorithms [4]. The highest sensitivity is to absolute pressure referencing errors (especially at part load), and this sensitivity can be made worse by resulting errors generated in the calculated compression and expansion exponents. Signal noise should not produce significant errors for normally defined burn angles but can cause problems with burn angles below 10% and above 90% and major problems with burn rates. A minimum of 150 cycles should be adequate for burn angle statistics which is less than would normally be required for IMEP calculations [4]. A crank angle resolution of 1.0° is recommended for most applications, but coarser resolutions of several degrees could be used if necessary with only a small loss in accuracy.

7.3 Combustion Gas Temperature Estimation

Thermodynamic state of the in-cylinder gases is defined by properties such as pressure, temperature, and density. Pressure is normally uniform in the combustion chamber, and it can be readily measured using a piezoelectric pressure transducer. Charge density can also be easily determined from cylinder volume and the amount of gases trapped in the cylinder. The gas temperature during compression can be considered uniform except for thermal boundary layers near the cylinder wall [16]. Temperature is normally not uniform during combustion in the conventional SI or CI engines because combustion is not occurring uniformly throughout the combustion chamber. However, combustion occurs almost homogeneously throughout the combustion chamber except in the proximity of combustion chamber walls in the HCCI engine. Thus, the assumption of uniform temperature during combustion is more closer to actual value is possibly in HCCI combustion. The bulk temperature of the charge can be estimated using ideal gas equation by assuming uniform temperature within the combustion chamber. The average gas temperature as a function of crank angle position can be calculated using Eq. (7.17) [1].

$$T(\theta) = \frac{P(\theta)V(\theta)n(\theta)}{P_{\mathrm{IVC}}V_{\mathrm{IVC}}n_{\mathrm{IVC}}}T_{\mathrm{IVC}} \tag{7.17}$$

where P, V, and T are the cylinder pressure, volume, and temperature of the cylinder gases, respectively. Temperature of gases at intake valve closing (IVC) position is an important variable, which is required for computation of bulk charge temperature.

One of the methods to calculate the temperature at IVC (T_{IVC}) is given by Eq. (7.18) [17].

$$T_{\mathrm{IVC}} = \frac{1}{(n_{\mathrm{a}} + n_{\mathrm{f}} + n_{\mathrm{R}})} \times \frac{P_{\mathrm{IVC}}V_{\mathrm{IVC}}}{R} \tag{7.18}$$

where n_{a}, n_{f}, and n_{R} are the moles of air, fuel, and residual gases, respectively, and R is the universal gas constant. Pressure at IVC position can be estimated by measured pressure data, and the volume at IVC position can be calculated by engine geometry. Moles of air and fuel can be estimated from the measured air and fuel values and their respective molecular weights. Moles of residual gas can be estimated by Eq. (7.19).

$$n_{\mathrm{R}} = \frac{P_{\mathrm{EVC}}V_{\mathrm{EVC}}}{T_{\mathrm{EVC}}R} \tag{7.19}$$

Pressure and volume known at exhaust valve closing (EVC) can be estimated similar to inlet valve closing (IVC). Temperature at exhaust valve closing is unknown in Eq. (7.19). The temperature measured close to the exhaust valve in the exhaust manifold can be used to estimate the T_{EVC}. The temperature measured is

a multi-cycle-averaged exhaust temperature, and it is lower than the cylinder temperature at EVC due to heat transfer. However, it is demonstrated that if the exhaust manifold temperature and pressure are used to calculate the moles of residual gas instead of T_{EVC} and P_{EVC}, the trapped gas fraction is very close to the experimentally measured residual fraction using the in-cylinder CO_2 method [17]. Thus, exhaust manifold temperature and pressure can be used to estimate the moles of residual gases, and temperature at IVC can be computed.

The gas temperature at IVC is influenced by heat transfer and residual gases, which are normally difficult to measure and determine. The air in the intake manifold is heated from intake manifold temperature (T_{im}) to T_a by the hot valves and the locally high heat transfer coefficients in the cylinder. Additionally, inducted fuel undergoes evaporation that affects the charge temperature. Another method is proposed to determine the charge temperature at IVC in a gasoline engine by considering the energy equation with a lumped process for heating, evaporation, and mixing the initial air-fuel mixture temperature [15]. The resultant temperature of the air-fuel mixture is calculated by Eq. (7.20).

$$T_{af} = \frac{m_a c_{pa} T_a + m_f c_{pf} T_f - m_f h_{v,f} + Q}{m_a c_{pa} + m_f c_{pf}} \tag{7.20}$$

where $h_{v,f}$ is the vaporization enthalpy for the fuel and Q is the heat added to the fresh mixture, which is difficult to estimate without detailed measurements. The residual gases and fresh charge are mixed in the combustion chamber, and temperature of the charge can be determined using Eq. (7.21). The residual gases have also been cooled down by heat transfer to the cylinder walls before mixing during the gas exchange process.

$$T_{ivc} = \frac{m_{af} c_{paf} T_{af} - m_r c_{pr} T_r}{m_{af} c_{paf} - m_r c_{pr}} \tag{7.21}$$

In this method, several variables need to determine using complex models. Therefore, charge temperature can be calculated by the simplified model using Eq. (7.22). In this equation, heat transfer is neglected which provides $T_{af} = T_{im}$, and c_p is assumed the same for both residuals and fresh air and fuel mixtures.

$$T_{ivc} = T_{af}(1 - x_r) + x_r T_r \tag{7.22}$$

where x_r is the residual gas fraction, which can be estimated by several models using cylinder pressure data (Chap. 10).

The combustion gas temperature plays a significant role in NO_x formation and its subsequent emissions. NOx formation is very sensitive to peak temperature encountered during the combustion. At temperatures above 1800 K, the NO_x formation rate increases rapidly. The maximum temperature in the combustion chamber also affects the combustion efficiency. At lower temperatures, combustion efficiency decreases,

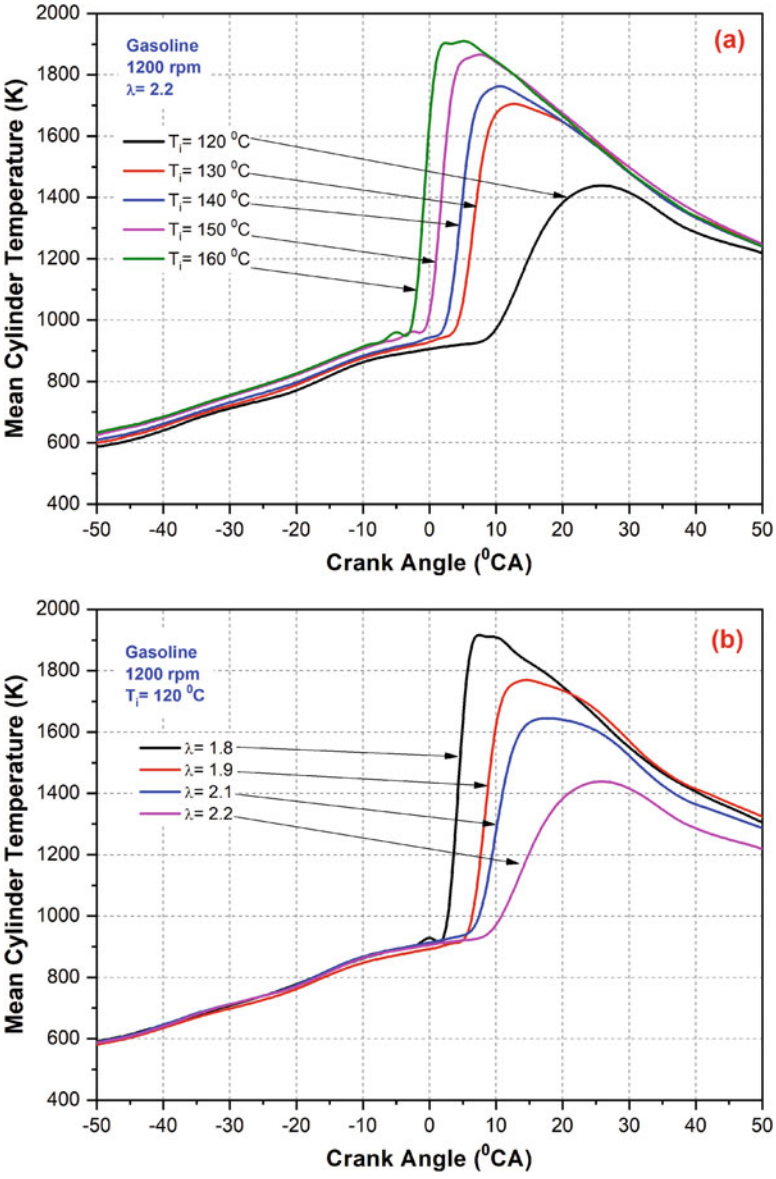

Fig. 7.6 Effect of λ and T_i on average cylinder temperature using gasoline at 1200 rpm in HCCI engine

which leads to higher unburned hydrocarbon emissions. The mean gas temperature history in the combustion chamber is shown in Fig. 7.6 at 1200 rpm in the HCCI engine using gasoline. Figure 7.6b shows that the mean gas temperature in the combustion chamber is highest for the richest mixture and decreases as the mixture

becomes leaner. Mean gas temperature in the combustion chamber is also affected by the initial temperature of the charge (Fig. 7.6a). Mean gas temperature of the combustion chamber is higher for a charge with higher initial temperature due to advanced combustion phasing. When intake air temperature increases, from 120 to 130 °C, change in mean gas temperature is large as compared to other inlet air temperatures due to a substantial increase in combustion efficiency and advanced combustion phasing (Fig. 7.6a).

Figure 7.7 shows the variation for T_{max} in HCCI operating range for gasoline and ethanol fuel at 1200 rpm. The figure depicts that the contour lines of T_{max} are inclined, which means T_{max} is dependent on λ as well as intake air temperature (T_i). It can also be noticed that the value of T_{max} is highest closer to the knock boundary for richer mixture for both the fuels (Fig. 7.7). Maximum value of T_{max} in HCCI operating range is relatively higher for ethanol in comparison to gasoline due to advanced combustion phasing.

Temperature determined from Eq. (7.17) by assuming a single zone in the cylinder can be used to calculate the burned gas temperature by considering two zones (burned and unburned) in the combustion chamber. Two-zone model is divided into two zones: one containing the unburned gases and the other containing the burned gases, separated by an infinitesimal thin divider representing the flame front. Each zone is homogenous considering that temperature, thermodynamic properties, and the pressure are the same throughout the zones. A simple two-zone model is proposed to determine the burned zone temperature (T_b) and the unburned zone temperature (T_u) [18].

The unburned zone temperature (T_u) is assumed to be equal to the single-zone temperature (T) before the start of combustion (SOC). The unburned zone temperature (T_u) after SOC can be estimated assuming adiabatic compression of the unburned charge as shown in Eq. (7.23).

$$T_u = T_{u,SOC}\left(\frac{p}{p_{SOC}}\right)^{1-1/\gamma} = T_{SOC}\left(\frac{p}{p_{SOC}}\right)^{1-1/\gamma} \tag{7.23}$$

Energy balance between the single-zone and the two-zone models can be written by Eq. (7.24).

$$(m_b + m_u)c_v T = m_b c_{v,b} T_b + m_u c_{v,u} T_u \tag{7.24}$$

where $c_{v,b}$ and $c_{v,u}$ are the constant volume-specific heat of burned and unburned charge. Assuming $c_v = c_{v,b} = c_{v,u}$, i.e., a calorically perfect gas, the Eq. (7.24) can be written as Eq. (7.25).

$$T = \frac{m_b T_b + m_u T_u}{m_b + m_u} = x_b T_b + (1 - x_b) T_u \tag{7.25}$$

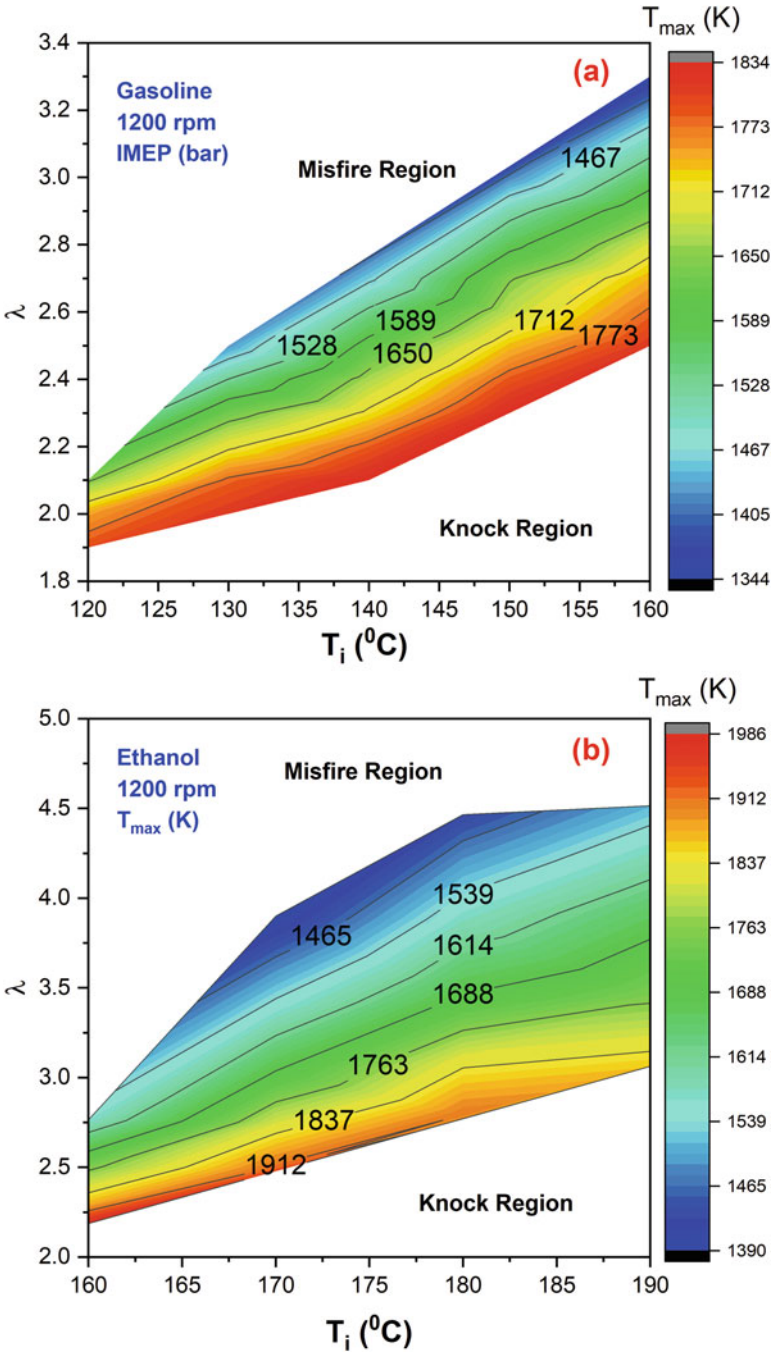

Fig. 7.7 Variation of T_{max} w.r.t. λ and T_i in HCCI operating range for gasoline and ethanol at 1200 rpm

where the single-zone temperature can be seen as the mass-weighted mean temperature of the two zones. The burned temperature (T_b) can be calculated by Eq. (7.26).

$$T_b = \frac{T - (1 - x_b)T_u}{x_b} \tag{7.26}$$

Heider [19] has defined an approach of burnt zone temperature calculation to determine the NO_x emissions more precisely. Thereby, the difference between the unburnt and burnt zone temperature is modeled by Eq. (7.27). As shown in Eq. (7.28), B describes the effect of the combustion using the cylinder pressure (p) minus the motored engine pressure (p_0), completed by the burned mass m_b.

$$T_b - T_{ub} = B \cdot A^* \tag{7.27}$$

$$B = 1 - \frac{\int_{\varphi_{SOC}}^{\varphi} (p - p_0) \cdot m_b \cdot d\varphi}{\int_{\varphi_{SOC}}^{\varphi_{EVO}} (p - p_0) \cdot m_b \cdot d\varphi} \tag{7.28}$$

A^* is an engine and combustion system-specific factor for the determination of the temperature level in the reaction (burnt) zone at the start of combustion. A method for estimation of A^* defined depending on engine stroke and global air-fuel ratio [20]. For engines with wide combustion bowl and without inlet swirl, the values of A^* are around 1600 K for a typical diesel engine. However, this model is not providing satisfactory results for constant volume combustion. The improved correlation for burnt zone temperature calculation based on combustion chamber thermodynamics and optical analysis is proposed in reference [21]. The found model in Eq. (7.29) calculates a temperature offset to the mass averaged temperature T which considers the combustion process by means of the normalized burn heat release (x) and the mixture air-fuel ratio λ.

$$\begin{aligned} T_b &= (A^* \cdot (1 - x) + x \cdot A) \cdot (1 - x) + T \\ A^* &= \left(0.9 - 2.26 \cdot \lambda + 1.9 \cdot \lambda^2 - 0.5 \cdot \lambda^3\right)^{-1} \end{aligned} \tag{7.29}$$

Further, an engine-specific factor A describes the temperature level in the burning zone at start of combustion. For engines up to 500 cc displacement per cylinder, good results can be reached with $A \approx 850$ K [21].

Combustion gas temperature plays a significant role in combustion and emission. For understanding autoignition kinetics of end-gas temperature is required with accuracy. Additionally, cylinder gas temperature is required for estimating the convective heat transfer and radiative loss to the wall and the thermal stress to wall material [16]. For measuring the gas temperature, the sensor used in the measurement system must be robust enough to deal with the environment inside the cylinder of a firing engine, and it should be capable of tracking the very rapid

changes in charge temperature that occurs during the compression and expansion strokes.

The basic principle of thermometry is to bring a well-characterized material into thermal equilibrium with the body to be measured. The temperature measurement is made by measuring the change in some property of the well-characterized material. Thermocouples are the first choice for the measurement of gas temperature, but their response is too slow. The response of thermocouples is also very sensitive to the flow conditions surrounding the bead. Since the time lag is a function of the rate of heat transfer into the thermocouple, anything that affects the heat transfer, such as turbulence levels, affects the response time. This effect makes correction for the time lag difficult [22]. High-speed thin film resistance temperature sensor is also demonstrated for measurement of gas temperature. The in-cylinder gas temperature measurement has been dominated by optical and acoustic measurement [16, 22]. Optical temperature measurement techniques are based on the emission and absorption, either singly or in combination, of light in the infrared through an ultraviolet range of the spectrum. The use of spectroscopic techniques is limited to optically thin gases due to the self-absorption. On the other hand, radiation thermometers are suited for thick gases where emissivity or absorptivity of gas can be measured accurately. Temperature measurement by spontaneous Raman scattering (SRS), laser Rayleigh scattering (LRS), coherent anti-Stokes Raman scattering (CARS), and laser-induced fluorescence (LIF) has been developed [16]. Acoustic techniques make use of the variation in the speed of sound with the temperature of a gas. The time of flight of an acoustic pulse, as well as acoustic resonance, can be used for determination of gas temperature [23].

7.4 Wall Heat Transfer Estimation

In reciprocating combustion engines, the heat transfer from the combustion gases to the cylinder walls is an important factor in the engine's design because it affects fuel conversion efficiency, power, and emissions. Thus, a lot of studies are focused on investigating an accurate model of the heat transfer, for engine design and optimization purposes [24]. Several potential advantages can be gained by accurate thermal predictions such as improved cooling systems (lighter and small pumps as well as heat exchangers), lower thermal distortion (reduced friction and optimized piston ring assembly), and advances in engine simulation and modeling (by applying correct boundary conditions) [25]. These advantages definitely contribute to improving fuel economy and reducing engine emissions. The thermal condition of the combustion chamber is closely tied to heat transfer from the hot gas to the walls. Thus, a good understanding of the heat transfer process in the combustion chamber is prerequisite for developing advanced engine control strategies and thermal management scheme.

The heat transfer from combustion gases to the coolant in reciprocating internal combustion engines represents between one-fourth and one-third of the total energy released by the mixture of fuel and air during combustion. The entire heat rejection to the cooling fluid depends mainly on engine type and operating conditions. The modes of heat transfer are typically involved in the heat transfer process from combustion gases to the coolant through metallic components of the engine. Heat transfer from combustion gases to liner takes place mainly by forced convection with a contribution by radiation. Heat transfer by radiation mode is dominant in conventional diesel engines because of the generation of highly radiative soot particles. The radiative heat transfer accounts for only 5% of the total heat flux in an SI engine, and it is usually neglected [26]. Heat transfer from the liner to coolant takes place by conduction mode.

Heat transfer in combustion engines is a nonuniform and unsteady process because heat flux between combustion gases and metallic surface (liner) varies in time and space significantly during an engine cycle. In-cylinder heat fluxes oscillate between a few MW/m^2 during combustion and close to zero or even negative during intake stroke [25]. Heat flux measurement and analysis of heat transfer are typically conducted during engine operation in motored condition and fired conditions. In motoring operation, the engine is driven by external power (such as an electric motor). Measurements in motoring operating conditions are taken to investigate the effect of the gas properties and the gas flow (without the influence of combustion) on heat transfer. Figures 7.8 and 7.9 show the factors affecting the heat flux in motoring and firing operating conditions, respectively. The factors affecting the heat flux are categorized into three main groups, namely, (1) in-cylinder flow, (2) gas properties, and (3) temperature difference between the combustion gases and the cylinder wall [24].

In-cylinder flow and gas properties play role in convective heat transfer and affect the convective heat transfer coefficient. To determine the factors that can be actually varied on the engine, the three groups are further expanded. Various factors affecting the heat flux in reciprocating engines are divided into three categories, namely, (1) controllable factors, (2) uncontrollable factors (ambient conditions), and (3) unchangeable factors (fixed for a particular engine). The pathways from these three types of factors to the top can be used to describe the trends in the heat flux in motored and fired operating conditions (Figs. 7.8 and 7.9). The ambient conditions are typically fixed during experiments. In motoring operating condition, three independent parameters, i.e., (1) the throttle position (TP), (2) the compression ratio (CR), and (3) the injected gas (type and quantity), can be changed for varying the heat flux. In firing operating conditions, the ignition timing (IGN), excess air ratio (λ), fuel type, engine load, and EGR are the additional variables that can be controlled to affect the heat flux (Fig. 7.9). In motored conditions, no significant spatial variation is observed, and thus, measurement at one location can be conduction. However, significant spatial variation occurs in heat flux during firing operation [24].

Figure 7.10 depicts the effect of excess air ratio on the peak heat flux, which is presented as a normalized value along with the measurement location from three

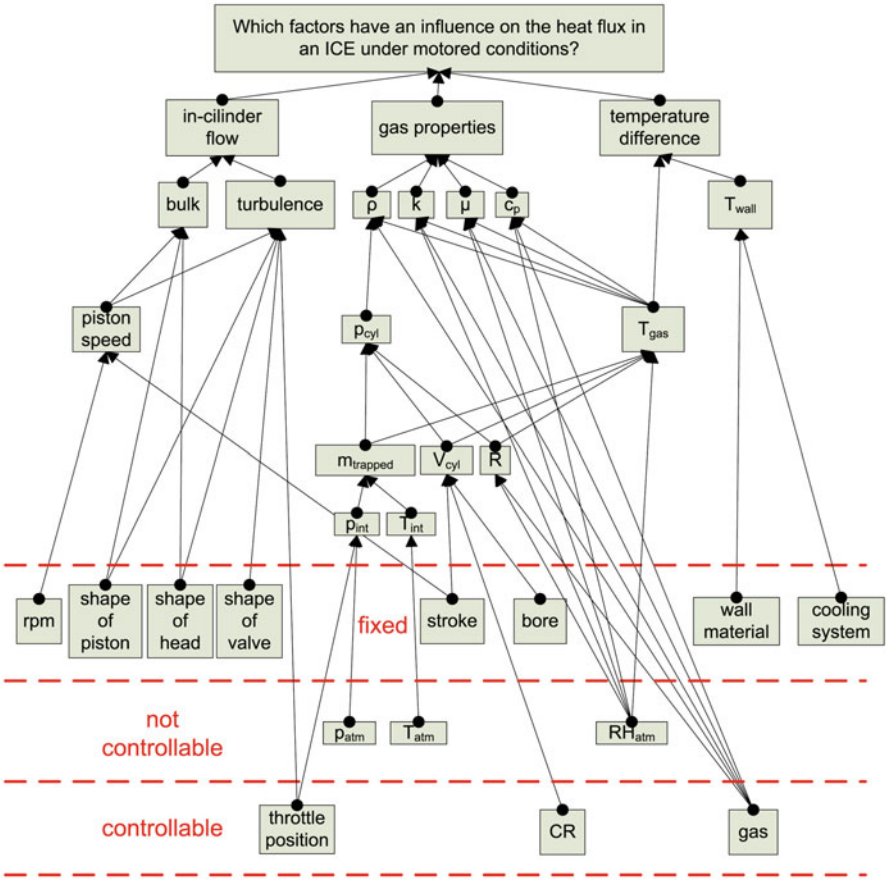

Fig. 7.8 Identification of the factors affecting the heat flux under motored engine operation [24]

studies. The figure depicts a maximum in the peak heat flux as with mixture richness. The maxima of peak heat flux around $\lambda = 1$ can be attributed to adiabatic temperature (highest for stoichiometric mixtures) and flame speed (the highest for richer mixtures) [24].

Engine speed significantly affects the heat transfer from the walls. The peak and total cycle heat flux increases with engine speed that is attributed to an increase in gas velocity and turbulence [24, 27, 28]. The increase in heat transfer happened mainly at the beginning of the expansion stroke, possibly due to the higher gas temperatures in that part of the engine cycle. The variation in spark timing around MBT affects both the rise and the peak value of the heat flux [27]. The operational properties are affected by increasing compression ratio such as (1) surface-to-volume ratio around TDC, (2) the gas pressure, (3) peak burned gas temperature, (4) gas motion increase, (5) faster combustion, and (6) the decrease in gas temperature late

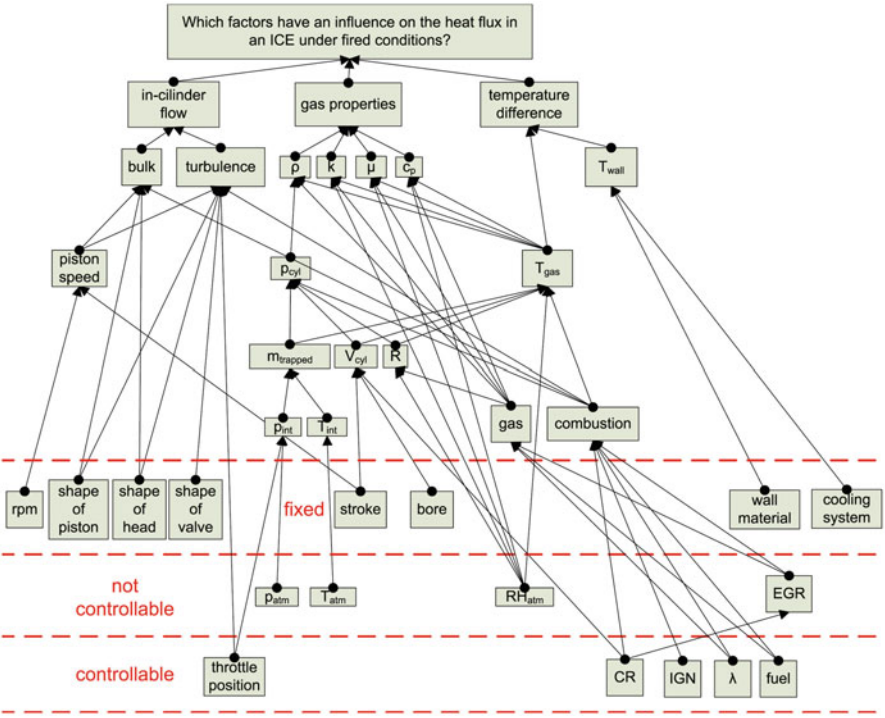

Fig. 7.9 Identification of the factors affecting the heat flux under fired engine operation [24]

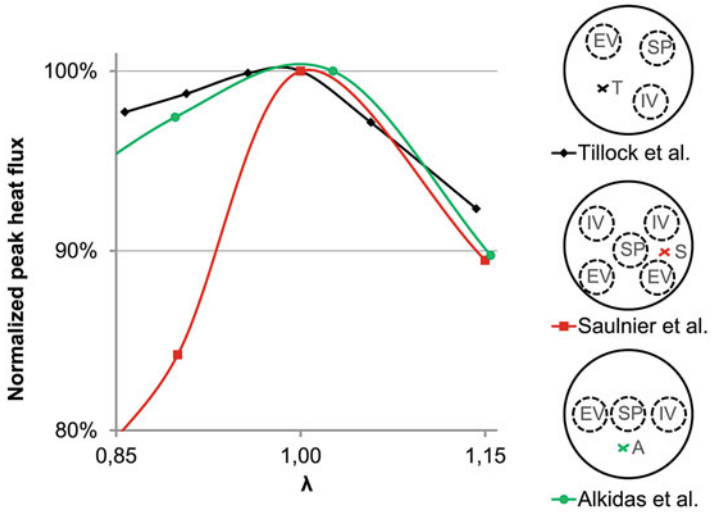

Fig. 7.10 Variation of normalized peak heat flux with excess air ratio (λ) [24]

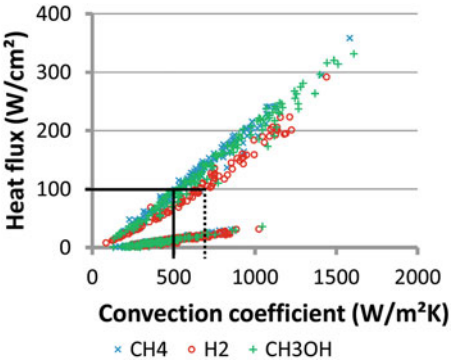

Fig. 7.11 The variation of convection coefficient for different fuels [29]

in the expansion stroke. The first five properties increase the heat transfer; the last one decreases it [24].

Convective heat transfer is also affected by fuel used for operating the engine. Figure 7.11 shows the heat flux is with the convection coefficient for the three fuels at different engine operating conditions. Heat flux is measured for all the condition at the same location. Figure 7.11 depicts that a certain heat flux level consistently corresponds with a higher convection coefficient for hydrogen (illustrated in Fig. 7.11 at a level of 100 W/cm^2). The convection coefficient of methane is significantly lower than hydrogen at particular heat flux. It suggests that for the same difference between the gas and wall temperature, the heat flux of hydrogen will be higher in comparison to methane [29].

Figure 7.12 illustrates the spatial variation in heat flux in a particular combustion cycle and cyclic variation in heat flux at a particular engine operating condition. Figure 7.12a depicts two local maxima in the heat flux traces at P2 and P4 positions. The P1 position corresponds to the spark plug installation. The first peak appears when flame passes over the measurement position and the second peak occurs when the temperature difference between combustion gases and wall reaches to maximum [29]. The maximum of gas temperature occurs before the flame reaches to the P3 position, and thus, it has only one maximum point in the curve (Fig. 7.12a).

Figure 7.12b depicts the typical cyclic variations in the measured pressure and heat flux. The cycle-averaged traces are shown with a solid red line; the cycles which differ the most (max and min) and the least (best) from the mean cycle are plotted with dashed black lines. The figure shows that there is a much steeper rise in the heat flux trace at the instant of the flame arrival in the case of individual cycles. This rise is not that steep in the case of the mean cycle due to the cyclic variations in the time of the flame arrival [29].

The convective heat transfer is a transient process but can be assumed to be quasi-steady. The rate of heat loss through the cylinder walls can be calculated using Eq. (7.30).

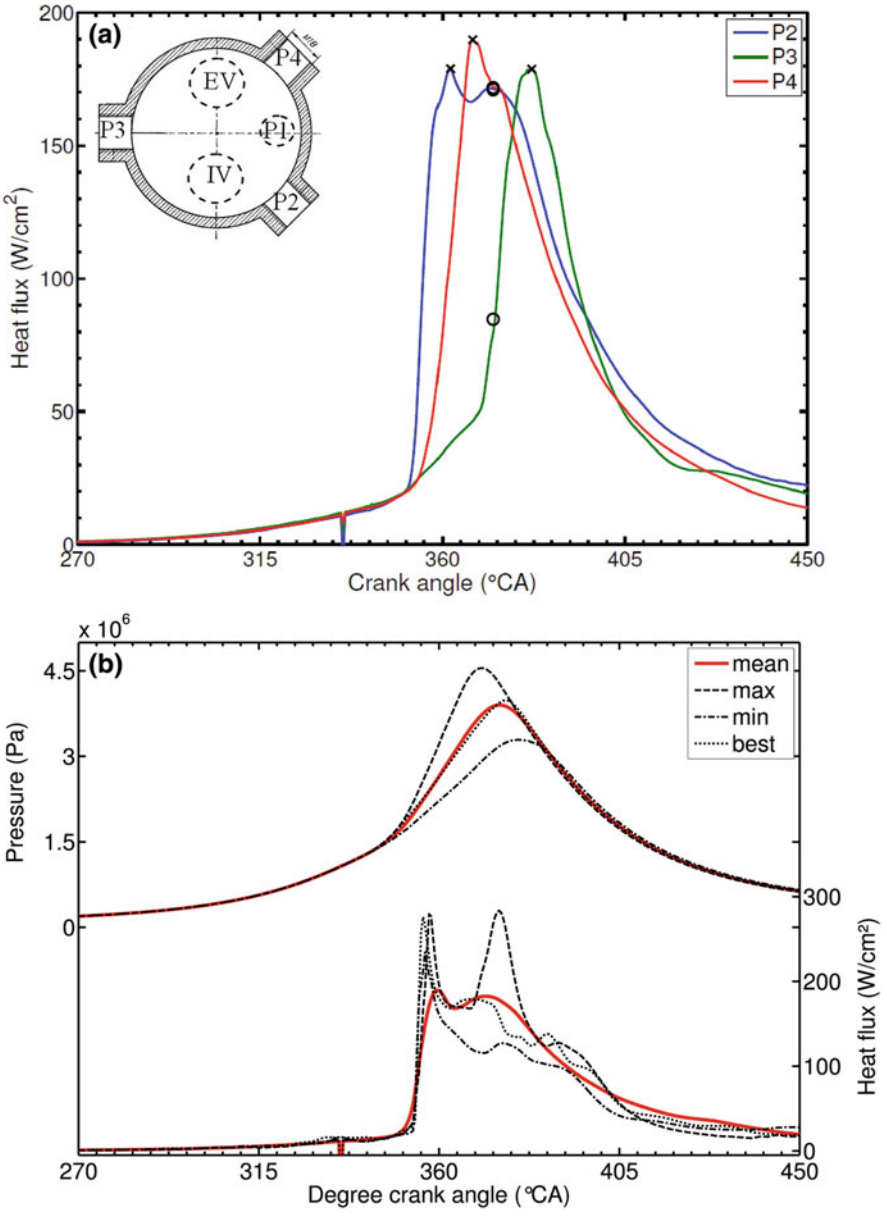

Fig. 7.12 (**a**) Spatial variation of heat flux at particular engine cycle and (**b**) cyclic variation in heat flux at particular engine operating condition [29]

$$\frac{\partial Q_{\mathrm{ht}}}{\partial \theta} = \frac{h(T - T_{\mathrm{w}})A}{360N} \quad [\mathrm{J/CAD}] \tag{7.30}$$

where h is heat transfer coefficient, T_{w} is the average cylinder wall temperature, A is the actual cylinder wall area, and N is the engine speed. It is normally assumed that T_{w} is constant over the entire cycle. h, T, and A are functions of crank angle position [1].

The most commonly used heat transfer models are empirical models that calculate the spatially averaged heat flux as a function of crank angle.

One of the early empirical models for the heat transfer coefficient is proposed by Eichelberg [30] which is given by Eq. (7.31).

$$h = \alpha_{\mathrm{s}} \cdot {S_{\mathrm{p}}}^{1/3} \cdot P^{1/2} \cdot T^{1/2} \tag{7.31}$$

where S_{p} is the mean piston speed, α_{s} is scaling factor, and P and T are pressure and temperature of the combustion chamber, respectively. The scaling factor depends on engine and combustion modes. The value of α_{s} is 0.25 in reference [31], and 7.67×10^{-3} is used in reference [32]. The scaling factors need to be calibrated for a particular engine. This model provides acceptable accuracy and easier to use and compute [32].

Heat transfer coefficient can be estimated by Hohenberg model which is shown in Eq. (7.32) [33].

$$h = \alpha_{\mathrm{s}}\, V^{-0.06} P^{0.8}\, T^{-0.4} \left(S_{\mathrm{p}} + 1.4\right)^{0.8} \tag{7.32}$$

Here S_{p} is the mean piston speed, α_{s} is scaling factor, and P, V, and T are pressure, volume, and temperature of combustion chamber, respectively. Another correlation that is normally used for computation of heat transfer coefficient by Woschni model [34] and presented by Eq. (7.33).

$$h = 131 \times (\mathrm{Bore})^{-0.2} \times P^{0.8} \times T^{-0.55} W^{0.8} \tag{7.33}$$

where

$$W = C_1 \times 2.28 \times S_{\mathrm{p}} + C_2 \times 3.24 \times 10^{-3} \times \frac{V_{\mathrm{d}}}{V_{\mathrm{IVC}}} \times \left(\frac{P - P_{\mathrm{mot}}}{P_{\mathrm{IVC}}}\right) \times T_{\mathrm{IVC}} \tag{7.34}$$

where S_{p} is the mean piston speed and C_1 and C_2 are constants. Typically, heat loss through the crevices is assumed to be small and neglected.

Generally, all the models are based on the Pohlhausen equation (7.35) which characterizes the convective heat transfer on a flat plate using the boundary layer theory [35].

$$Nu = a \cdot Re^b \cdot Pr^c \tag{7.35}$$

where a, b, and c are model coefficients and Nu, Re, and Pr, are the Nusselt number, Reynolds number, and Prandtl number, respectively. Prandtl number is typically lumped with scaling constant "a" because it does not change significantly throughout the engine cycle for most fuels [29]. Thus, empirical correlations for the convective heat transfer coefficient can be presented as a function of a characteristic length L, a characteristic velocity V_{ch}, the thermal conductivity k, the dynamic viscosity, and the density of the combustion gases (Eq. (7.36)).

$$h = a \cdot {V_{ch}}^b \cdot L^{b-1} \cdot k \cdot \mu^{-b} \cdot \rho^b \tag{7.36}$$

Various proposed models differ with the selection of characteristics length and velocity and estimation of thermal properties of the charge. The model coefficient is typically computed by regression with experimental data.

The Eq. (7.36) can be approximated as Eq. (7.37) by certain assumptions about the thermal properties [35].

$$h = a \cdot {V_{ch}}^b \cdot L^d \cdot T^e \cdot P^b \tag{7.37}$$

The characteristics length (L) and velocity (V_{ch}) along with model coefficients for several models are proposed in reference [35].

Annand [36] proposed a correlation for both SI and CI engines, the constant b depends on the type of engine, and the heat transfer coefficient is given by Eq. (7.38).

$$h = a \cdot \frac{k}{B} Re^{0.7} + b \frac{\left(T^4 - {T_w}^4\right)}{\left(T - T_w\right)} \tag{7.38}$$

where T and T_w are the temperature of combustion gases and wall, k is thermal conductivity of gases, and B is the bore of the engine. For SI engines, the values of $a = 0.35$–0.8 and $b = 4.3 \times 10^{-9}$ W/m^2 K^{-4}.

Bargende [37] proposed another model for the heat transfer coefficient as shown by Eq. (7.39).

$$h = 3.5212 \cdot P^{0.78} \cdot \left(0.5\sqrt{8k_{spec} + {S_p}^2}\right) \cdot \left(V^{1/3}\right)^{-0.22} \cdot T^{-0.477} \tag{7.39}$$

where k_{spec} is the specific kinetic energy [m^2/s^2], S_p is mean piston speed, and P, V, and T are pressure, volume, and temperature, respectively.

Chang [38] proposed a new heat transfer coefficient for HCCI combustion by modifying the Woschni model. It was found that the original Woschni model cannot match well measurements in the HCCI engine since the unsteady gas velocity term causes overprediction of heat transfer during combustion. This in turn leads to

underprediction during compression and hence undesirable consequences regarding predicting ignition. The proposed model is given in Eq. (7.40).

$$h = \alpha_s \cdot P^{0.8} \cdot \left(c_1 \cdot S_p + c_2 . \frac{V_s \cdot T_r}{P_r \cdot V_r} \cdot (P - P_0) \right)^{0.8} \cdot L_c{}^{-0.2} \cdot T^{-0.73} \tag{7.40}$$

where L_c is the instantaneous combustion chamber height.

A study applied the models of Chang, Hohenberg, and Woschni in a single-zone engine simulation of HCCI engine and showed that the shape of the heat flux curve predicted by Hohenberg and Chang model is very similar if the same length scale is used [39]. Figure 7.13 shows the variation of heat flux with a crank angle for different heat transfer coefficient model in motored and fired operation of HCCI engine. Figure 7.13a shows that the models of Woschni, Hohenberg, Chang, and Hensel underestimate the heat flux throughout the entire combustion cycle, except during the final part of the expansion phase. Subsequently, these models underestimate both the maximum heat flux and the total heat loss [35]. The Bargende model overestimates the heat flux in the whole combustion cycle in motoring conditions. Figure 7.13a clearly shows that none of the models can be used without calibrating the scaling coefficient first. After calibration in motoring conditions, the coefficient is used for heat flux estimation in fired engine operation (Fig. 7.13b). The models of Annand, Hohenberg, and Bargende are able to capture the effect of the combustion on the heat transfer. The models accurately predict the maximum heat flux during fired operation using the scaling coefficient found during motored operation [35].

A detailed assessment of the models of convective heat transfer coefficients can be conducted by presenting the Nusselt number as a function of the Reynolds number on a logarithmic scale. The relationship between the Nusselt and the Reynolds number must be a straight line on a logarithmic scale if the model perfectly predicts the convection coefficient because all the models are based on the power law as shown in Eq. (7.35) [35]. Figure 7.14 depicts the variation of the Nusselt with Reynolds number for the models of Annand, Woschni, and Bargende. Yellow square and red dot show the SOC and the EOC, respectively. The Annand and Woschni models show a distinct horseshoe shape with two straight legs around the top dead center position, representing the compression and the expansion phase (Fig. 7.14). Subsequently, a better model for heat transfer coefficient can be achieved if different coefficients a and b are used for the compression and expansion phase [35]. The linear relationship only occurs during the compression and expansion immediately before and after the combustion. The prediction of the heat flux cannot be improved in the other regions by using different values for the coefficients a and b (Eq. 7.35).

Knocking engine operating conditions affected the cylinder heat transfer, and it significantly increases. A study found that knock intensities above 0.2 MPa influenced the heat flux, and at knock intensities above 0.6 MPa, the peak heat flux was 2.5 times higher than for a non-knocking cycle [40]. The influence of knocking on heat flux is believed to be due to an increased charge motion as a result of the autoignition. This influences the heat transfer coefficient as the Reynolds

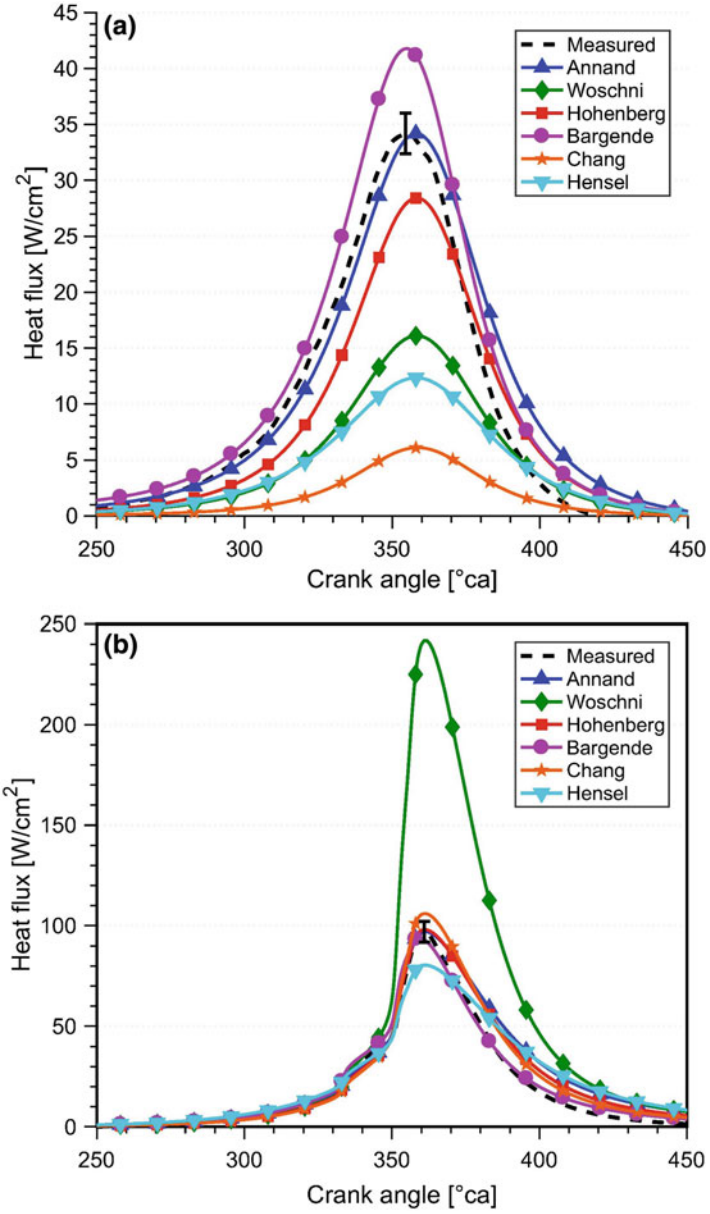

Fig. 7.13 Variation of heat flux during (**a**) motoring operation and (**b**) firing operating conditions with coefficients for motored operation [35]

number is increased. There were no evident indications that the heat flux was affected by the direction of the pressure waves in relation to the wall at which measurements were made.

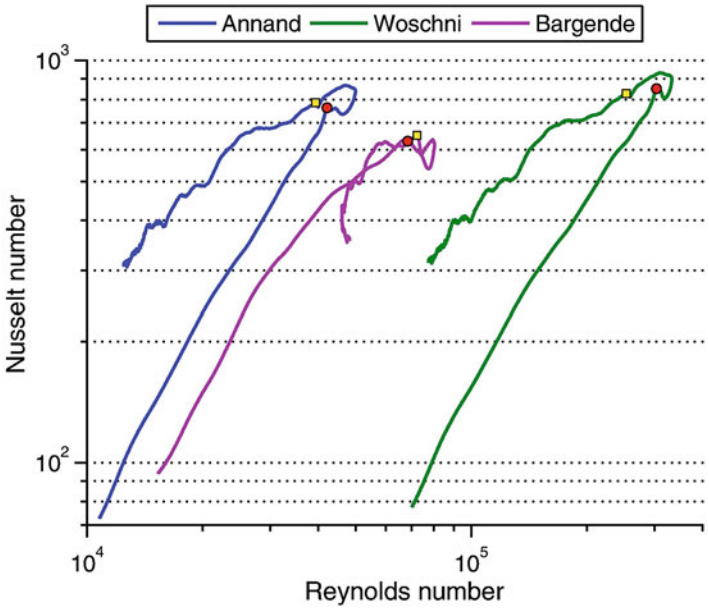

Fig. 7.14 Nusselt and Reynolds number on a logarithmic scale [35]

A study separated the heat loss into the loss due to normal heat transfer and into the loss due to knock in an HCCI engine [31]. Total heat transfer is separated into the normal convection heat transfer and the effect of knock by using the heat transfer coefficient (Eq. 7.41), by turn the term of dp/dt (pressure rise rate) in the coefficient on and off.

$$\begin{aligned} h &= C_1 \cdot {S_\mathrm{p}}^{1/3} \cdot P^{1/2} \cdot T^{1/2} \cdot \left(1 + \frac{dp/dt}{C_2}\right) \\ dp/dt &= dp/dt \quad (dp/dt > 0) \\ dp/dt &= 0 \quad (dp/dt \leq 0) \end{aligned} \tag{7.41}$$

It is demonstrated that changes in heat transfer rate can be expressed by knock in the HCCI engine with adding a term of *dp/dt* (pressure rise rate) to heat transfer coefficient by Eichelberg model [31].

Another study investigated the effect in-cylinder pressure oscillations have on piston heat transfer using two fast-response surface thermocouples embedded in the piston top for transient temperature measurement [41]. To quantify the magnitude of in-cylinder pressure oscillations, the metric of signal energy (SE) is introduced. The SE is calculated by integrating the power spectral density (PSD) over the first resonant mode. The limits of integration were selected to be 5.3 and 8.0 kHz, as denoted by a subscript designation specifying the frequency range, $SE_{5.3–8.0}$.

$$SE_{5.3-8.0} = \int_{5.3}^{8.0\ \text{kHz}} \text{PSD} \cdot df \tag{7.42}$$

Increase in the closed-cycle integrated heat flux is found with an increase in $SE_{5.3–8.0}$, which strongly suggests that the higher pressure oscillations are increasing the heat transfer rate [41]. It was found that before SOC, the heat transfer coefficient was effectively the same for cycles with high and low $SE_{5.3–8.0}$ at the same cylinder pressure. However, after combustion, the cycles with high $SE_{5.3–8.0}$ showed higher heat transfer coefficients than those with low $SE_{5.3–8.0}$ at the same pressure. This strongly suggests a correlation with the cylinder pressure oscillations.

7.5 Heat Release Rate Analysis

Cylinder pressure traces have been used for a long time to monitor the combustion event and extract information regarding burn rate, combustion phasing, and combustion duration. Heat release analysis by using a pressure sensor signal is a well-recognized technique for evaluation of the combustion event and also for combustion diagnostics. In this section, calculation of heat release from measured cylinder pressure data is discussed.

7.5.1 Rassweiler and Withrow Model

Rassweiler and Withrow (RW) heat release model is an approximate model that is loosely based on the Rassweiler and Withrow mass fraction burnt model (Sect. 7.2.2). The equation for heat release uses the same basic combustion pressure rise equation as the standard RW equation which is based on the assumption that the pressure changes due to (1) piston motion and (2) charge to wall heat transfer can be represented by polytropic processes [3]. However, the heat release equation does not assume that the proportion of fuel burned is proportional to the increase in the corrected combustion pressure. The main assumptions in RW heat release model are (1) the combustion can be idealized as being divided into a number of constant volume combustion processes and (2) the pressure change due to piston motion and charge to wall heat transfer can be modeled as a series of polytropic processes [3, 42].

The pressure rise between two positions 1 and 2 in the engine cycle due to combustion can be written as Eq. (7.43) by assuming pressure change due to compression can be represented by a polytropic process with polytropic index n [3].

$$\Delta P_2 = P_2 - P_1 \left(\frac{V_1}{V_2}\right)^n \tag{7.43}$$

Assuming ideal gas relationships, the incremental temperature rise (ΔT_2), due to combustion, can be approximated by Eq. (7.44).

$$\Delta T_2 = \frac{\Delta P_2 \cdot V_2}{m \cdot R} \tag{7.44}$$

Equation (7.44) is an approximation because it assumes R is a constant and the combustion occurs at a fixed volume. The incremental heat release energy ($\Delta Q_{\mathrm{hr},2}$), required to produce the temperature rise, can be achieved by using the first law for the assumed constant volume process as shown in Eq. (7.45) [3, 42].

$$Q_{\mathrm{hr},2} = m \cdot C_{\mathrm{v}} \cdot \Delta T_2 = \frac{V_2}{\gamma - 1} \cdot \left\{ P_2 - P_1 \left(\frac{V_1}{V_2}\right)^n \right\} \tag{7.45}$$

Equation (7.45) provides the approximate incremental gross heat release energy for the crank angle interval from θ_1 to $\theta_{2,}$ and this can be integrated over the combustion period to get cumulative gross heat release. The net cumulative heat release can be obtained if the polytropic index (n) is replaced by the ratio of specific heats (γ) which ignores the heat transfer [3, 42].

A potential advantage of this equation is that charge to wall heat transfer is included for in the polytropic index term. To be most accurate, this term would need to be varied continuously during the heat release calculations, but it is assumed here that using the measured polytropic coefficients immediately prior to ignition and shortly after the end of combustion (EOC) can be used without significant loss of accuracy [3].

Figure 7.15 illustrates the effect of the polytropic index (assumed constant value over the entire cycle) on gross heat release curve which is computed using Eq. (7.45) with the calculated polytropic index with temperature-dependent γ. The figure depicts that the polytropic index variation considers the effect of the heat transfer, which has a large effect on the heat release rate after the EOC. However, the advantage of this model over the heat transfer term in the first law equation is that the polytropic index can be determined from the measured pressure-volume data, and thus, calculated values for each cycle can be used rather than assumed and probably erroneous values [3, 42].

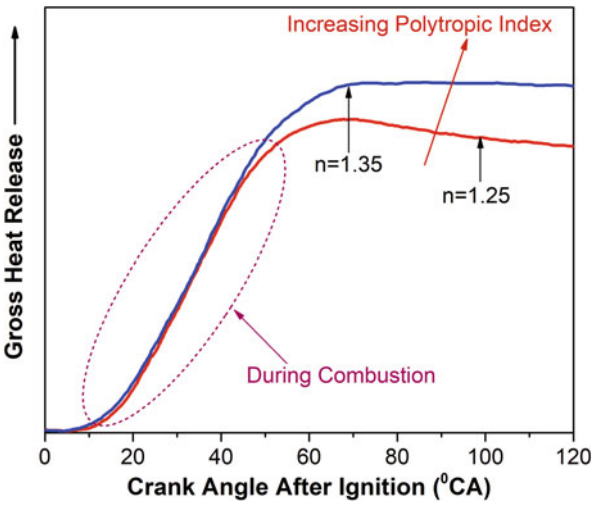

Fig. 7.15 Effect of assumed fixed polytropic index on the cumulative gross heat release calculated by Eq. (7.45) with temperature-dependent γ (adapted from [3])

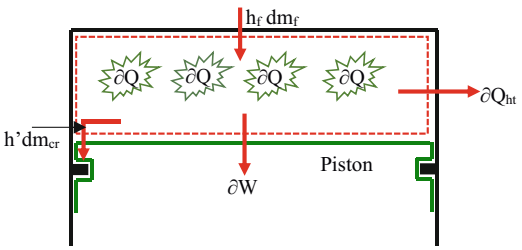

Fig. 7.16 Energy balance for engine combustion chamber with chemical heat release

7.5.2 *Single-Zone Thermodynamic Model*

Simple single-zone models are usually employed in preference to the potentially more accurate multidimensional thermodynamic models due to their lower complexity and because they are numerically more efficient and normally yield similar results. The single-zone models do not include spatial variations and, thus, assume uniform charge temperature and composition in the entire combustion chamber. The first law of thermodynamics is employed to cylinder gases by assuming the combustion chamber as control volume as shown in Fig. 7.16. The state of the cylinder is defined in terms of average properties and does not differentiate the burned and unburned gases. The engine cylinder is assumed as a single zone, where no temperature gradient occurs and the reactants and products are completely mixed [2, 16, 43]. Single-zone model offers the advantage of including heat transfer and gas flow phenomena more simply. The combustion process is considered as separate heat addition process and contents of the cylinder as single fluid. The classical first law equation for the in-cylinder charge during the non-flow period between inlet valve closure (IVC) and exhaust valve closure (EVC) can be written for an incremental crank angle interval.

The gross chemical heat released (Q) due to combustion can be presented by Eq. (7.46) [16, 43].

$$\partial Q = dU_s + \partial W + \sum h_i \cdot dm_i + \partial Q_{ht} \tag{7.46}$$

Here U_s is the sensible energy of the charge (which means change in internal energy (u) or enthalpy (h) due to change in temperature alone and changes due to chemical reaction or phase change are ignored), ∂Q_{ht} is the heat transfer to the cylinder walls, and ∂W is the work on the piston, which is equal to pdV. The mass flux term indicates the flow across the system boundary, which includes crevice flows and injected fuel in case of direct fuel injection engines.

$$\sum h_i \cdot dm_i = \left(h' dm_{cr} - h_f dm_f\right) \tag{7.47}$$

Assuming U_s can be written as $m{\cdot}u(T)$, where T is the average charge temperature of the cylinder gases and m is the mass within the system boundary and u is internal energy.

$$dU_s = dm \cdot u + mC_v dT \tag{7.48}$$

For SI engines running on premixed charge, dm is caused by flows in and out of the crevices ($dm = -dm_{cr}$). The Eq. (7.46) can be written as Eq. (7.49).

$$\partial Q = mC_v dT + P \cdot dV + (h' - u) dm_{cr} + \partial Q_{ht} \tag{7.49}$$

By assuming that combustion gases follow the ideal gas law ($PV = mRT$), changes in temperature can be calculated by Eq. (7.50).

$$\frac{dT}{T} = \frac{dP}{P} + \frac{dV}{V} - \frac{dm}{m} \tag{7.50}$$

By substituting the Eq. (7.50) to Eq. (7.49), the heat release equation can be written as Eq. (7.51).

$$\partial Q = \left(1 + \frac{C_v}{R}\right) P \cdot dV + \frac{C_v}{R} dP \cdot V + \left(h' - u + C_v T\right) dm_{cr} + \partial Q_{ht} \tag{7.51}$$

Since gases are assumed as an ideal gas, then $C_p + C_v = R$, and $\gamma = C_p/C_v$. Substituting the values of γ, the final heat release rate equation is written as Eq. (7.52).

$$\frac{dQ}{d\theta} = \frac{\gamma}{\gamma - 1} P \cdot \frac{dV}{d\theta} + \frac{1}{\gamma - 1} \frac{dP}{d\theta} \cdot V + \left(h' - u + C_v T\right) \frac{dm_{cr}}{d\theta} + \frac{\partial Q_{ht}}{d\theta} \tag{7.52}$$

The ratio of specific heat (γ) is the most important property used in the heat transfer calculation. The values of γ depend on temperature and the composition of charge (fuel, EGR, air-fuel ratio, ratio of reactant to combustion products). For spark ignition engine, the values of γ are obtained by matching single-zone model analysis to that of a two-zone model analysis for different fuels [44]. The calculation of heat transfer term in Eq. (7.52) is discussed in Sect. 7.4.

Crevice effect can be modeled by assuming the overall effect of crevice volume as single aggregate crevice volume, where the gas pressure is same as cylinder pressure, but the temperature is same as the wall temperature (T_w) [43].

$$m_{cr} = \frac{P \cdot V_{cr}}{R \cdot T_w} \quad \text{or} \quad dm_{cr} = \left(\frac{V_{cr}}{R \cdot T_w}\right) dP \tag{7.53}$$

Assuming $\gamma(T) = a + bT$, the factor by which dm_{cr} is multiplied in Eq. (7.51) can be expressed as Eq. (7.54) [43].

$$\left(h' - u + C_v T\right) = T' + \frac{T}{\gamma - 1} - \frac{1}{b} \ln\left(\frac{\gamma - 1}{\gamma' - 1}\right) \tag{7.54}$$

where the "primed" quantities are evaluated at cylinder conditions when mass is out of the control volume and evaluated at crevice condition when it re-enters the chamber.

Substituting the Eq. (7.54), the final gross heat release equation can be written as Eq. (7.55).

$$\frac{dQ}{d\theta} = \frac{\gamma}{\gamma - 1} P \cdot \frac{dV}{d\theta} + \frac{1}{\gamma - 1} \frac{dP}{d\theta} \cdot V + V_{cr}\left(T' + \frac{T}{\gamma - 1} - \frac{1}{b} \ln\left(\frac{\gamma - 1}{\gamma' - 1}\right)\right) \frac{dP}{d\theta} + \frac{\partial Q_{ht}}{d\theta} \tag{7.55}$$

The crevice volume is often ignored in the heat release analysis. The charge to wall heat transfer is often ignored for simplicity, and the heat release determined by ignoring crevice losses and wall heat transfer is referred to as "net" or "apparent" heat release. The net heat release equation can be represented by Eq. (7.56).

$$\frac{dQ_n}{d\theta} = \frac{\gamma}{\gamma - 1} P \cdot \frac{dV}{d\theta} + \frac{1}{\gamma - 1} \frac{dP}{d\theta} \cdot V \tag{7.56}$$

The net heat release equation is the same for the direct injection engines also [16]. A zero-dimensional, three-zone heat release calculation utilizing thermodynamic equilibrium for direct injection (DI) compression ignition engine has been proposed [45]. In this method, an Arrhenius-based equation used to evaluate the rate

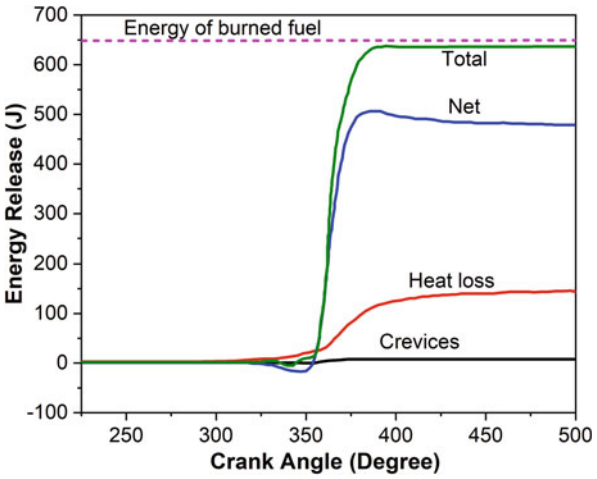

Fig. 7.17 Cumulative heat release profile with net heat release calculated from the zero-dimensional model ($\phi = 0.35$, fuel consumption of 0.015 g/cycle, 1800 rpm, 0% EGR, and intake temperature of 18 °C) [47]

of fuel mass consumed by the combustion process, allowing the model to estimate the rate of change of the chemical species within the cylinder, which provides the properties of the bulk gas at a given crank angle for thermodynamic analysis. Another study proposed a corrected temperature-based heat release analysis in HCCI engine using equilibrium composition of species as a function of crank angle position [46].

The cumulative heat release can be calculated by integrating the heat release rate. Figure 7.17 illustrates the typical cumulative heat release as a function of crank angle position in the HCCI engine. This figure also depicts the net heat release and the losses due to heat transfer as well as crevices. Figure 7.17 shows that crevice loss can be neglected due to very small contribution in the total heat release. The wall heat transfer significantly contributes to the total heat release depending on the engine operating conditions and combustion modes.

Specific heat ratio (γ) is another important factor that affects the heat release calculation using in-cylinder pressure measurement. The ratio of specific heat for single-zone model is computed by a more rigorous study using two-zone models [18, 44]. However, the simpler linear model can be used for calculation of γ by Eq. (7.57) [43].

$$\gamma = \gamma_0 - \frac{k}{100}\frac{T}{1000} \tag{7.57}$$

where γ_0 is the value of the ratio of specific heat at some reference temperature (typically 300 K), and it depends on charge composition. For atmospheric air, γ_0 is 1.4, and for lean air-fuel mixtures, 1.38 is a usable value. The constant k is usually set at 8.

Figure 7.18 illustrates the effect of γ without heat transfer consideration and the effect of heat transfer at fixed γ (1.28) on the cumulative heat release calculated using

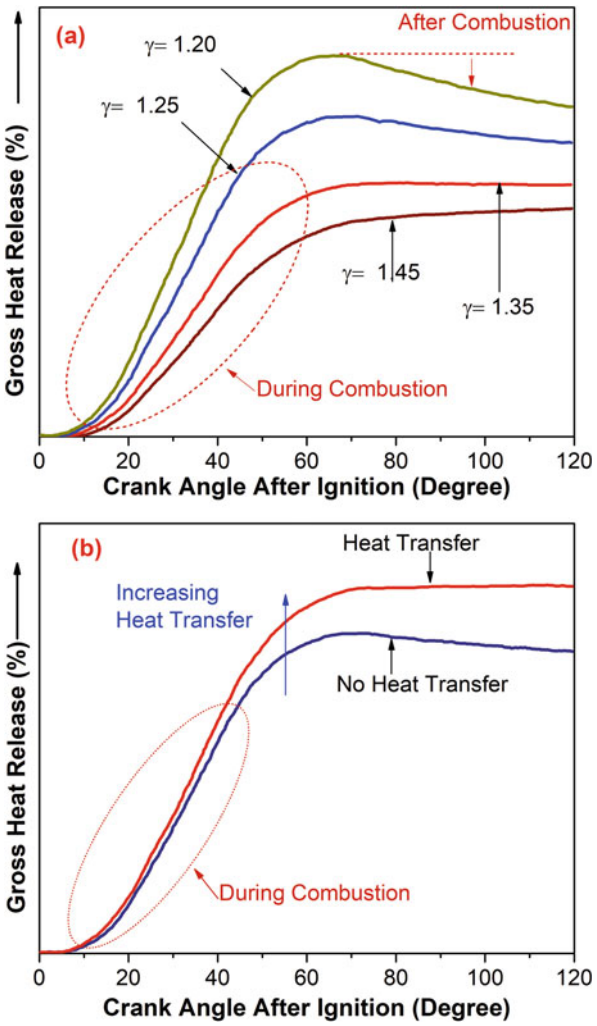

Fig. 7.18 (**a**) Effect of γ with no heat transfer and (**b**) effect of heat transfer at fixed γ (1.28) on the cumulative heat release calculated using single-zone model (adapted from [3])

single-zone thermodynamic model. Figure 7.18a shows that γ has a very large effect on both the magnitude of the heat release and the shape of the cumulative heat release curves. A low value of γ produces both (1) a heat release value which is too high and (2) a heat release rate which is negative after the completion of combustion. The opposite effect is present for high γ values although the effect is not linear with gamma, being inversely proportional to $(\gamma - 1)$ [3]. Figure 7.18b depicts that heat transfer has a significant effect on both the peak cumulative gross heat release and the gradient of the curves following the completion of combustion. It suggests that heat transfer effects must be included if accurate gross heat release values are to be obtained.

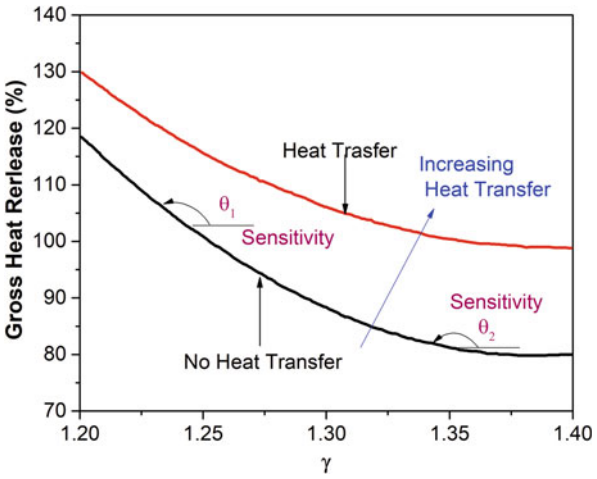

Fig. 7.19 Effect of γ and heat transfer rate on the cumulative heat release calculated using cylinder pressure by single zone model (adapted from [3])

Figure 7.19 demonstrates the effects of the γ and heat transfer rate by presenting the combined effects on the total (at 120° CA after ignition) cumulative gross heat release energy. The figure shows that there is a strong interaction between the γ and heat transfer with the calculated cumulative gross heat release. Sensitivity to γ is highest for conditions where γ is at its lowest (Fig. 7.19). Engine operation at richer mixture have lower γ values, and thus, relatively larger error is possible in heat release calculation. Therefore, accurate and repeatable gross heat release data can only be obtained if accurate values are used for both γ and heat transfer [3].

7.5.3 Real-Time Heat Release Estimation

The control system requirements of a modern engine are complicated because of the wide variety of combustion modes and fuel injection strategies that can be utilized to achieve high efficiency, low noise, or low emissions of oxides of nitrogen (NO_x) and soot. Any means to control the phasing of the combustion process in a desired crank angle window may help to alleviate the problems associated with the cyclic variation and can stabilize these combustion regimes. Thus, online calculation of combustion phasing is required, which can be calculated by calculation of real-time heat release. There are several methods for the online calculation of combustion phasing (discussed in Sect. 7.7) such as apparent heat release, RW methods, and pressure departure ratio [48].

Present combustion measurement system provides the heat release curves on real-time basis during engine experiments. Typically, apparent heat release is calculated on a real-time basis. The basic algorithm for fast net heat release is proposed and implemented by AVL based on single-zone model given by Eq. (7.58).

$$Q_i = \frac{K}{\gamma - 1}\{\gamma \cdot P_i \cdot (V_{i+n} - V_{i-n}) + V_i \cdot (P_{i+1} - P_{i-1})\} \tag{7.58}$$

where K is the constant (based on unit conversion) and n is the crank angle interval.

The heat release calculation based on RW model based on Eq. (7.45) can also be used for online heat release computation. The γ values as a function of temperature can also be used for the calculation of heat release. For control purposes, combustion phasing is required which can be calculated by computing cumulative heat release or mass fraction burnt.

7.5.4 Characteristics of Heat Release Rate in Different Engines

The heat release rate can be calculated from measured cylinder pressure data using a single-zone model for different combustion modes such as SI, CI, HCCI, or dual-fuel combustion. The typical shape of heat release rate trace depends on the combustion mode as well as engine operating conditions. Important conclusions can be drawn based on analyzing the heat release rate traces at different engine operating conditions.

Figure 7.20 shows the measured cylinder pressure and calculated heat release rate for spark ignition (SI) and laser ignition (LI) of natural gas for different relative air-fuel ratios (λ). The figure shows that the maximum cylinder pressure and maximum heat release rate increase with relatively richer mixture (decreasing λ) up to stoichiometric mixture ($\lambda = 1$) for both SI and LI. For mixture richer than stoichiometric ($\lambda < 1$), maximum cylinder pressure and maximum heat release rate decreased. The typical heat release rate curve is almost symmetric in conventional spark ignition engine for normal combustion using homogeneous charge (Fig. 7.20). Initially, combustion of charge begins at a slower rate and increases rapidly to a very high combustion rate around halfway of the combustion process. After achieving the maximum point, the heat release rate starts decreasing toward zero in almost identical fashion as it increased. This almost symmetric characteristic heat release curve is obtained for SI engine at different load and speed conditions. The typical combustion duration obtained is around 50 CAD in SI and LI combustion (Fig. 7.20).

Figure 7.21 shows the heat release rate traces for conventional diesel combustion and modern diesel engine with multiple fuel injection in a cycle. Modern diesel combustion systems typically utilize common rail direct injection (CRDI), high-pressure fuel injection systems with multiple injections per cycle, variable geometry turbines, alternate combustion modes, and advanced exhaust gas recirculation (EGR) handling techniques to enable compliance with the diesel emission standards [48]. The present trend is to split the heat release into multi-events or even to shift the heat release away from the TDC in order to achieve lower the combustion

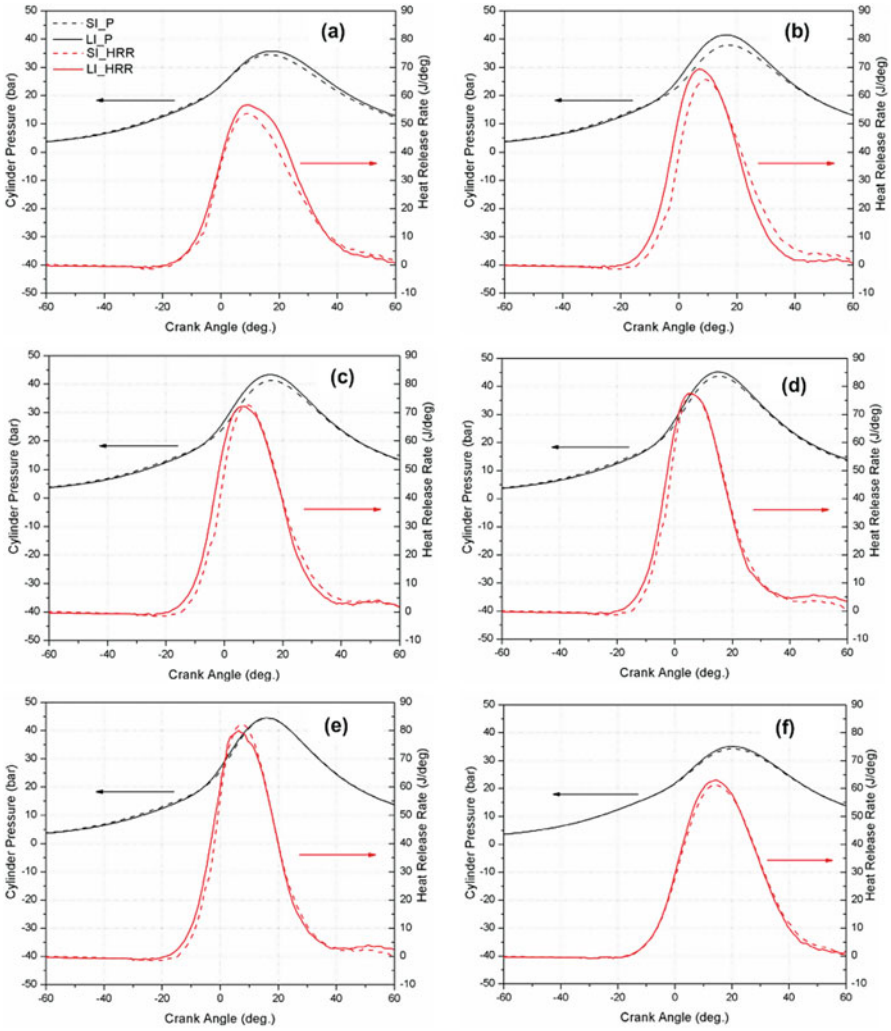

Fig. 7.20 Comparative variation of cylinder pressure and ROHR for SI and LI with crank angle position for (**a**) $\lambda = 1.35$, (**b**) $\lambda = 1.2$, (**c**) $\lambda = 1.15$, (**d**) $\lambda = 1.10$, (**e**) $\lambda = 1.00$, and (**f**) $\lambda = 0.90$ at ignition timing of 25° bTDC [49]

temperature to reduce NO_x emission and lower pressure rise rate [12]. The combustion phasing can be early or late depending on the boost pressure, EGR, and engine loads. Typical heat release rate curve in multiple injection strategy in diesel combustion is illustrated in Fig. 7.21b. In typical conventional diesel combustion with signal injection at a relatively lower injection pressure, the heat release consists of premixed combustion phase and diffusion-controlled combustion (Fig. 7.21). The peak of the premixed combustion phase depends on the ignition delay period, which depends on several factors such as fuel properties, injection timing, injection

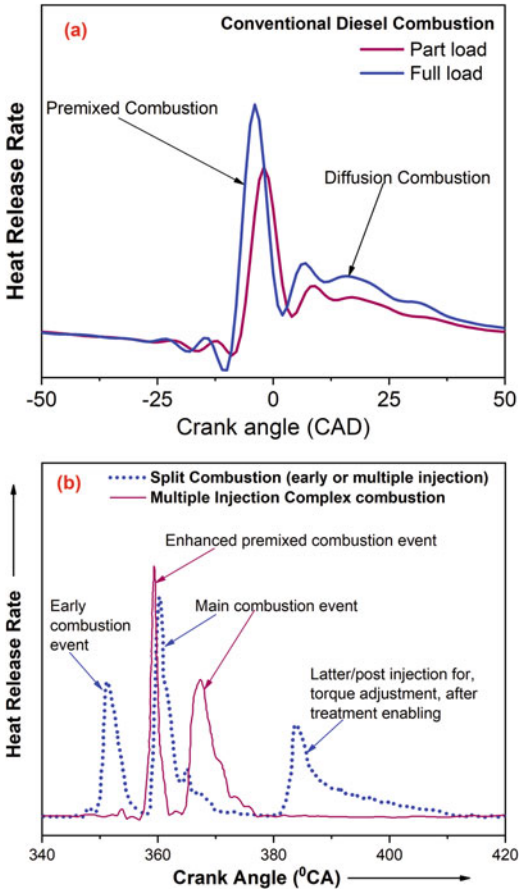

Fig. 7.21 Heat release rates for (**a**) conventional and (**b**) modern (multiple injection) diesel engines (adapted from [12])

pressure, engine load, etc. Thus, the combustion phasing and the combustion duration in modern diesel engine heavily depend on the mode of operation and fuel injection strategy. For example, the split injection can be used to control the combustion noise, while a retarded combustion phasing is essential to control the pressure rise rate and peak pressure at high boost pressure. Post-flame control can also be applied for torque modulation or the reduction of soot in certain cases (Fig. 7.21b) [12].

Figure 7.22 shows heat release rate traces at different λ in HCCI engine using ethanol and methanol. In the HCCI combustion, the charge is premixed, and combustion starts by autoignition. The typical shape of heat release curve in HCCI combustion is similar to SI combustion as both have almost symmetric characteristic heat release. However, in HCCI combustion the peak heat release rate is high, and the combustion duration is less than half (in terms of CA) of the combustion duration in SI engine. Figure 7.22 shows that the heat release rate and peak pressure rise rate increase as the mixture becomes richer (decrease in λ). Both fuels (ethanol and

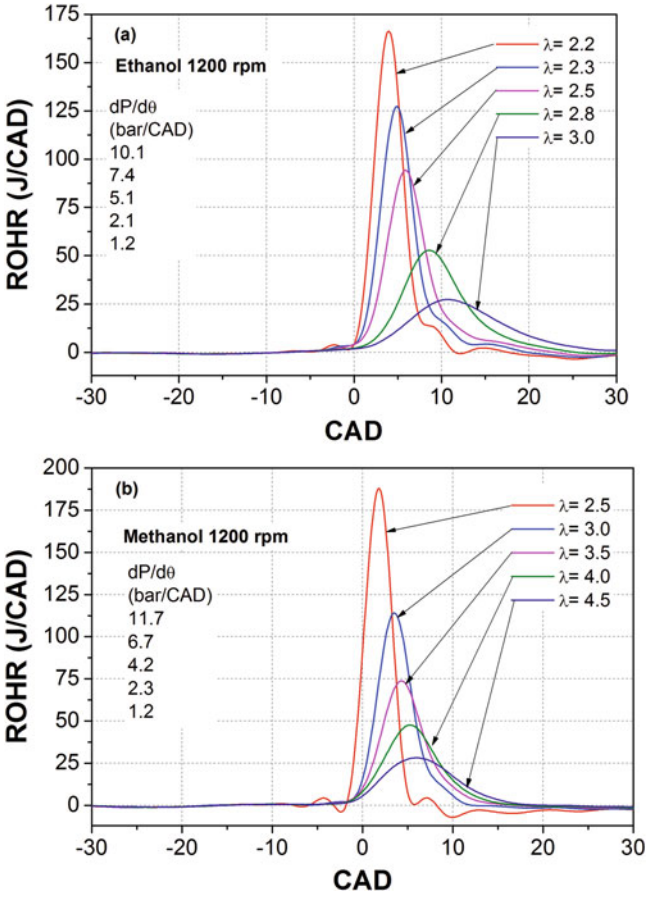

Fig. 7.22 Typical heat release rate trances for (**a**) ethanol and (**b**) methanol in HCCI combustion for different λ at 1200 rpm (adapted from [50])

methanol) show single-stage heat release process because these are high-octane fuels and do not show low-temperature heat release in naturally aspirated engine operation [1]. The highest heat release rate is achieved at richest (lowest λ) operating condition, and the lowest heat release rate is obtained for the leanest mixture (highest λ) at constant inlet air temperature in HCCI engine.

Figure 7.23 illustrates the typical heat release rate in a dual-fuel combustion engine with direct injection of high reactivity fuel and port injection of low reactivity fuel. Figure 7.23a depicts the heat release rate for three different conditions in dual-fuel combustion mode. The heat release rate shape of the first dual-fuel combustion mode is similar to the heat release rate shape of the conventional diesel combustion (Fig. 6.23a). However, the heat release rate shape of the second dual-fuel combustion mode looked like an "M shape," which has two maxima in the heat release rate. The third heat release rate shape of dual-fuel combustion mode 3 is similar to a "bell

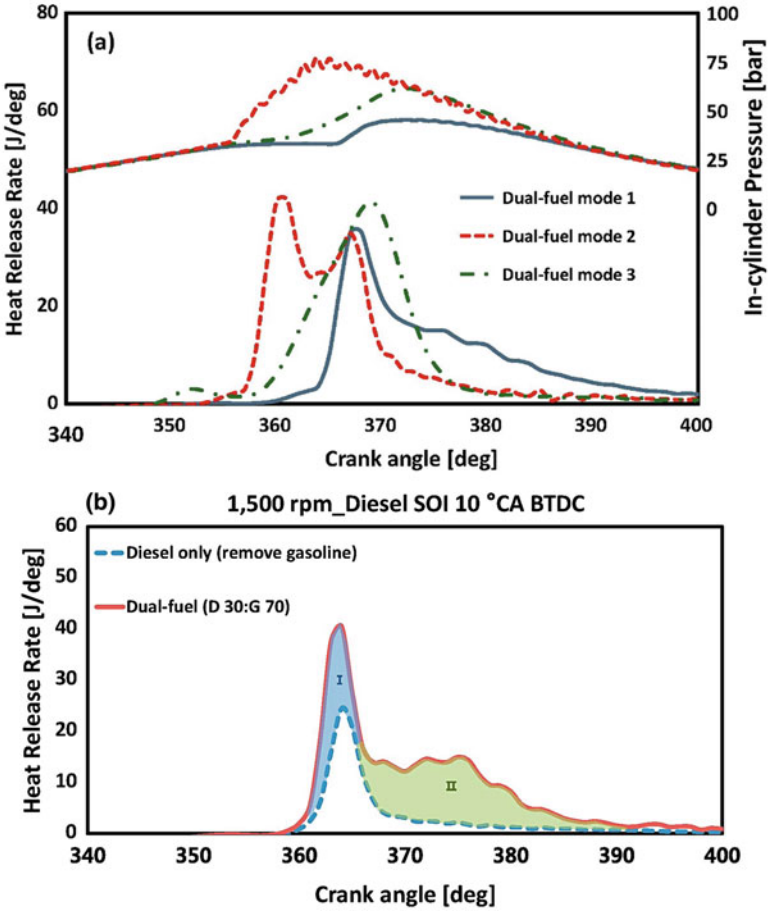

Fig. 7.23 (**a**) Heat release rate traces of dual-fuel combustion modes 1 (diesel SOI: 6°CA BTDC), 2 (diesel SOI: 13°CA BTDC), and 3 (diesel SOI: 46°CA BTDC) at 1500 rpm/Φ:0.44/gasoline ratio:70%, (**b**) comparison of dual-fuel combustion and diesel-only combustion [51]

shape" based on the premixed combustion. Figure 7.26b illustrates the difference in heat release rate when low reactivity fuel (gasoline) is added or not added at the constant diesel injection timing which was 10°CA bTDC. The shaded area (Fig. 7.23b) shows the increasing amount of heat release rate due to gasoline fuel during dual-fuel combustion. The "part I" area is originated by the combustion of gasoline (which is premixed with air where diesel is injected) as a premixed combustion phase. In "part II" area, the flame propagation of gasoline is proceeding, which was supported by the energy provided from the diesel mixing controlled and late combustion modes [51]. The gasoline fuel burned along with the burning of the diesel fuel, not after the end of diesel combustion.

7.6 Tuning of Heat Release

Cylinder pressure measurement and its analysis are routinely used for understanding the engine combustion because it provides a large amount of information such as IMEP, PMEP, peak in-cylinder pressure (critical structural constraint), combustion rate and phasing, etc. Several recent studies used cylinder pressure signal for online combustion diagnostics and control, trapped mass estimation, EGR control, emissions control, and noise control. The combustion diagnostics and control strategies require a reliable pressure data and error-free input parameters for accurate calculation of combustion parameters through heat release analysis. For better combustion diagnostics, understanding of the sensitivity of the combustion parameters to measurement error in the input parameters is required. The heat release analysis using single-zone model uses several input parameters, which can lead to error if input parameters have measurement error. Thus, tuning of the input parameters required for heat release computation is essential for the correct determination of heat release rate. In this section, tuning of input parameters based on measured motoring pressure and self-tuning methods are discussed in detail. A method for automatic identification of the heat release parameters is proposed in reference [52]. To have a well-determined reference for the heat release, the identification is performed for a motored cycle that is obtained by skipped firing. The parameters γ, crank angle offset, pressure sensor offset, and IVC cylinder pressure are identifiable without numerical difficulties. At least one of the parameters' initial temperature, wall temperature, and heat transfer coefficient, included in the heat transfer equations, must be fixed to a constant value or else the model is overparameterized. Another study proposed a method that the gross cumulative heat release should be constant following the end of combustion [3]. If the errors in the value of γ and measured pressure data are small, then any deviations from a constant heat release are due to heat transfer errors. Therefore, it is assumed that the heat transfer multiplier should be adjusted to give a cumulative gross heat release which is constant following the end of combustion. Potential problems with this method include the fact (1) that very slow burn cycles are difficult to cater for, (2) that pressure measurement errors will produce erroneous values of heat transfer rate and perhaps heat release rate, and (3) that "signal noise" effects may cause additional problems.

7.6.1 Motoring Pressure-Based Method

In this method, input parameters used for calculating heat release using a single-zone model are tuned using measured motoring pressure. The heat release calculated using cylinder pressure in motored operating condition must be zero because there is no combustion occurring during motoring operation. Figure 7.24 illustrates the measured cylinder pressure and the calculated heat release rate as a function of crank angle in motoring cycle with well-tuned parameters. The rate of heat release (ROHR)

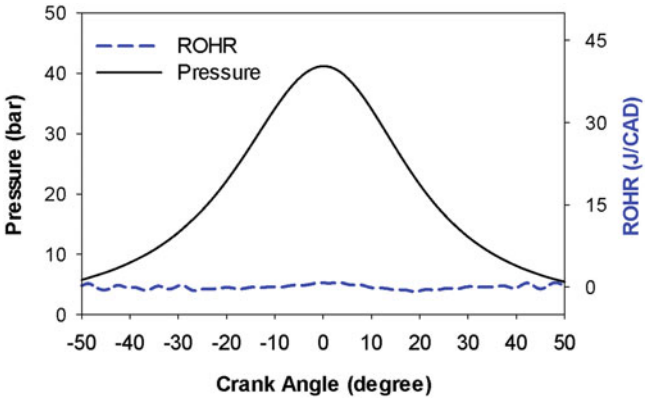

Fig. 7.24 Measured cylinder pressure and rate of heat release (ROHR) traces for motoring cycle [53]

trace is almost zero (Fig. 7.24). Thus, input parameters of gross heat release (inlet temperature and pressure, phasing between the pressure and volume trace, compression ratio and scaling factor of heat transfer coefficient) are considered to be well-tuned. Tuning of input parameter is performed iteratively with respect to calculated heat release, and the parameters giving almost zero cumulative heat release can be selected as a correct parameters.

Figure 7.25 illustrates the effect of incorrectly applied input parameters for calculation of heat release using a single-zone model. The figure shows that slight variations in some of the input parameters lead to the large and unacceptable errors in calculated cumulative heat release. Measurement errors in the phasing between pressure and volume, manifold pressure (for pegging of measured pressure signal), and compression ratio have significant error in cumulative heat release calculation.

The input parameters which provide almost zero cumulative heat release are used for calculation of heat release in the firing operating conditions. Figure 7.26 shows the measured cylinder pressure and calculated heat release rate using input parameters tuned in motoring conditions for an HCCI combustion. All the engine operating conditions were kept the same in the fired cycles except the amount of fuel injected (as compared to motoring cycle). The figure shows that the rate of heat release rate is almost zero at crank angle positions other than combustion duration.

The effect of measurement errors in the input parameters depends on the combustion parameter to be calculated using the measured cylinder pressure data. Table 7.1 illustrates the effect of measurement error in input parameters on the calculation of various combustion parameters in the HCCI engine. The calculation of errors is conducted over a wide range of load and speed conditions and summarized in Table 7.1. Table depicts that the maximum heat release rate is mainly affected by measurement errors in TDC location, compression ratio, and intake air pressure. The location corresponding to peak heat release rate is mainly affected by an error in TDC location and intake pressure. The combustion phasing (CA_{50}) is found to be a

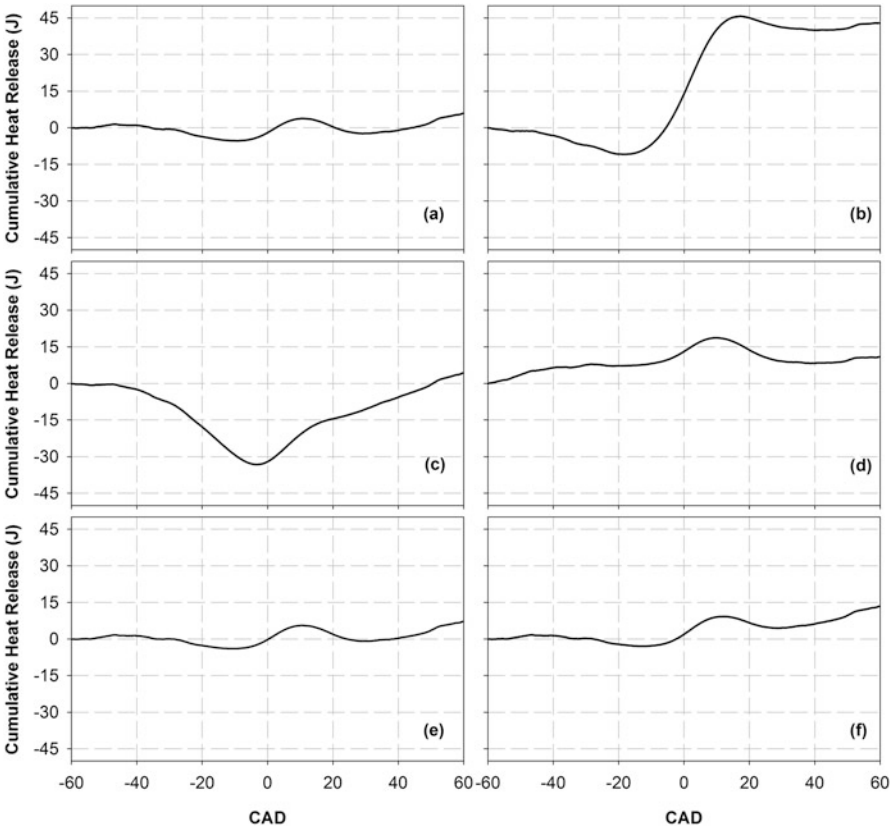

Fig. 7.25 Effect of incorrectly tuned input parameters on cumulative heat release during motoring (**a**) well-tuned parameters, (**b**) wrong phasing [*P* and *V* traces are phased apart by 1° CA], (**c**) wrong compression ratio [compression ratio is altered from 17 to 18], (**d**) wrong inlet air pressure [inlet air pressure altered from 0.99 to 0.89 bar], (**e**) wrong inlet air temperature [temperature is altered from 120 to 130 °C], and (**f**) wrong scaling of heat transfer coefficient [heat transfer increased 15%] [53]

very robust parameter for HCCI combustion control because it is mainly affected by measurement errors in TDC location. Cumulative heat release is strongly affected by measurement errors in TDC position, intake air pressure, and heat transfer determination. Calculation of maximum average gas temperature is affected mainly by measurement error in intake air pressure. The IMEP is mainly affected by phasing error of cylinder pressure and volume, and error of 1° CA leads to errors of up to 11.66%.

This method depends on the tuning parameters corrected in the motoring conditions. Thus, measurement of pressure data needs to be taken in similar operating conditions, which may be difficult in some of the engine test rigs. The other limitation is that some of heat transfer model may differ in motoring and firing conditions, and tuning parameters in motoring condition may give erroneous results

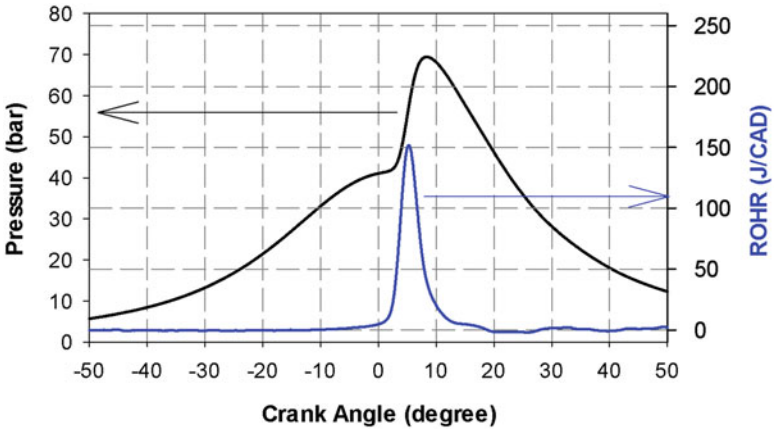

Fig. 7.26 Measured cylinder pressure and rate of heat release (ROHR) traces for a firing cycle in well-tuned parameters condition in HCCI engine [53]

Table 7.1 Effect measurement errors on HCCI engine combustion and performance parameters [53]

	IMEP (%)	PMEP (%)	HRR_{max} (%)	CA_{50} (CAD)	CD (CAD)	CAD HRR_{max}	Total HR (%)	T_{max} (%)
TDC +1 (CAD) ↑	8.87–11.66↑	1.23–0.8↑	4.58–7.80↑	1.0–0.5↑	0.167–0.5↑	1.166↑	9.88–10.81 ↑	3.21–3.94↑
r_c +1↑	NE	NE	6.90–3.36 ↓	0.33–1.0↑	5.16–4.67↑	–	0.99–1.10 ↓	4.51–3.45↓
IP −0.1 (bar) ↓	–	0.02↓	4.48–3.24↑	0.16–0.33↓	0.50–1.16↓	0.166↑	3.87–2.53 ↑	10.68↑
IT +10 °C↑	NE	NE	1.02–0.78↑	–	0.333↓	–	0.63–0.67↑	2.54↑
HT+15% ↑	NE	NE	0.16–0.41↑	–	0.5–0.66↑	–	2.17–2.52↑	–

NE no effect, r_c compression ratio, *IT* intake temperature, *IP* intake pressure, *HT* heat transfer, *TDC* top dead center, *HR* heat release, *CD* combustion duration, *PMEP* pumping mean effective pressure

(see Fig. 7.13). Additionally, this method is difficult to use online. The self-tuning method considers the heat transfer in a more sophisticated way, which may provide better results, and it can be used online.

7.6.2 Self-Tuning Method

Tunestal proposed an alternative method for self-tuning of the heat release using in-cylinder pressure [54]. This method is based on the least-square determination of

the polytropic exponent immediately before and after the combustion event, respectively. The polytropic exponent cannot be estimated during the combustion event because it is not a polytropic process. A linear interpolation of the polytropic exponent with respect to crank angle is implemented during the combustion event between the compression and expansion values. This interpolated exponent values are used for computing the heat release. The interpolated exponents automatically incorporate an aggregate model for the heat losses, crevice losses, and blowby [54]. The interpolated polytropic exponent (n) trace is used as a replacement for the ratio of specific heat (γ) in the net heat release Eq. (7.56), which is derived using definition of specific heat ratio. The resultant heat release equation can be written as Eq. (7.59).

$$\frac{dQ_n}{d\theta} = \frac{n}{n-1} P \cdot \frac{dV}{d\theta} + \frac{1}{n-1} \frac{dP}{d\theta} \cdot V \tag{7.59}$$

The crank angle intervals used for least-square fit to estimate polytropic exponent before and after combustion need to be selected based on the beforehand knowledge of the earliest and latest possible occurrence of combustion event, respectively. There is also a trade-off in choosing the interval lengths because a longer interval leads to improvement in statistics for the polytropic exponent estimation but also means more variation of the polytropic exponent over the interval [54]. Figure 7.27 illustrates the variations of polytropic exponents estimated before (compression) and

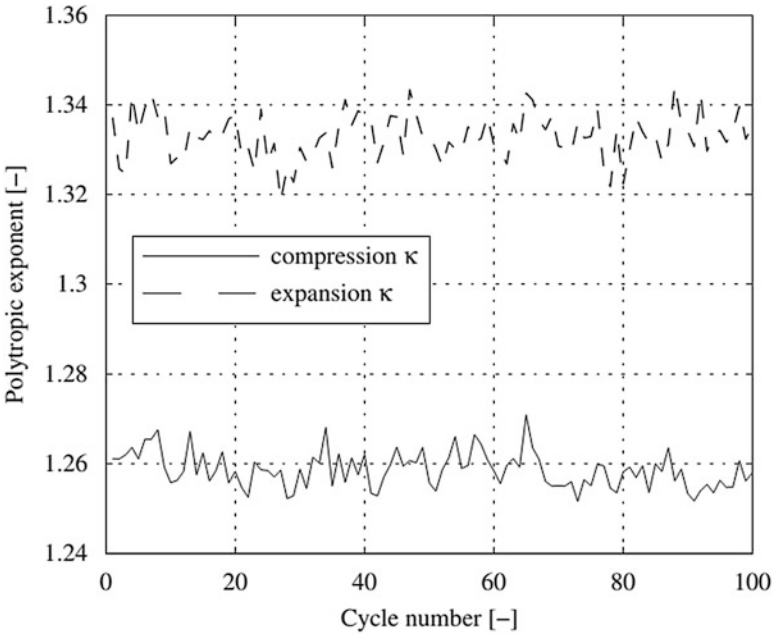

Fig. 7.27 Variations of polytropic exponents estimated before and after HCCI combustion ($\lambda = 2.5$) for 100 consecutive cycles [54]

after (expansion) HCCI combustion ($\lambda = 2.5$) for 100 consecutive cycles. The interpolated exponent between these two values is used during combustion process in Eq. (7.59).

The algorithm was proved to be fast and suitable for online calculation of the combustion phasing because in this model, there is no need to tune the heat transfer which allows a faster post-processing. The weak point of this model might be represented by the linear interpolation between the polytropic exponent before and after the combustion. A validation study of self-tuning heat release algorithm demonstrated that there is a very good match between the rate of heat release and the heat release computed with the modified Tunestal model and the Woschni model [55]. Additionally, the self-tuning heat release algorithm is user-independent which means that there are no errors introduced by the user; this allows a more realistic comparison between different engines and different operating points.

7.7 Estimation of Various Combustion Parameters

Combustion diagnosis and control have always been important in engine management systems. Presently, it is even more crucial due to the increasing demands to reduce pollutant emissions and engine noise. For this reason, a large number of parameters need to be evaluated in modern engine control systems. Engine combustion diagnosis and/or monitoring for closed-loop control has been implemented using the ion current sensor, optical combustion timing sensor, and cylinder pressure sensors. However, for combustion control in reciprocating engines, the in-cylinder pressure sensor is most widely used because ion current and optical sensors do not guarantee endurance during soot contamination (typically in a diesel engine). For combustion monitoring or diagnosis by cylinder pressure measurement, estimation of combustion indicators is required. Several combustion parameters such as start of combustion (SOC), ignition delay, the location of 50% fuel mass burned, combustion duration, etc. are estimated to obtain different kinds of information about the combustion process and combustion modes. This section describes different methods for evaluation of various combustion parameters in reciprocating engines using in-cylinder pressure measurement.

7.7.1 Start of Combustion

The start of combustion (SOC) is an important indicator due to its direct impact on heat release rate, which affects the pollutant formation and combustion noise. Thus, SOC directly affects the combustion as well as emission, and engine performance (torque and efficiency) typically increases with advanced SOC. The advanced SOC timings also lead to higher peak pressure and temperature in the cylinder, which increases the NOx emissions, and very advanced SOC may also hamper the engine efficiency. On the other hand, retarded combustion timing can result into incomplete

combustion leading higher unburned hydrocarbons. Therefore, optimal SOC position is essential at particular engine operating condition and combustion mode [56, 57]. Typically, SOC is controlled by spark (in gasoline engines) or injection (in diesel engines) timings, but ignition delay can vary during the lifetime of the engine because of variation in fuel quality or gradual deterioration of the engine and injection/spark system. Additionally, combustion in advanced premixed compression ignition engine is kinetically controlled, and ignition timing is governed by pressure and temperature in the cylinder. Thus, closed-loop control of SOC is required to correct unanticipated shifts in SOC timings. The requirements of the pressure variable for engine control are (1) one-to-one correspondence to engine operating conditions, (2) invariance of the target value (mapping of combustion control is not required for constant pressure variable), (3) good signal noise immunity, (4) high contrast-noise ratio (CNR), and (5) low processor load (computational effort) [58]. Moreover, early detection of multiple SOCs created by multiple fuel injections is beneficial for not only next-cycle but also same-cycle combustion phase control [57, 59].

For online (real-time) applications, the SOC estimation methods typically use the cylinder pressure signal and its derivatives as well as the heat release rate (HRR), such as (1) the crank angle position of abrupt deviation from motoring (without combustion) pressure by measured pressure signal during combustion [58, 60, 61], (2) the crank angle position of the first maximum value of the second derivative of combustion pressure [62], (3) the crank angle position of the zero crossing (inflection point) of the second derivative of cylinder pressure during combustion [63], (4) the crank angle position of the first maximum value of the third derivative of cylinder pressure [64], (5) the crank angle position of the minimum value of the heat release rate before it starts increasing, (6) the crank angle position of the first zero crossing of the heat release rate after fuel injection [48], and (7) the crank angle position of the x % mass fraction burned ($x = 1\%$, 5%, or 10%) [60, 65]. Typically, for estimation for rapid combustion period, the crank angle position corresponding to 10% heat release (CA_{10}) is considered as SOC.

Figure 7.28 illustrates the different methods of start of combustion detection based on measured cylinder pressure data and its analysis. The SOC is typically characterized as the separation point between the measured cylinder pressure during combustion and motored cylinder pressure trace (SOC_{SP}). This is the most direct method of SOC detection. The SOC can also be defined by the location of the point where compression curves start deviating from straight line in $\log P - \log V$ curve (Fig. 6.1).

To find the deviation of measured cylinder pressure from motoring curve (sharp pressure rise is expected at the SOC), pressure derivatives with respect to crank angle are used. The inflection point can be computed where the second derivative of pressure has the value zero. This point can also be considered as SOC position. Some of the studies have used crank angle corresponding to the maximum value of the second derivative of cylinder pressure as SOC. Further research on detection of SOC showed that the maximum value of the third derivative measured cylinder pressure curve with respect to crank angle is closer to the actual SOC [64]. The

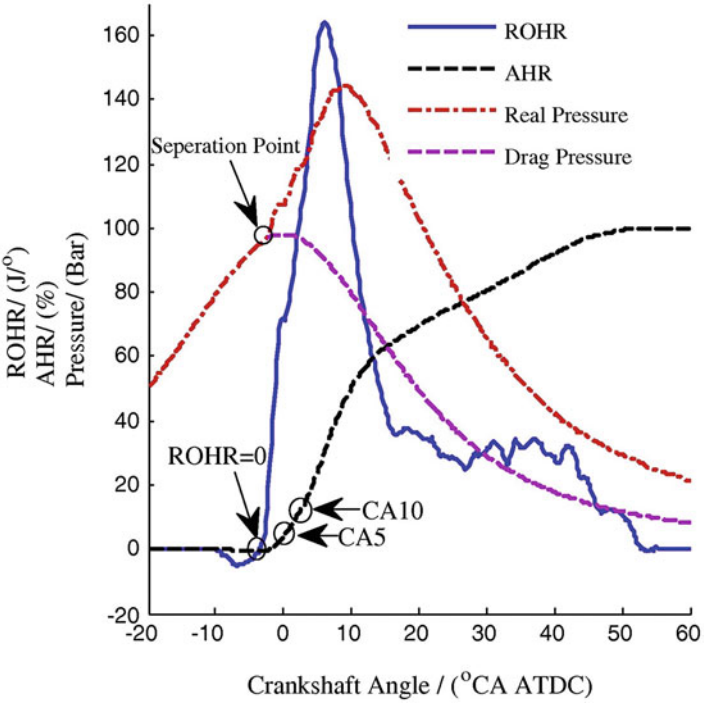

Fig. 7.28 Various start of combustion detection methods using cylinder pressure measurement [59]

physical meaning of the third derivative can be determined from the net heat release Eq. (7.56). From Eq. (7.56), it can be derived that near TDC or at TDC position (rate of change of volume is close to zero), the heat release rate can be written as Eq. (7.60).

$$\frac{dQ_n}{d\theta} \propto \frac{dP}{d\theta} \tag{7.60}$$

The Eq. (7.60) suggests that the peak heat release rate will coincide with the peak pressure rise rate. To define SOC, it is appropriate to denote the point where heat release rate significantly departs from zero (the point of maximum curvature of heat release rate) as the position of SOC. Mathematically, the maximum of second-order derivative of heat release rate can be designated as SOC position. Using Eq. (7.60), the maximum of the second derivative of pressure rise rate can be used as SOC.

$$\text{SOC} = \left(\frac{d^3P}{d\theta^3}\right)_{\max} \tag{7.61}$$

Since the cylinder pressure signal naturally contains electric noises, the accuracy of differential operations is very low, and it can lead to inaccurate results for real-

time control systems [59, 60]. A threshold value of the third derivative of pressure is also used to calculate SOC as shown by Eq. (7.62) [66].

$$\frac{d^3P}{d\theta^3} > \left.\frac{d^3P}{d\theta^3}\right|_{\text{lim}} \tag{7.62}$$

The threshold value used is 25 kPa/CA^3 for the detection of the main SOC in HCCI engine [66].

Heat release-based methods are also used for the detection of ignition timing or SOC in reciprocating engines. Typically, the SOC position is defined as the zero-crossing point of heat release rate (HRR) curve ($SOC_{HRR=0}$) [59]. The HRR is usually below zero before combustion due to vaporization of fuel in the cylinder. Thus, the first point when the HRR curve reached to zero value is considered as SOC. The calculation of HRR involves cylinder pressure derivative, and thus, numerical derivative operation on real-time system can be problematic due to electrical noise. Filtering operation can be performed on raw data to minimize the effect of noise, but it increases the computation time. Generally, CA5 or CA10 (5% and 10% heat release position, respectively) is used as SOC to obtain reliable results for control purposes. Ignition position is important in HCCI combustion as there is no direct control on ignition timings. However, accurate ignition timing detection is required for combustion diagnosis particularly in fully premixed combustion (HCCI) or partially premixed combustion (PPC). To determine the ignition timing in HCCI engine, a study used one crank angle before the 1% heat release position [67]. Sometimes crank angle position corresponding to 1% heat release is also used as ignition position.

Figure 7.29 illustrates the typical heat release rate trace for partially premixed combustion (PPC). The HRR curve can be divided into four distinct phases: (1) ignition delay (ID), (2) low-temperature reaction (LTR), (3) premixed combustion phase, and (4) late mixing controlled phase (Fig. 7.29). In this combustion, typically fuel injection ends before the SOC. Ignition delay (ID) phase is defined as the period between start of injection (SOI) and SOC. The duration between the end of injection (EOI) and SOC is denoted as mixing period (MP). The SOC is defined as the position at which HRR is zero (CA0). The HRR is negative in ID phase because most of the fuel is injected in this period and evaporation of droplets occurs. The LTR phase occurs as a small peak before the main heat release (Fig. 7.29). To determine the start of the main heat release position, the end of LTR (EoLTR) is defined. A Gaussian profile is used to distinguish the LTR and main heat release in a well-defined manner [68, 69]. Gaussian profile is fitted to the rising flank of the premixed peak, between the end of LTR and the actual peak, and the difference between the fitted curve and HRR curve is calculated. The position where the difference is zero is considered as EoLTR.

Another study used a threshold value of 0.2 J/CAD of HRR for estimation of ignition timing as well as ignition pressure and temperature in HCCI engine [70]. The conventional heat release method requires large computational effort in

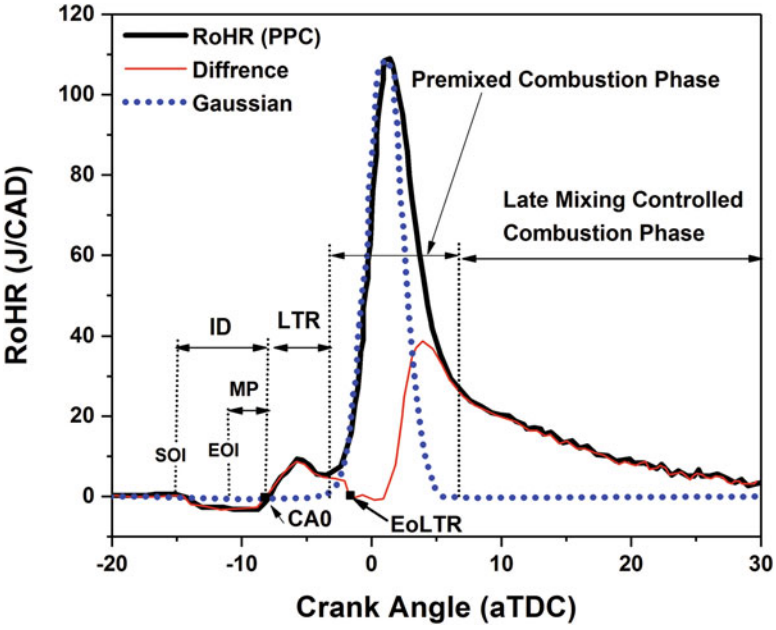

Fig. 7.29 Typical HRR curve indicating different combustion phasing in PPC engine (adapted from [68], Courtesy of Hadeel Solaka)

the calculation of heat release. Therefore, computationally efficient methods of SOC detection are proposed based on initial heat release [56].

The initial heat release (IHR) can be calculated from the heat release rate Eq. (7.56). The measured cylinder pressure is expressed as a summation of pressure difference due to combustion and motoring pressure ($P = P_{\text{diff}} + P_{\text{motoring}}$). The Eq. (7.56) can be written as Eq. (7.63) by substituting the pressure values [56].

$$\frac{dQ}{d\theta} = \frac{1}{\gamma - 1}\left(V\frac{dP_{\text{diff}}}{d\theta} + \gamma P_{\text{diff}}\frac{dV}{d\theta}\right) + \frac{1}{\gamma - 1}\left(V\frac{dP_{\text{motoring}}}{d\theta} + \gamma P_{\text{motoring}}\frac{dV}{d\theta}\right) \quad (7.63)$$

Typical variations of each term in Eq. (7.63) are presented in Fig. 7.30a. It can be noticed from Fig. 7.30a that the term (b) is zero near the early stage of combustion. Thus, it can be neglected from the Eq. (7.63). Thus, the initial heat release rate (IHRR) equation can be written as Eq. (7.64) [56].

$$\frac{dQ}{d\theta} \approx \frac{1}{\gamma - 1}\left(V\frac{dP}{d\theta} + \gamma P_{\text{motoring}}\frac{dV}{d\theta}\right) \quad (7.64)$$

The cumulative initial heat release (IHR) can be calculated from the Eq. (7.64) by integrating the equation. The variation of total heat release (HR) calculated using Eq. (7.56) and IHR calculated using Eq. (7.64) is shown in Fig. 6.30b.

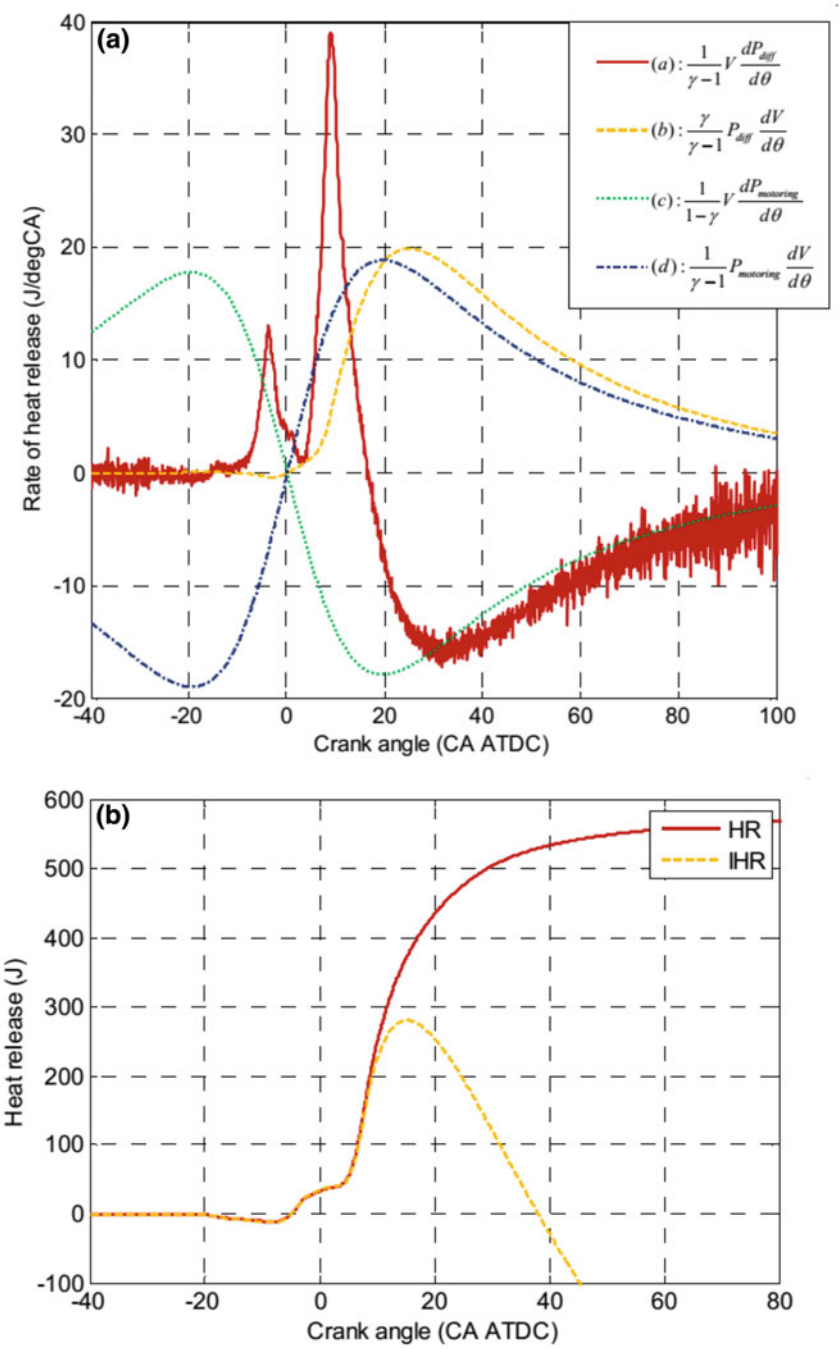

Fig. 7.30 (**a**) Variations of different terms in Eq. (7.63) and (**b**) total heat release and initial heat release variation [56]

The estimated SOC combustion is defined as a linear interpolation of 2% of IHR (IHR_2) as shown in Eq. (7.65).

$$SOC_{est} = a \times IHR_2 + b \tag{7.65}$$

This method can also be used for online estimation of SOC. It is demonstrated that this method reduces 49.8% of the cylinder pressure acquisitions and 44.8% of the calculation time compared to the conventional method [56]. However, this method still uses the pressure derivative, which is sensitive to electrical noise.

The difference between the measured cylinder pressure and the motoring pressure is also used for determination of SOC. The SOC estimated using this method is highly dependent on the accuracy of the determination of motoring pressure. The separating position of motoring and fired pressure is typically detected with a threshold, i.e., the crank angle position at which the pressure difference is greater than the threshold value is considered as the initial SOC (further correction also possible) [60]. A threshold of 10 bar is used in reference [58, 61], and 1.5 bar is used in [59]. However, these threshold values are too high for the detection of the start of low-temperature reactions in premixed compression ignition engines. The motoring pressure is typically predicted by assuming the polytropic process, and the determination of polytropic index is crucial for the accurate determination of motoring pressure. A fixed polytropic index limits prediction of the accurate motoring pressure because wall heat transfer strongly affects the polytropic process. A study [59] corrected the polytropic index by mean gas temperature, and the reference point is changed at every 10 °C, and the estimation error less than 1.5 bar in the motoring pressure is demonstrated. Another study used self-adaptive correction in the polytropic index for estimation of correct polytropic index [60]. The equivalent polytropic exponent can be calculated using Eq. (7.66).

$$k_e(i) = \frac{\log p(i) - \log p(i-1)}{\log V(i-1) - \log V(i)} \tag{7.66}$$

The $p(i)$ can be the same as or lower than $p(i-1)$ because of signal noise, and thus, a fixed reference is selected to avoid nonphysical values [57] as shown in Eq. (7.67).

$$k_e(i) = \frac{\log p(i) - \log p_{ref}}{\log V_{ref} - \log V(i)} \tag{7.67}$$

At the jth point in the mth engine cycle, the real value of the equivalent isentropic index $k_e(j, m)$ is calculated using Eq. (7.67). The predicted value of the equivalent isentropic index $k_{e,p}$ of the ith point is computed by Eq. (7.68).

$$k_{e,p}(i,m) = k_e(j,m) + C(i,j,m) \quad i \in (j, j+u) \tag{7.68}$$

where u is the prediction length and $C(i, j, m)$ is a self-adaptive correction factor for the prediction of the ith point at the jth point in the mth engine cycle. This factor is corrected once in the current engine cycle by Eq. (7.69).

$$C(i,j,m) = \alpha(k_e(i,m-1) - k_e(j,m-1)) + (1-\alpha)C(i,j,m-1) \tag{7.69}$$

where α is a coefficient for this self-adaptive strategy, with a value between 0 and 1 [60].

After determining the predicted equivalent isentropic index, the motoring pressure can be determined using Eq. (7.70).

$$p_{mot}(i) = p_{ref}\left(\frac{V_{ref}}{V(i)}\right)^{k_{e,p(i)}} \tag{7.70}$$

Using this method, the motoring pressure can be determined accurately with an error less than 0.02 bar [60].

Figure 7.31 illustrates the detection of SOC using self-adaptive correction of the polytropic index. The threshold value used for detection of low-temperature reactions is 0.02 bar. The method is able to determine SOC satisfactorily, and it can be used online. It can also be noted that this method does not use the pressure derivative term.

A real-time SOC detection method applying the first derivative of the equivalent isentropic index is proposed [57]. The polytropic index is calculated using Eq. (7.67) from the measured data. The first derivative of the polytropic index is calculated using Eq. (7.71), and its result is illustrated in Fig. 7.32.

$$dk_e(i) = 100 \times (k_e(i) - k_e(i-1)) \tag{7.71}$$

The original value of the derivative is magnified in order to be calculated in the real ECU [57].

Figure 7.32 depicts that first derivative of the equivalent isentropic index increases rapidly after the SOC which indicates that it can be utilized for the detection of the SOC. Figure 7.33 illustrates the determination of SOC using this method. To achieve the accurate results, the SOC detection begins only after fuel injection and two-stage threshold levels are used. The first point whose value is over the higher threshold level is obtained, and then the next point whose value is over the lower threshold level is obtained and treated as the detected SOC [57]. This method is capable of detecting multiple SOCs caused by multiple injections, and it can be used for engine operation in both in stationary and transient conditions.

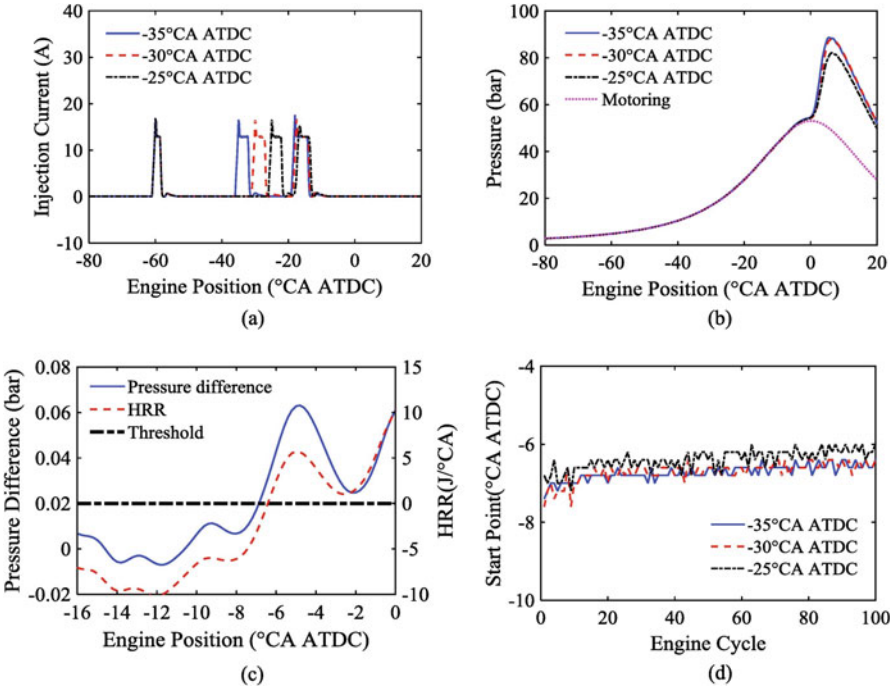

Fig. 7.31 Illustration of SOC detection method at 1200 rpm, IMEP 5.4 bar [60]. (**a**) Injection currents. (**b**) Cylinder pressure. (**c**) Pressure difference for second fuel injection timing at −25°CA ATDC. (**d**) Start of low temperature reactions

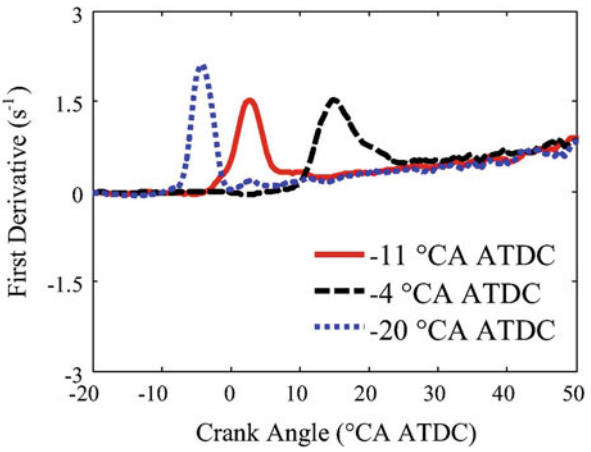

Fig. 7.32 First derivative of the equivalent isentropic index for different main fuel injection timing in a compression ignition engine [57]

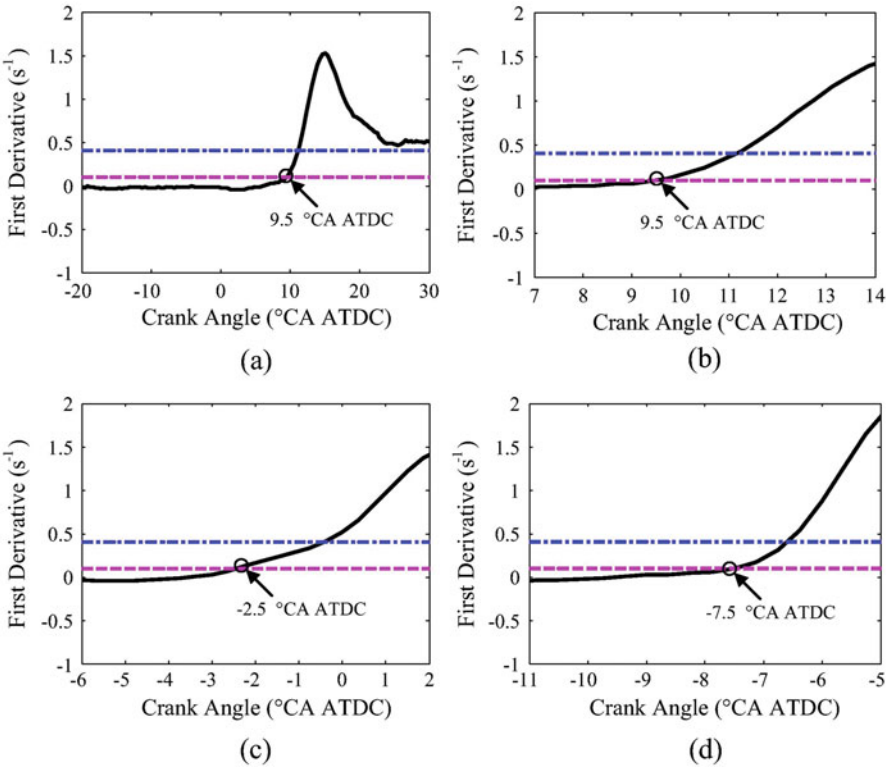

Fig. 7.33 Illustration of SOC detection method using the first derivative of isentropic index [57]. (**a**) −4°CA ATDC main fuel injection timing. (**b**) Partial view of (**a**). (**c**) −11°CA ATDC main fuel injection timing. (**d**) −20°CA ATDC main fuel injection timing

7.7.2 Ignition Delay

In a diesel engine, the ignition delay (ID) is typically defined as the duration between the SOI and the SOC. Ignition delay plays an important role in the operation and performance of diesel engines. Diesel engines tolerate a range of IDs with minimal variation in the performance. However, the ID longer than the designed value can cause significant impacts. Particularly, longer ignition delay leads to the very high-pressure rise rate which can be destructive to engine components [71, 72]. Figure 7.34 depicts the ignition delay and combustion process of typical diesel combustion. Diesel combustion can be divided into four phases (Fig. 7.34a) [73]. The fuel is injected between the start of injection (SOI) and end of injection (EOI) as diesel spray. The combustion phases can be distinguished from the heat release rate (HRR): initial jet development (physical delay and chemical delay) when the fuel starts to vaporize (SOV); triggering autoignition or start of combustion (SOC); premixed combustion; and diffusive combustion, also called mixing controlled, until end of

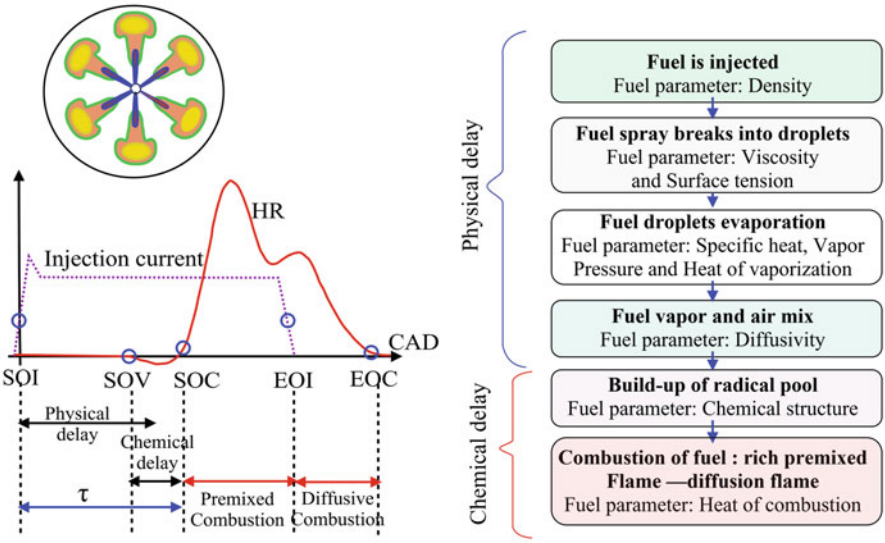

Fig. 7.34 Physical and chemical processes during ignition delay period in a diesel engine [71]

combustion (EOC). Diesel spray consists of three distinct zones: (1) spray evaporation, (2) mixing with surrounding hot air, and (3) combustion (Fig. 7.34b) [71]. Total time taken before the combustion and after the fuel injection can be divided into two major groups called physical delay and chemical delay. Physical delay comprises the time necessary for droplet breakup, air entrainment, and vaporization. Even though the fuel's physical properties such as density, specific heat, and volatility have an effect on the physical delay [74], in high-pressure injection jets, the fuel injection pressure has a deterministic impact on the spray breakup and vaporization [75]. Chemical delay is controlled by the fuel's autoignition kinetics which is dependent on fuel chemical composition, molecular structure, and associated reactivity. Thus, pressure, charge temperature and local equivalence ratio conditions affect chemical ignition delay [73, 74]. Physical delay and chemical delay usually overlap in time. For CI engines, the physical delay is much longer than chemical delay. The cylinder charge conditions at SOI affect the duration of the physical and chemical processes [73]. Higher temperature reduces both delays: the higher thermal energy entrainment for the same mass of air speeds up the vaporization [76]. In addition, the chemical kinetics are faster, and the chemical delay is shorter [77].

The ignition delay can be estimated by determination of SOI and SOC which can be determined by several methods (Sect. 7.7.2). Start of injection (SOI) can be determined from the injection current at a calibrated threshold where mass estimated by the difference between SOI and EOI, i.e., injection duration, agrees with measurements of injected mass in a spray rig. Start of vaporization (SOV) is when the absorption of energy for fuel vaporization starts to decrease the apparent HR. A good trade-off between detectability and accuracy was found when the derivative of the HR goes below -0.6 J/CAD^2 [73].

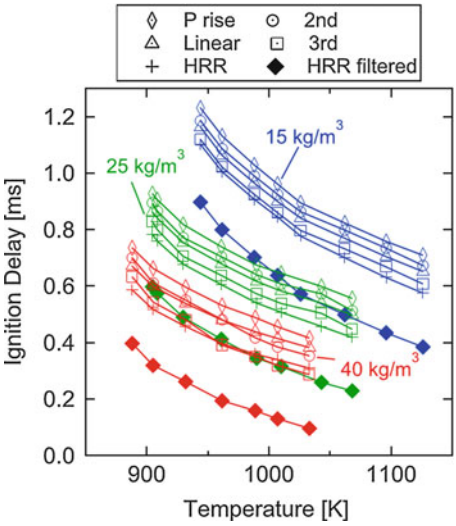

Fig. 7.35 Comparison of different ID criterion for the jet-A2 fuel data at three different SOI densities (15, 25, and 40 kg/m^3) versus temperature [72]

A study used six different criteria of SOC detection for the estimation of ignition delay [72]. The criterion uses are as follows: (1) the crank angle position of 50% of pressure rise (*P* rise) because of premixed burn combustion, (2) extrapolation of the peak slope of the pressure rise due to combustion to the zero-crossing point (denoted as linear in Fig. 7.35), (3) the crank angle position of the first peak of the second derivative of cylinder pressure (second), (4) the crank angle position of the first peak of the third derivative of cylinder pressure (third), (5) the crank angle position of 10% of the maximum HRR in the premixed burn (HRR), and (4) same as (5) except using the HRR computed from a low-pass filtered pressure data (HRR filtered).

Figure 7.35 illustrates the estimated ignition delay for three SOI densities using six different methods of SOC detection. The five methods based on the unfiltered pressure trace are grouped together, whereas, using the HRR determined from the filtered pressure gives ignition delay values that are 200–330 μs shorter than the other methods [72]. The figure shows that the criteria used for SOC detection strongly affect the ignition delay period. The use of filtering before ID estimation can lead to large shifts in the ID >200 μs and is not recommended.

7.7.3 Combustion Phasing

Combustion phasing in reciprocating engines typically means the location of combustion with respect to the piston/crankshaft position. The crank angle position corresponding to the 50% mass burned fraction is generally referred as combustion phasing. The combustion phasing typically affects the performance and emission characteristics of the engine. Too early combustion phasing leads to very high-

pressure rise rate and combustion temperature, leading to high heat loss and also a loss in efficiency. Too retarded (delayed) combustion phasing may lead to incomplete combustion and higher unburned emissions. The delayed combustion phasing also leads to lower effective expansion ratio leading to a loss in engine efficiency. Therefore, engine operation at correct combustion phasing is required for optimal fuel economy. In premixed combustion where ignition is kinetically controlled, the closed-loop control of combustion phasing is essential.

Typically, combustion phasing is calculated by heat release analysis or mass burned fraction analysis. The crank angle position corresponding to 50% heat release can be computed using Eqs. (7.55) or (7.56). Sometimes other variables are also used as combustion phase like CA1 and CA5 (the crank angles corresponding 1% and 5%, burned mass fraction, respectively) which can be calculated using heat release analysis. The CA1 and CA5 are very sensitive parameters as they are easily affected by noise and other disturbances due to their small amounts of BMF. On the other hand, CA50 is more robust against noise or disturbances because the combustion has developed sufficiently at this point [78].

Combustion phasing estimation using heat release Eq. (7.55) takes a lot of computational time and, thus, not suitable for real-time applications. To reduce the computational time, the difference pressure apparent heat release equation is developed [61]. In this method, the total pressure is considered as summation of motoring pressure and difference pressure (P_{diff}) due to combustion, and heat release equation can be written as Eq. (7.63). Theoretically, there is no heat released during the motoring operation; therefore, the heat released contribution term by the motoring pressure term can be negligible in Eq. (7.63). The terms that remained after neglecting the motoring pressure terms are defined as the difference pressure apparent heat release equation, (Q_{diff}), which can be written as Eq. (7.72) [61].

$$Q_{\text{diff}} = \frac{1}{\gamma - 1} \int V \frac{dP_{\text{diff}}}{d\theta} d\theta + \frac{\gamma}{\gamma - 1} \int P_{\text{diff}} \frac{dV}{d\theta} d\theta \tag{7.72}$$

The crank angle position of 50% of the difference pressure apparent heat release ($\text{MFB50}_{\text{diff}}$) can be calculated similar to conventional combustion phase detection algorithm using heat release analysis. Fig. 7.36 illustrates the calculation method of $\text{MFB50}_{\text{diff}}$ using different heat release. The $\text{MFB50}_{\text{diff}}$ is used to determine the combustion phase parameter using a linear fitting method [61].

Another study proposed a method of combustion phase parameter as a substitute for MFB50 for real-time application based on initial heat release (IHR) [79]. In this method, the Eq. (7.72) is further simplified by assuming volume change rate negligible near the TDC position. Thus, the heat release equation can be written as Eq. (7.73).

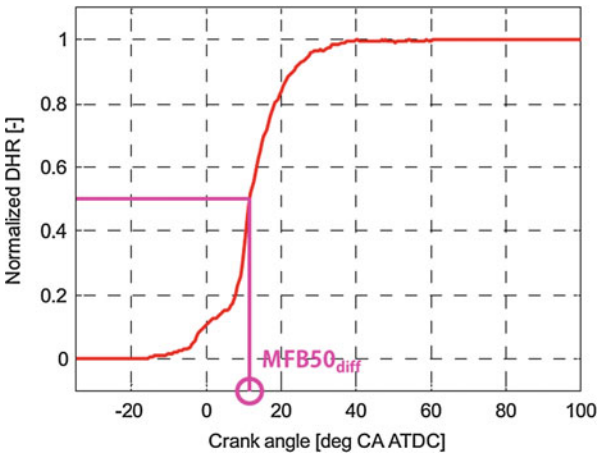

Fig. 7.36 Illustration of $MFB50_{diff}$ calculation method [61]

$$\frac{dQ}{d\theta} \approx \frac{1}{\gamma - 1} V \frac{dP_{\text{diff}}}{d\theta} \tag{7.73}$$

The initial heat release (Fig. 7.30b) is divided into IHR before peak (IHR_{bp}) and IHR after peak (IHR_{ap}) and compared with the conventional heat release. It was found that the location of 20% of IHR_{ap}, (IHR_{ap20}), has a very good correlation with MFB50 [79]. The mass fraction burned (MFB) can be estimated using Eq. (7.74).

$$\text{MFB50}_{\text{estimated}} = a \times \text{IHR}_{\text{ap20}}{}^3 + b \times \text{IHR}_{\text{ap20}}{}^2 + c \times \text{IHR}_{\text{ap20}} + d \tag{7.74}$$

Based on the analysis results, the IHR_{ap20} found to be a viable real-time combustion phase indicator [79].

A method based on the normalized difference pressure (NDP) is also proposed for the estimation of combustion phasing in HCCI engine [78]. The difference pressure (DP) is calculated by subtracting the motoring pressure from the measured pressure. The normalized difference pressure can be calculated by Eq. (7.75).

$$\text{NDP} = \frac{\text{DP}}{\max(\text{DP})} \tag{7.75}$$

Figure 7.37 shows the comparison between normalized heat release and NDP in an HCCI engine. The figure depicts that both curves follow closely during combustion. The combustion phasing parameter $CA_{NDP0.5}$ is defined as the crank angle position at which the NDP becomes 0.5. This parameter is a linear function of CA50, which is calculated by heat release. The combustion phase CA50 can be determined using Eq. (7.76) [78].

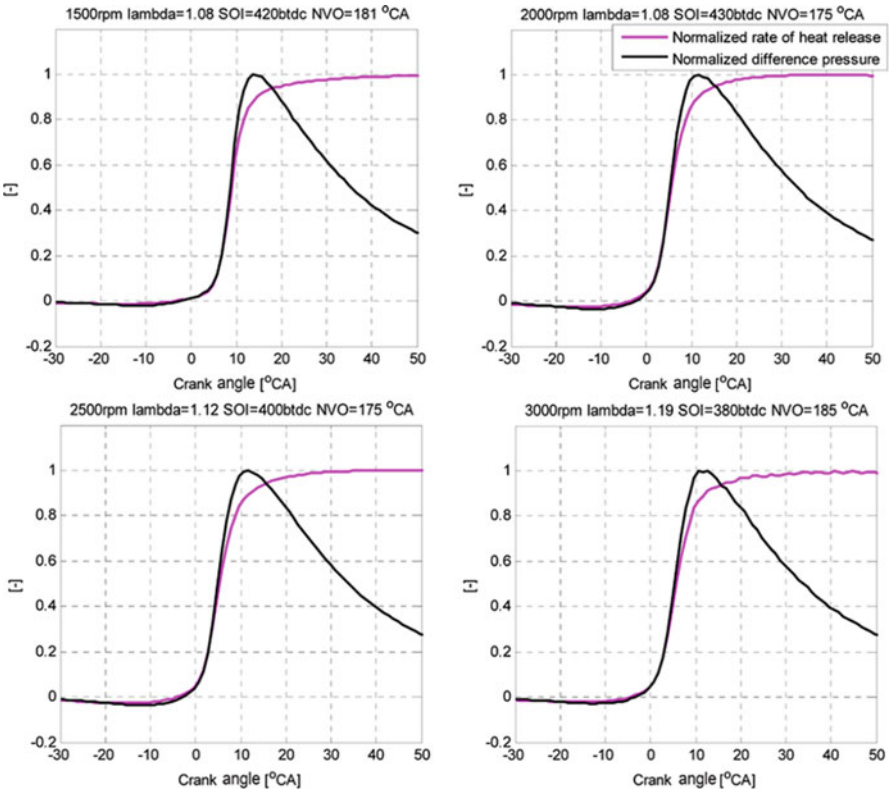

Fig. 7.37 Comparison between normalized heat release and normalized difference pressure [78]

$$\mathrm{CA}_{50\%} = \mathrm{CA}_{\mathrm{NDP0.5}} - \Delta CA_{\mathrm{DD}} \tag{7.76}$$

where $\mathrm{CA}_{\mathrm{DD}}$ is a detection delay angle, which is a constant with a typical value of around 0.3 [78]. This method is proved simpler and faster than heat release analysis and demonstrated the very good accuracy of combustion phasing detection.

7.7.4 End of Combustion and Combustion Duration

Combustion duration is an important combustion parameter, which affects the engine performance. Combustion duration is dependent on the combustion rate in the cylinder. Combustion duration is typically defined as the time period between start of combustion (SOC) and end of combustion (EOC). Section 7.7.1 discussed the various methods for the detection of SOC. The EOC can also be detected using measured cylinder pressure. When the combustion process gradually leads to burn

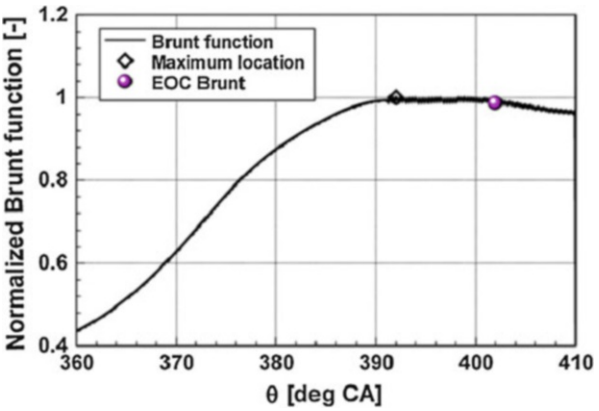

Fig. 7.38 Illustration of Brunt's methods of EOC calculation [7]

out phase, it is difficult to define suitable criteria that can adequately detect the effective EOC position [7]. Typically, the crank angle positions corresponding to 99% or 95% or sometimes 90% mass burned fraction are qualitatively used to represent EOC. A reasonably better approach is to define the ECO using $\log P - \log V$ curve (Fig. 7.1). In this curve, during expansion stroke after the end of combustion, the curve should be straight line assuming the polytropic expansion process. The inflection point (point e in Fig. 7.1) can be defined as the EOC position.

Another study [4] proposed the EOC detection by the crank angle position at which $P{\cdot}V^{1.15}$ reached a maximum value, where P is the cylinder pressure and V is the cylinder volume. The calculation of the EOC function was performed from 10° ATDC and continued to EVO-10° CA and the average value for 10° being used to minimize the noise effects [4]. The selected polytropic index (1.15) which is lower than the typical expansion index (1.25–1.3) occurs. This is done to ensure that reliable results are obtained even when large pressure errors are present and to ensure a distinct maximum to the function. The addition of 10° is to partly compensate for the low value of the index and also to ensure that combustion is complete. Figure 7.38 illustrates the EOC detection using this method. An improved method is proposed based on the analysis of the HRR [7]. This method is based on the threshold value, and a value 3% of $\mathrm{HRR_{max}}$ threshold is found suitable for the detection of EOC. The EOC is defined as the crank angle at which the heat release rate reaches to threshold value (3% of $\mathrm{HRR_{max}}$) towards the completion of combustion process. The calculation of HRR involves the pressure derivative which is sensitive to noise, and it can lead to oscillatory heat release toward the EOC. To deal with this problem, moving average of heat release is proposed for evaluation of EOC [7].

The SOC and EOC can be directly detected using $\log P - \log V$ (Fig. 7.1). The polytropic index depends on engine operating conditions and differs for engine models and from design to the other. The SOC and EOC can be determined from the ratio of specific heat (γ) variations with crank angle position [80]. An accurate $\gamma(T)$ model is a major parameter for an accurate heat release analysis because $\gamma(T)$

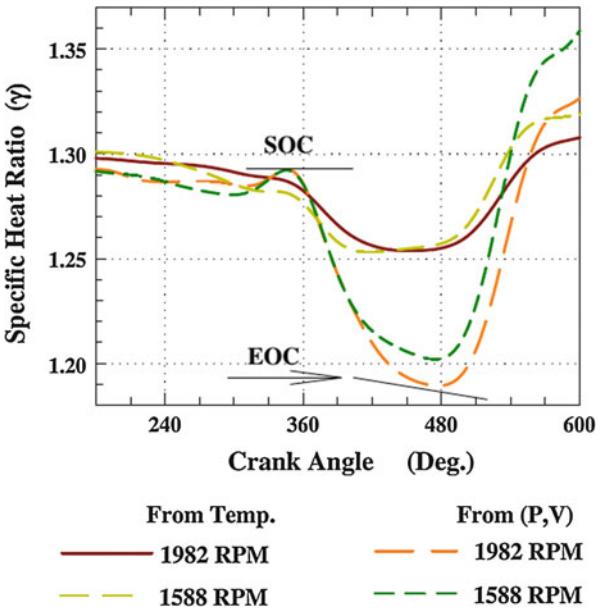

Fig. 7.39 Comparison between $\gamma(T)$ calculated from T_{Gas} and γ from (log P/log V) for gasoline at different speeds [80]

couples the system energy parameters to other thermodynamic quantities. Figure 7.39 depicts the $\gamma(T)$ calculated using two different methods (1) using temperature-dependent function and (2) using $\log(\Delta P)/\log(\Delta V)$ for two engine speeds. The $\gamma(T)$ curves have a similar trend but different numerical values. The inflection points in the $\gamma(T)$ curves are obtained based on $\log(\Delta P)/\log(\Delta V)$. The two inflection points can be considered as SOC and EOC from the Fig. 7.39.

Figure 7.40 illustrates the SOC and EOC combustion detection based on entropy determination method. The gas entropy can be calculated using a variation of gas temperature and pressure using Eq. (7.77).

$$dS = c_p \ln \frac{T}{T_r} - R \ln \frac{P}{P_r} \tag{7.77}$$

During the compression process, when charge temperature is lower than the wall temperature, the heat transfers from wall to charge occur which leads to an increase in entropy. The entropy decreases the location where charge temperature is higher than the wall temperature. Similarly, during combustion, when the HRR is higher than the heat transfer rate to the wall, entropy begins to increase, and when the heat transfer rate exceeds the combustion rate, the entropy starts to decrease toward the EOC process [80]. Therefore, the minimum or maximum entropy values achieved at SOC and EOC position, which is illustrated in Fig. 7.40. Another study also showed that the point of maximum entropy of the cylinder gases closely matched the EOC predicted by the heat release curve, while SOC did not coincide with the minimum of entropy [81]. However, the SOC can be determined from the rate of change of entropy with crank angle, which showed a rapid change at SOC point.

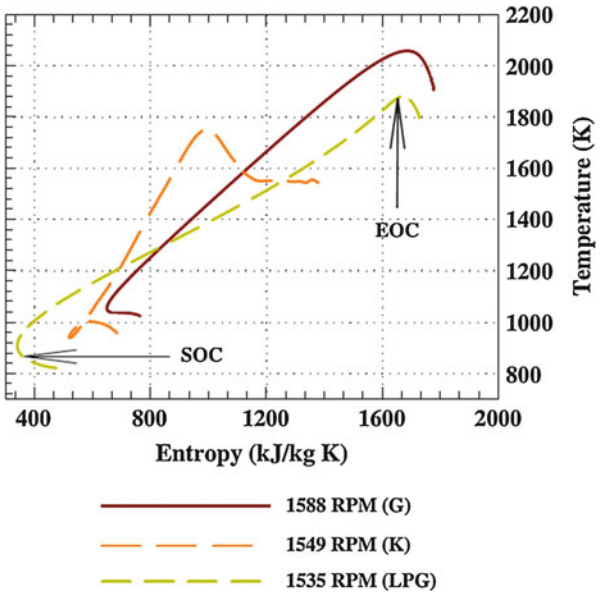

Fig. 7.40 Entropy versus gas temperature through combustion duration for gasoline at different speeds [80]

Figure 7.41 illustrates the variation of combustion duration detected using four different methods: (1) burned mass fraction, (2) entropy change, (3) $\gamma(T)$, and (4) log P − log V scale. The figure shows that combustion duration increases with engine speed irrespective of methods. The combustion duration estimated using burned mass fraction shows the smallest value, but it depends on the selected threshold value. The difference in the combustion duration predicted by other three methods is small with respect to each other [80].

A method based on the change in polytropic volume is proposed for detection of SOC and EOC [82]. The polytropic volume can be calculated using measured cylinder pressure and polytropic process assumptions during compression and expansion. The polytropic volume can be calculated by using Eq. (7.78).

$$V_{\mathrm{p,i}(\phi)} = V_{\mathrm{c}}\left(\phi_{\mathrm{ref,i}}\right)\left(\frac{p\left(\phi_{\mathrm{ref,i}}\right)}{p(\phi)}\right)^{1/n_i} \tag{7.78}$$

where V_{p} and V_{c} are the polytropic and real volume (calculated from geometry), respectively. All crank angles (ϕ) where the polytropic cylinder volume $V_{\mathrm{p,i}(\phi)}$ is not equal to the real cylinder volume $V_{\mathrm{c}(\phi)}$ do not belong to the compression process (if i = compression) or expansion process (if i = expansion) of the engine cycle [82].

Figure 7.42 illustrates the variation of real volume and polytropic volume using compression and expansion polytropic index. The crank angle location of the intake valve closes (IVC), SOC, EOC, and exhaust valve opens (EVO) can be observed clearly by the naked eye. The locations where the polytropic volume drifts away from the real cylinder volume can be detected as IVC, SOC, EOC, and EVO.

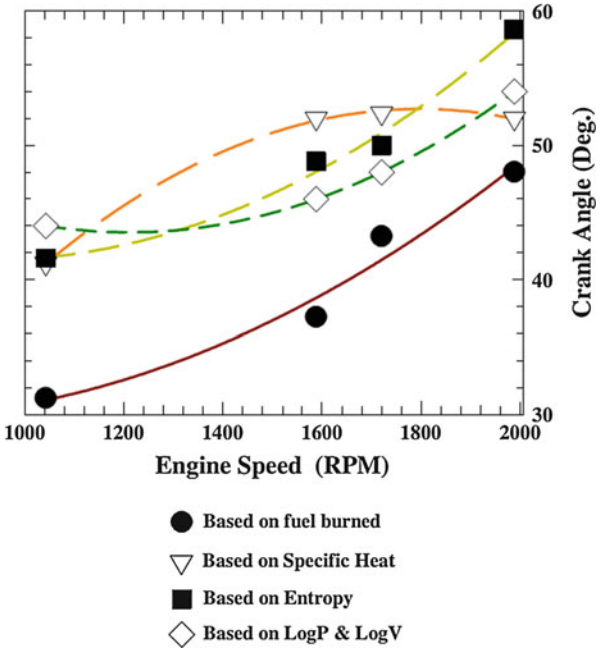

Fig. 7.41 Combustion duration using different methods using gasoline in SI engine [80]

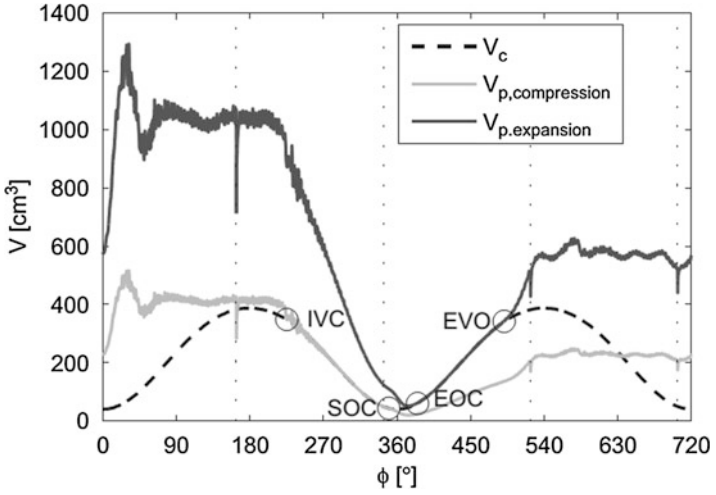

Fig. 7.42 Variation of real cylinder volume (V_c) and polytropic cylinder volumes [82]

The detection of combustion events can be performed using the simplest possible fast wavelet transformation at the first level on the change in volume ($\Delta V = V_c - V_{p,i}$) signal. The change in volume can be calculated using Eq. (7.79) with i = compression or i = expansion.

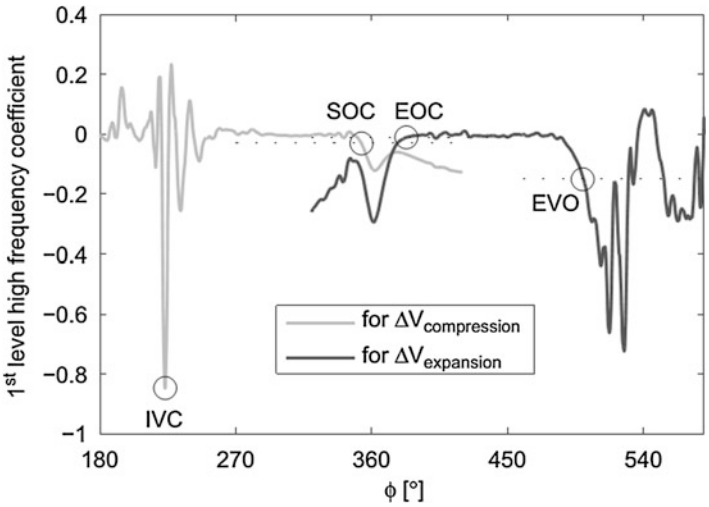

Fig. 7.43 High-frequency parts of the single-level discrete wavelet transformation for ΔV the signals [82]

$$\Delta V_{\mathrm{i}}(\phi) = V_{\mathrm{c,TDC}}\left[1 + \frac{\varepsilon - 1}{2}\left(\lambda + 1 - \cos\phi - \sqrt{R^2 - \sin^2\phi}\right)\right] - V_{\mathrm{c}}(\phi_{\mathrm{ref,i}})\left(\frac{p(\phi_{\mathrm{ref,i}})}{p(\phi)}\right)^{1/n_i} \tag{7.79}$$

Figure 7.43 illustrates the combustion event detection based on the high-frequency signals of compression and expansion using discrete wavelet transform. The combustion events can easily be detected using threshold values [82]. The detection of the first level frequency coefficient's minimum found to be a robust method for the data used because the signal is very noisy around the IVC event. The combustion events SOC and EOC can clearly be distinguished (Fig. 7.43). It is found that the SOC and EOC can be determined with less than 2% difference of the SOC or EOC based on the heat release method, and the method is robust with respect to pegging level error.

7.8 Thermal Stratification Analysis

Thermal stratification of the unburned charge before ignition plays a significant role in governing the heat release rates, particularly in HCCI engine. Understanding the conditions affecting the thermal stratification is essential for actively managing HCCI combustion rates and extending its operating range. A thermal stratification analysis (TSA) method is proposed for estimating the unburned temperature

distribution prior to ignition [83–85]. The methodology divides the cylinder charge into a number of different regions or zones, where each region has different temperature. In this method, the regions are not assigned any spatial location like it is done in multi-zone modeling. The pressure and equivalence ratio of charge is assumed to be uniform in the entire combustion chamber.

For analyzing the temperature variations before ignition, it is important to estimate an upper and lower bound on the range of temperatures which can physically exist in the combustion chamber. To describe the hottest possible unburned gas temperature (corresponds to the adiabatic core of the charge) in the cylinder, the isentropic unburned temperature is computed using Eq. (7.80) [84, 85].

$$T_{\text{isen, unburned}} = T_{\text{IVC}} \cdot \left(\frac{P_{\text{cyl}}}{P_{\text{IVC}}} \right)^{(1-1/\gamma)} \tag{7.80}$$

where P_{cyl} is the measure cylinder pressure and γ is the ratio of specific heats of the charge, which is calculated at each time step based on the mixture properties and temperature at that time step.

In an HCCI combustion engine, as the first mass burns, it compresses the remaining unburned mass, increasing its temperature and accelerating the autoignition progression. The isentropic unburned temperature (Eq. 7.80) includes the compression effect from combustion elsewhere in the cylinder by using the measured cylinder pressure. Equation (7.80) includes compression effects from compression and combustion elsewhere in the cylinder, but it does not include any heat transfer effects between zones after combustion starts. An additional term is required to capture heat transfer between the burned and unburned gases [85]. To simulate the remaining (colder) regions of the cylinder, a linear combination of the wall temperature and the isentropic unburned temperature is used and represented by Eq. (7.81).

$$T_{\text{zone}} = (1 - \text{NZT}) \cdot T_{\text{wall}} + \text{NZT} \cdot T_{\text{isen, unburned}} \tag{7.81}$$

where NZT (normalized zone temperature profile) is a scaling variable that can vary from 0 to 1. When NZT equals 0, T_{zone} represents a region with the same temperature as the wall. When NZT is 1, T_{zone} represents the adiabatic core. By varying NZT from 0 to 1, all of the possible gas temperatures can be simulated.

A given NZT represents a self-similar temperature trajectory over the compression and expansion strokes. In the absolute temperature domain, ignition depends on both time and temperature. The ignition timing of each NZT is then determined using the autoignition integral proposed by Livengood and Wu [86]. The ignition timing as a function of normalized zone temperature (NZT) is shown in Fig. 7.44 (curve 1). The mass burned fraction can also be computed from measured cylinder pressure based on heat release analysis using Eq. (7.16). The heat release can be calculated using Eq. (7.55). The mass burned fraction as a function of crank angle is shown as curve 2 in Fig. 7.44. By setting the two variables equal to each other, the assumption is made that when a pocket of gas ignites, it burns instantaneously. The mass burned faction can be obtained as a function of NZT, which is presented as

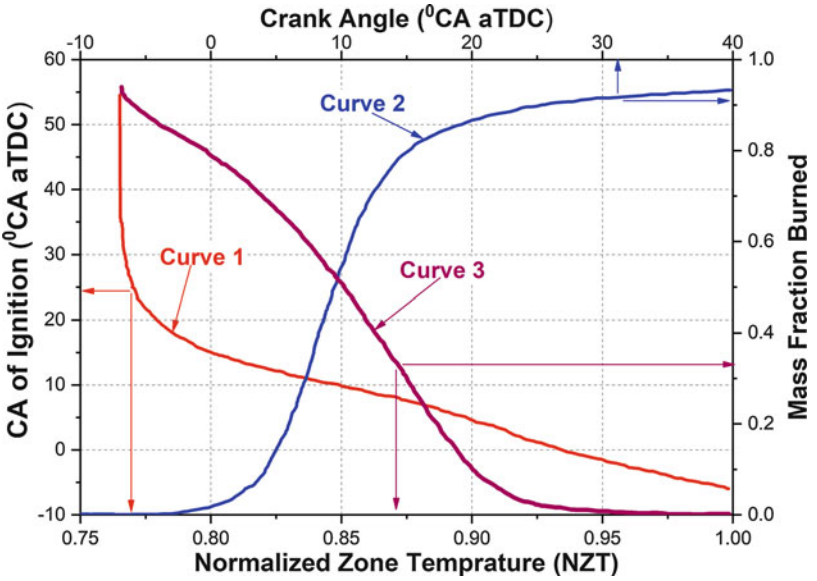

Fig. 7.44 Illustration of computation methodology of mass fraction burned as a function of NZT (adapted from [83–85])

curve 3 in Fig. 7.44. NZT relates to time and absolute temperature so that ignition timing can be plotted against one variable, instead of two. The curve 3 in Fig. 7.44 represents the distribution of mass and temperature in the cylinder, however, not in a way that is easy to visualize. Thus, the data of curve 3 in Fig. 7.44 can be rearranged in a more visually intuitive manner. The *y*-axis data in curve 3 of Fig. 7.44 is subtracted from 1, and the result is the mass cumulative distribution function (CDF) shown in Fig. 7.45.

The cumulative distribution function (CDF) is much easier to inspect the results visually. For example, the CDF in Fig. 7.45 depicts that about 90% of the mass is at a normalized temperature (NZT) of 0.90 or lower and about 20% of the mass is at NZT of 0.80 or lower. Thus, 70% of the mass is in the NZT range from 0.80 to 0.90.

The derivative of the CDF is defined as probability density function (PDF) in probability theory. The PDF of the mass burned function is calculated and presented in Fig. 7.45 (curve 2). The PDF reveals that the probability of finding mass at near-adiabatic conditions is relatively low. The highest probability of finding a mass in the cylinder occurs at a normalized temperature of about 0.88 (peak value) for this case (Fig. 7.45). As the NZT further decreases, the probability of finding mass at that temperature becomes less and less likely [85].

Chemical kinetics is ultimately sensitive to absolute temperatures. Thus, the same distributions can be plotted as a function of absolute temperature at TDC (as represented as upper *x*-axis in Fig. 7.45). Since a given NZT corresponds to an absolute temperature profile that varies with crank angle, to plot the absolute temperature distribution on a two-dimensional plot, an arbitrary crank angle needs

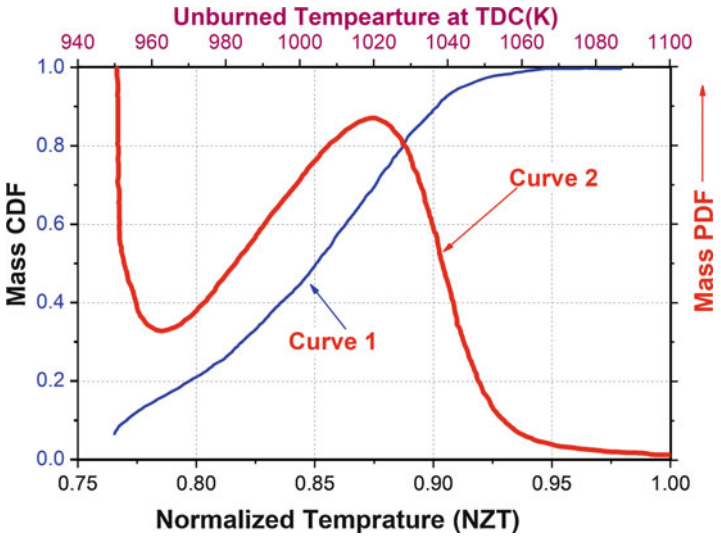

Fig. 7.45 Mass CDF and PDF with NZT and absolute temperature at TDC (adapted from [83, 85])

to be selected (TDC in this case). Then, wall temperature and isentropic unburned temperature are used to remove the normalization by Eq. (7.82).

$$\mathrm{NZT} = \frac{T_{\mathrm{zone}} - T_{\mathrm{wall}}}{T_{\mathrm{isen,\,unburned}} - T_{\mathrm{wall}}} \tag{7.82}$$

The mass PDF as a function of temperature can be used to analyze the thermal stratification in the charge. A more complete detail of thermal stratification analysis can be found in original studies [83–85].

Figure 7.46 illustrates unburned temperature distribution (as mass PDF) at the different operating conditions in an HCCI engine. The mass PDFs show the density of mass over the range of temperatures that exist in the cylinder. Higher values of the mass PDF indicate more mass concentrated at that particular temperature. Figure 7.46 reveals that the higher intake temperature or higher glow plug voltage (early combustion phasing) has broader temperature distributions with a lower peak of the distribution. The near-wall regions of all test conditions overlap because the wall conditions are not changed between the cases (Fig. 7.46). The differences in the temperature distributions for the second latest CA_{50} pair (blue) and the mid-phase CA_{50} pair (red) are negligible. However, as the glow plug voltage increases, the differences become more significant [87]. The hottest leading edge of the temperature distribution is stretched toward higher temperatures because of the glow plug's ability to heat a fraction of the mass to a much higher temperature. These results illustrate that by actively controlling the glow plug voltage, the unburned temperature distribution can be controlled to some extent, which results in some level of control over HRR in the HCCI engine.

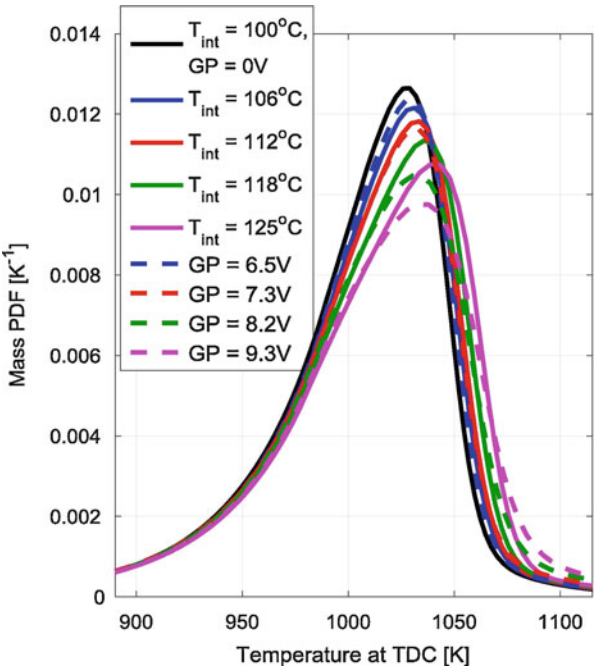

Fig. 7.46 Unburned temperature distributions for the glow plug voltage sweep and the intake temperature sweep [87]

Discussion/Investigation Questions

1. Discuss two methods for calculation of burned mass fraction (BMF) in reciprocating engines using measured in-cylinder pressure data. Describe a method that can be used for online calculation of mass burned fraction.
2. Describe the possible sources of error in the mass fraction burned calculation. Discuss why the error in mass burned fraction calculation is smaller than the error in heat release calculation.
3. Discuss the reasons why bass fraction burned calculation using Marvin's or Rassweiler and Withrow method is more suitable for conventional SI engine than diesel engines. Explain a method of mass fraction burnt calculation for a modern diesel engine.
4. Describe the experimental methods that can be used for measurement of gas temperature in the cylinder. Write the limitations of these methods and possible sources of errors in the measurement.
5. Discuss the operating conditions or combustion modes where calculated mean gas temperature using ideal gas equation is close to an actual gas temperature in the cylinder.
6. Describe a method for calculating the burned gas temperature in SI engine, and discuss the significance of the calculated burned gas temperature. Discuss its relevance over the average gas temperature calculated using single-zone model.

7. Discuss the possible reasons for spatial variations in heat flux in conventional SI and CI engines. Explain why heat flux measurement is normally conducted using the single sensor in motored condition and multiple sensors in fired operating conditions.
8. Describe various empirical models used for heat transfer coefficient in reciprocating engines. Describe why typically radiative heat transfer is not considered in SI engine but accounted in a diesel engine as it is significant. Investigate and find out the suitable heat transfer coefficient for SI, CI, and HCCI engines.
9. Discuss how fuel properties and air-fuel mixture quality affect the heat flux in the combustion chamber.
10. Investigate the effect of knocking on the heat transfer through the walls of the combustion chamber, and discuss the possible factors affecting the heat transfer.
11. Derive the heat release equation using a single-zone model, and also discretize the equation as measured pressure signal is typically digital. Discuss the assumptions made in the derivation of heat release calculation using a single-zone model. Differentiate between the net (apparent) and gross heat release rate.
12. Discuss the possible sources of error in heat release rate calculation using a single-zone heat release model. Explain the possible methods to minimize the errors in heat release calculation.
13. Figure P7.1 shows the heat release curve calculated by the single-zone model using measured cylinder pressure data from the SI engine. Heat release curves 2 and 3 have a shape different from 1 (correctly calculated) due to some error during calculation. Discuss the possible sources of error in heat release calculation in curves 2 and 3.

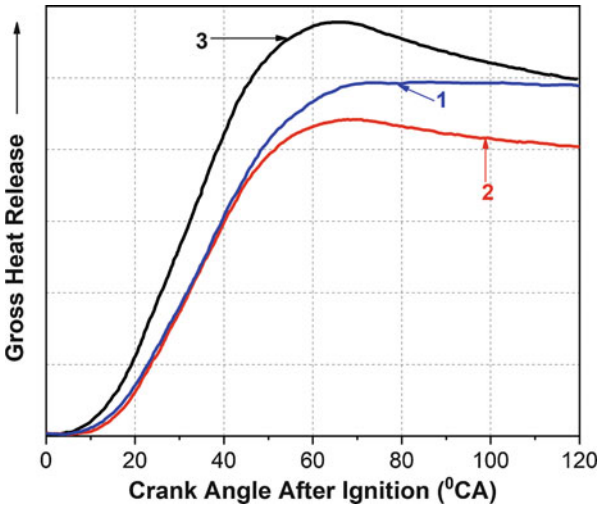

Fig. P7.1 Gross heat release as a function of crank position

14. Draw the heat release rate curves for SI, CI, and HCCI combustion engine. Discuss the difference between the heat release rate curve between conventional spark ignition and diesel combustion. How the heat release rate curve in low-temperature combustion modes such as HCCI and RCCI is different from the conventional combustion modes. Justify your answers with suitable reasoning.
15. Discuss the two methods to the tuning of gross heat release calculations. Describe the sources of error in each of the methods.
16. Discuss the combustion phase (ignition position, CA_{50}) detection algorithm for controlled autoignition (CAI) engines using in-cylinder pressure data. Why it is important to determine the combustion phasing in engine operating on LTC modes (CAI, HCCI, RCCI, etc.)?
17. Discuss the methods for detection of the start of combustion in reciprocating engines using pressure rise rate and heat release rate. Describe the merit and demerit of each of the methods.
18. Discuss the effect of SOC location on the engine combustion and performance. Explain the role of combustion duration on engine performance.
19. Explain why closed-loop control is required in modern combustion engines especially advance premixed combustion modes. Discuss the requirement that needs to be fulfilled by pressure variable that is used for closed-loop control.
20. Calculate the start of combustion, end of combustion, crank angle location for 50% burned mass fraction, and combustion duration for cylinder pressure shown in Fig. P7.2. The cylinder pressure measured at constant engine load for two different fuels (diesel and butanol blend) in a conventional four-stroke diesel engine. The bore/stroke and connecting rod length of the engine are 87.5/110 mm and 234 mm, respectively. Engine operation can be assumed at a compression ratio of 17.5. Clearly state your assumption.

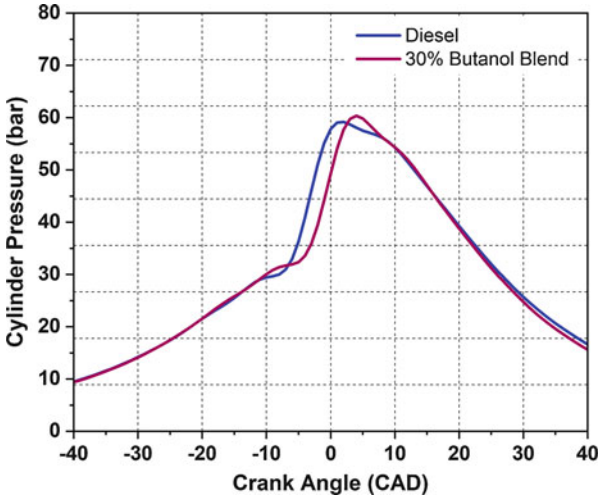

Fig. P7.2 Cylinder pressure as a function of crank angle position in a diesel engine

21. Discuss how the following parameters affect ignition delay in compression ignition engines: (1) decrease in compression ratio, (2) injection advance, (3) increase in air-fuel ratio, and (4) increase in coolant temperature.
22. Discuss the variation of ignition delay with brake mean effective pressure (BMEP) in a typical diesel engine. Draw the graph of ignition delay versus BMEP at two different cetane number (CN) fuel (e.g., CN = 60 and 40).

References

1. Maurya, R. K. (2018). *Characteristics and control of low temperature combustion engines: Employing gasoline, ethanol and methanol*. Cham: Springer.
2. Thor, M., Andersson, I., & McKelvey, T. (2009). *Parameterized diesel engine heat release modeling for combustion phasing analysis* (No. 2009-01-0368). SAE Technical Paper.
3. Brunt, M. F., Rai, H., & Emtage, A. L. (1998). *The calculation of heat release energy from engine cylinder pressure data* (No. 981052). SAE Technical Paper.
4. Brunt, M. F., & Emtage, A. L. (1997). *Evaluation of burn rate routines and analysis errors* (No. 970037). SAE Technical Paper.
5. d'Ambrosio, S., Ferrari, A., & Galleani, L. (2015). In-cylinder pressure-based direct techniques and time frequency analysis for combustion diagnostics in IC engines. *Energy Conversion and Management, 99*, 299–312.
6. Marvin Jr, C. F. (1927). *Combustion time in the engine cylinder and its effect on engine performance*. NACA Technical Report 276.
7. Baratta, M., & Misul, D. (2012). Development and assessment of a new methodology for end of combustion detection and its application to cycle resolved heat release analysis in IC engines. *Applied Energy, 98*, 174–189.
8. Rassweiler, G. M., & Withrow, L. (1938). Motion pictures of engine flames correlated with pressure cards. *SAE Transactions*, Paper no-380139, 185–204.
9. McCuiston, F. D., Jr., Lavoie, G., & Kauffman, C. W. (1977). Validation of a turbulent flame propagation model for a spark ignition engine. *SAE Transactions*, Paper No-770045, 200–223.
10. Arroyo, J., Moreno, F., Muñoz, M., & Monné, C. (2015). Experimental study of ignition timing and supercharging effects on a gasoline engine fueled with synthetic gases extracted from biogas. *Energy Conversion and Management, 97*, 196–211.
11. Matekunas, F. A. (1983). *Modes and measures of cyclic combustion variability*. SAE Technical Paper, 830337.
12. Asad, U., & Zheng, M. (2008). Fast heat release characterization of a diesel engine. *International Journal of Thermal Sciences, 47*(12), 1688–1700.
13. Vibe, I. I., & Meißner, F. (1970). *Brennverlauf und kreisprozess von verbrennungsmotoren*. Berlin: Verlag Technik.
14. Stone, C. R., & Green-Armytage, D. I. (1987). Comparison of methods for the calculation of mass fraction burnt from engine pressure—time diagrams. *Proceedings of the Institution of Mechanical Engineers, Part D: Transport Engineering, 201*(1), 61–67.
15. Eriksson, L., & Nielsen, L. (2014). *Modeling and control of engines and drivelines*. Chichester: Wiley.
16. Zhao, H., & Ladommatos, N. (2001). *Engine combustion instrumentation and diagnostics*. Warrendale, PA: Society of Automotive Engineers Warrendale.
17. Scaringe, R. J. (2009) *Extension of the high load limit in the homogenous charge compression ignition engine* (PhD thesis). Massachusetts Institute of Technology, Cambridge, MA.
18. Klein, M., & Eriksson, L. (2004). *A specific heat ratio model for single-zone heat release models* (No. 2004-01-1464). SAE Technical Paper.

19. Heider, G. (1996). *Rechenmodell zur Vorausrechnung der NO-Emission von Dieselmotoren* (Doctoral dissertation). Technische Universitaet Muenchen.
20. Heider, G., Woschni, G., & Zeilinger, K. (1998). 2-zonen Rechenmodell zur Vorausrechnung der NO-emission von Dieselmotoren. *MTZ-Motortechnische Zeitschrift, 59*(11), 770–775.
21. Kulzer, A., Lejsek, D., Kiefer, A., & Hettinger, A. (2009). *Pressure trace analysis methods to analyze combustion features and cyclic variability of different gasoline combustion concepts* (No. 2009-01-0501). SAE Technical Paper.
22. Carryer, J. E. (1992). *Estimating in-cylinder pre-combustion mixture temperatures using acoustic resonances* (PhD thesis). Stanford University, Stanford, CA.
23. Carryer, J. E., Roy, R. H., & Powell, J. D. (1996). Estimating in-cylinder precombustion mixture temperatures using acoustic resonances. *Journal of Dynamic Systems, Measurement, and Control, 118*(1), 106–112.
24. Broekaert, S., Demuynck, J., De Cuyper, T., De Paepe, M., & Verhelst, S. (2016). Heat transfer in premixed spark ignition engines part I: Identification of the factors influencing heat transfer. *Energy, 116*, 380–391.
25. Finol, C. A., & Robinson, K. (2006). Thermal modelling of modern engines: A review of empirical correlations to estimate the in-cylinder heat transfer coefficient. *Proceedings of the Institution of Mechanical Engineers, Part D: Journal of Automobile Engineering, 220*(12), 1765–1781.
26. Borman, G., & Nishiwaki, K. (1987). Internal-combustion engine heat transfer. *Progress in Energy and Combustion Science, 13*(1), 1–46.
27. Alkidas, A. C. (1980). Heat transfer characteristics of a spark-ignition engine. *Journal of Heat Transfer, 102*(2), 189–193.
28. Enomoto, Y., Furuhama, S., & Minakami, K. (1985). Heat loss to combustion chamber wall of 4-Stroke gasoline engine: 1st report, heat loss to piston and cylinder. *Bulletin of JSME, 28*(238), 647–655.
29. De Cuyper, T., Demuynck, J., Broekaert, S., De Paepe, M., & Verhelst, S. (2016). Heat transfer in premixed spark ignition engines part II: Systematic analysis of the heat transfer phenomena. *Energy, 116*, 851–860.
30. Eichelberg, G. (1939). Some new investigations on old combustion engine problems. *Engineering, 148*, 547–550.
31. Tsurushima, T., Kunishima, E., Asaumi, Y., Aoyagi, Y., & Enomoto, Y. (2002). *The effect of knock on heat loss in homogeneous charge compression ignition engines* (No. 2002-01-0108). SAE Technical Paper.
32. Lounici, M. S., Loubar, K., Balistrou, M., & Tazerout, M. (2011). Investigation on heat transfer evaluation for a more efficient two-zone combustion model in the case of natural gas SI engines. *Applied Thermal Engineering, 31*(2–3), 319–328.
33. Hohenberg, G. F. (1979). *Advanced approaches for heat transfer calculations* (No. 790825). SAE Technical Paper.
34. Woschni, G. (1967). *A universally applicable equation for the instantaneous heat transfer coefficient in the internal combustion engine* (No. 670931). SAE Technical Paper.
35. Broekaert, S., De Cuyper, T., De Paepe, M., & Verhelst, S. (2017). Evaluation of empirical heat transfer models for HCCI combustion in a CFR engine. *Applied Energy, 205*, 1141–1150.
36. Annand, W. J. D. (1963). Heat transfer in the cylinders of reciprocating internal combustion engines. *Proceedings of the Institution of Mechanical Engineers, 177*(1), 973–996.
37. Bargende M. (1990). *Ein Gleichungsansatz zur Berechnung der instationären Wandwärmeverluste im Hochdruckteil von Ottomotoren* (PhD thesis). Technische Universität Darmstadt.
38. Chang, J., Güralp, O., Filipi, Z., Assanis, D. N., Kuo, T. W., Najt, P., & Rask, R. (2004). *New heat transfer correlation for an HCCI engine derived from measurements of instantaneous surface heat flux* (No. 2004-01-2996). SAE Technical Paper.

39. Soyhan, H. S., Yasar, H., Walmsley, H., Head, B., Kalghatgi, G. T., & Sorusbay, C. (2009). Evaluation of heat transfer correlations for HCCI engine modeling. *Applied Thermal Engineering, 29*(2–3), 541–549.
40. Grandin, B., & Denbratt, I. (2002). *The effect of knock on heat transfer in SI engines* (No. 2002-01-0238). SAE Technical Paper.
41. Gingrich, E., Janecek, D., & Ghandhi, J. (2016). Experimental investigation of the impact of in-cylinder pressure oscillations on piston heat transfer. *SAE International Journal of Engines, 9*(3), 1958–1969.
42. Brunt, M. F., & Platts, K. C. (1999). *Calculation of heat release in direct injection diesel engines* (No. 1999-01-0187). SAE Technical Paper.
43. Gatowski, J. A., Balles, E. N., Chun, K. M., Nelson, F. E., Ekchian, J. A., & Heywood, J. B. (1984). *Heat release analysis of engine pressure data* (No. 841359). SAE Technical Paper.
44. Cheung, H. M., & Heywood, J. B. (1993). Evaluation of a one-zone burn-rate analysis procedure using production SI engine pressure data. *SAE Transactions*, Paper No-932749, 2292–2303.
45. Mattson, J. M., & Depcik, C. (2014). Emissions–calibrated equilibrium heat release model for direct injection compression ignition engines. *Fuel, 117*, 1096–1110.
46. Fathi, M., Saray, R. K., & Checkel, M. D. (2010). Detailed approach for apparent heat release analysis in HCCI engines. *Fuel, 89*(9), 2323–2330.
47. García, M. T., Aguilar, F. J. J. E., Lencero, T. S., & Villanueva, J. A. B. (2009). A new heat release rate (HRR) law for homogeneous charge compression ignition (HCCI) combustion mode. *Applied Thermal Engineering, 29*(17–18), 3654–3662.
48. Asad, U., & Zheng, M. (2008). *Real-time heat release analysis for model-based control of diesel combustion* (No. 2008-01-1000). SAE Technical Paper.
49. Srivastava, D. K., & Agarwal, A. K. (2014). Comparative experimental evaluation of performance, combustion and emissions of laser ignition with conventional spark plug in a compressed natural gas fuelled single cylinder engine. *Fuel, 123*, 113–122.
50. Maurya, R. K. (2012) *Performance, emissions and combustion characterization and close loop control of HCCI engine employing gasoline like fuels* (PhD thesis). Indian Institute of Technology, Kanpur, India.
51. Lee, J., Chu, S., Min, K., Kim, M., Jung, H., Kim, H., & Chi, Y. (2017). Classification of diesel and gasoline dual-fuel combustion modes by the analysis of heat release rate shapes in a compression ignition engine. *Fuel, 209*, 587–597.
52. Eriksson, L. (1998). *Requirements for and a systematic method for identifying heat-release model parameters* (No. 980626). SAE Technical Paper.
53. Maurya, R. K., & Agarwal, A. K. (2013). Investigations on the effect of measurement errors on estimated combustion and performance parameters in HCCI combustion engine. *Measurement, 46*(1), 80–88.
54. Tunestål, P. (2009). Self-tuning gross heat release computation for internal combustion engines. *Control Engineering Practice, 17*(4), 518–524.
55. Manente, V., Vressner, A., Tunestal, P., & Johansson, B. (2008). *Validation of a self tuning gross heat release algorithm* (No. 2008-01-1672). SAE Technical Paper.
56. Oh, S., Min, K., & Sunwoo, M. (2015). Real-time start of a combustion detection algorithm using initial heat release for direct injection diesel engines. *Applied Thermal Engineering, 89*, 332–345.
57. Fang, C., Ouyang, M., & Yang, F. (2017). Real-time start of combustion detection based on cylinder pressure signals for compression ignition engines. *Applied Thermal Engineering, 114*, 264–270.
58. Lee, K., Yoon, M., Son, M. H., & Sunwoo, M. (2006). Closed-loop control of start of combustion using difference pressure management. *Proceedings of the Institution of Mechanical Engineers, Part D: Journal of Automobile Engineering, 220*(11), 1615–1628.
59. Yang, F., Wang, J., Gao, G., & Ouyang, M. (2014). In-cycle diesel low temperature combustion control based on SOC detection. *Applied Energy, 136*, 77–88.

60. Fang, C., Ouyang, M., Yin, L., Tunestal, P., Yang, F., & Yang, X. (2018). Start of low temperature reactions detection based on motoring pressure prediction for partially premixed combustion. *Applied Thermal Engineering, 141*, 1101–1109.
61. Chung, J., Oh, S., Min, K., & Sunwoo, M. (2013). Real-time combustion parameter estimation algorithm for light-duty diesel engines using in-cylinder pressure measurement. *Applied Thermal Engineering, 60*(1–2), 33–43.
62. Assanis, D. N., Filipi, Z. S., Fiveland, S. B., & Syrimis, M. (2003). A predictive ignition delay correlation under steady-state and transient operation of a direct injection diesel engine. *Journal of Engineering for Gas Turbines and Power, 125*(2), 450–457.
63. Hariyanto, A., Bagiasna, K., Asharimurti, I., Wijaya, A. O., Reksowardoyo, I. K., & Arismunandar, W. (2007). *Application of wavelet analysis to determine the start of combustion of diesel engines* (No. 2007-01-3556). SAE Technical Paper.
64. Katrašnik, T., Trenc, F., & Oprešnik, S. R. (2006). A new criterion to determine the start of combustion in diesel engines. *Journal of Engineering for Gas Turbines and Power, 128*(4), 928–933.
65. Wilhelmsson, C., Tunestål, P., Widd, B. J. A., & Johansson, R. (2009). *A physical two-zone NO x model intended for embedded implementation* (No. 2009-01-1509). SAE Technical Paper.
66. Shahbakhti, M., & Koch, C. R. (2009). Dynamic modeling of HCCI combustion timing in transient fueling operation. *SAE International Journal of Engines, 2*(1), 1098–1113.
67. Christensen, M. (2002). *HCCI combustion-engine operation and emission characteristics* (PhD thesis). Lund University, Lund.
68. Solaka, H. (2014). *Impact of fuel properties on partially premixed combustion* (PhD thesis). Lund University, Lund.
69. Solaka, H., Tunér, M., & Johansson, B. (2012, May). Investigation on the impact of fuel properties on partially premixed combustion characteristics in a light duty diesel engine. In *ASME 2012 Internal Combustion Engine Division Spring Technical Conference* (pp. 335–345).
70. Truedsson, I., Tuner, M., Johansson, B., & Cannella, W. (2013). Pressure sensitivity of HCCI auto-ignition temperature for oxygenated reference fuels. *Journal of Engineering for Gas Turbines and Power, 135*(7), 072801.
71. McAllister, S., Chen, J. Y., & Fernandez-Pello, A. C. (2011). *Fundamentals of combustion*. New York: Springer.
72. Rothamer, D. A., & Murphy, L. (2013). Systematic study of ignition delay for jet fuels and diesel fuel in a heavy-duty diesel engine. *Proceedings of the Combustion Institute, 34*(2), 3021–3029.
73. Moreno, C. J., Stenlaas, O., & Tunestal, P. (2017). *Influence of small pilot on main injection in a heavy-duty diesel engine* (No. 2017-01-0708). SAE Technical Paper.
74. Groendyk, M. A., & Rothamer, D. (2015). Effects of fuel physical properties on auto-ignition characteristics in a heavy duty compression ignition engine. *SAE International Journal of Fuels and Lubricants, 8*(1), 200–213.
75. Siebers, D. L. (1998). *Liquid-phase fuel penetration in diesel sprays* (No. 980809). SAE Technical Paper.
76. Jung, D., & Assanis, D. N. (2001). *Multi-zone DI diesel spray combustion model for cycle simulation studies of engine performance and emissions* (No. 2001-01-1246). SAE Technical Paper.
77. Finesso, R., & Spessa, E. (2014). Ignition delay prediction of multiple injections in diesel engines. *Fuel, 119*, 170–190.
78. Lee, M., Oh, S., & Sunwoo, M. (2011). Combustion phase detection algorithm for four-cylinder controlled autoignition engines using in-cylinder pressure information. *International Journal of Automotive Technology, 12*(5), 645.
79. Oh, S., Chung, J., & Sunwoo, M. (2015). An alternative method to MFB50 for combustion phase detection and control in common rail diesel engines. *IEEE/ASME Transaction on Mechatronics, 20*(4), 1553–1560.

80. Shehata, M. S. (2010). Cylinder pressure, performance parameters, heat release, specific heats ratio and duration of combustion for spark ignition engine. *Energy, 35*(12), 4710–4725.
81. Tazerout, M., Le Corre, O., & Ramesh, A. (2000). A new method to determine the start and end of combustion in an internal combustion engine using entropy changes. *International Journal of Thermodynamics, 3*(2), 49–55.
82. Thurnheer, T., & Soltic, P. (2012). The polytropic volume method to detect engine events based on the measured cylinder pressure. *Control Engineering Practice, 20*(3), 293–299.
83. Lawler, B. J. (2013). *A methodology for assessing thermal stratification in an HCCI engine and understanding the impact of engine design and operating conditions* (Doctoral dissertation). University of Michigan, Ann Arbor.
84. Lawler, B., Hoffman, M., Filipi, Z., Güralp, O., & Najt, P. (2012). Development of a postprocessing methodology for studying thermal stratification in an HCCI engine. *Journal of Engineering for Gas Turbines and Power, 134*(10), 102801.
85. Lawler, B., Lacey, J., Dronniou, N., Dernotte, J., Dec, J. E., Guralp, O., . . . & Filipi, Z. (2014). *Refinement and validation of the thermal stratification analysis: A post-processing methodology for determining temperature distributions in an experimental HCCI engine* (No. 2014-01-1276). SAE Technical Paper.
86. Livengood, J. C., & Wu, P. C. (1955). Correlation of autoignition phenomena in internal combustion engines and rapid compression machines. In *Symposium (international) on combustion* (Vol. 5, No. 1, pp. 347–356). Amsterdam: Elsevier.
87. Lawler, B., Lacey, J., Güralp, O., Najt, P., & Filipi, Z. (2018). HCCI combustion with an actively controlled glow plug: The effects on heat release, thermal stratification, efficiency, and emissions. *Applied Energy, 211*, 809–819.